NOVEL PULSED POWER APPLICATIONS

by

GEOFFREY ROBERT TURNER

Submitted in partial fulfilment of the academic
requirements for the degree of
Master in Science in the
Department of Physics
University of Natal
Durban

December 2001

ABSTRACT

The purpose of this dissertation is to examine the mechanisms of the glow (Townsend) discharge, the arc (streamer) discharge, the corona discharge, and the vacuum discharge. The physics of each discharge is presented and then investigated by way of mathematical model and experiment. Four novel pulsed power experiments constructed for the purpose of examining each discharge are presented. Namely a transverse electric atmospheric carbon-dioxide laser, a flash-lamp, a surface corona apparatus, and a plasma opening switch. Methods for the measurement of short duration intense electric and electromagnetic events are included. Practical aspects of pulsed power experimentation are discussed.

PREFACE

The work described in this dissertation was carried out at the University of Natal Laser Laboratory in Durban, and at the Atomic Energy Corporation of South Africa in Pretoria, from January 1995 to October 1999 under the supervision of Professor M. M. Michaelis.

These studies represent original work by the author and have not otherwise been submitted in any other form for any degree or diploma to any tertiary institution. Where use has been made of the work of others it has been duly acknowledged in the text.

CONTENTS

Chapter 5 : The Corona discharge

Chapter 6 : A Magnetically Interrupted Vacuum Discharge

Chapter 7 : Pulsed Current Measurements

ACKNOWLEDGMENTS

I would like to extend my thanks to Professor M. M. Michaelis for his support, guidance and patience throughout the long period of work which has culminated in this text. I would also like to extend my thanks to all at the University of Natal and Atomic Energy Corporation who contributed to the manufacture of components, without whom these experiments would not have been possible.

Chapter 1

Introduction

1.1 Scope and Purpose of this Dissertation

The purpose of this dissertation was to investigate at both at theoretical and practical level the physics of a transient electric discharge through a gaseous medium at various initial and boundary conditions. Specifically the:

- Glow discharge
- Arc discharge
- Corona discharge, and
- Vacuum discharge

under pulsed conditions were investigated. Emphasis was placed on the theoretical investigation of each discharge mechanism. The glow discharge, arc discharge and corona discharge were described predominantly as a function of gas pressure and electric field strength between two discharge electrodes. The vacuum discharge, however, focussed on the electrode geometry and a magnetic field caused to pass through the discharge space. The corona discharge was of the surface type, and was therefore also a strong function of the surface material. The specific theory of each discharge was derived from basic theory. The specific objectives of this dissertation were:

- To investigate and present the theory of each discharge mechanism as a function of all variables.
- To present the design and manufacture of each experiment.
- To present collected data.
- To compare collected data to theoretical predictions in order to verify or disprove the presented theory.

In most cases variables were too numerous to allow a simple theoretical analysis of each discharge mechanism. Numerical models were therefore frequently constructed to assist in an analysis and prediction of the discharge behaviour. Each discharge

was measured and categorised as a function of either the discharge voltage or discharge current. Without the aid of spectroscopic instrumentation it was not possible to categorise each discharge in greater detail. Voltage and current measurements were made easy with the abundance of voltage and current measurement equipment available. However, since this work dealt specifically with pulsed or *transient* discharges attention was paid to probe compatibility to ensure accurate measurement procedure. For this reason work was performed to develop a current probe suited to each experiment.

As is typical, a custom designed and manufactured apparatus was required for each experiment. Likewise specialised vacuum or pressure equipment, discharge electrodes, discharge vessels, pulsed power-supplies, diagnostic and measurement equipment was required. Since this work formed an integral part of the total project some aspects of the manufacturing have been included in this dissertation. However, since the construction of each experiment was not considered of primary importance to this work, careful attention was paid not to move the emphasis from the theoretical and physical mechanisms of each experiment to the practical considerations. Work was performed at the University of Natal, Durban (UND) laser laboratory, and at the Atomic Energy Corporation (AEC) of South Africa during the period from January 1995 to October 1999.

1.2 Motivation

The Motivation behind this work was primarily one of a desire to better understand and experience firsthand the physics of electric discharges. Much interest and excitement has been generated as a result of breakthroughs in semiconductor technology, to the extent that much of that which has been learned about gaseous discharges has been forgotten, and that which we never learned in the first place is no longer of concern since semiconductor technology now apparently governs all. While it is indeed true that semiconductor technology has revolutionised our planet, there still exists many applications governed by the physics of the gaseous discharge, particularly that of the low pressure discharge. Prior to the transistor revolution all radio frequency transmitters and receivers relied on vacuum tubes to function. To this day high power radio transmitters still require vacuum tubes. Other applications include radar and microwave installations, microwave ovens, lasers, and high power light sources. The simple sodium and mercury-arc lamps are two very common examples of light sources that rely on the motion of electrons through a gaseous volume to produce light.

Certain of the instruments described in this dissertation are of significance and may have a practical application. It is true that certain of the instruments and experiments described in this thesis were developed with a particular product in mind. It is difficult within any institution, academic or commercial, to obtain funding for a research project that does not show the potential to become a useful product. However, it is a sad fact that most of the hardware described in this dissertation is now locked away where it gathers dust daily. The lasers described in chapter 3 were intended to be used to burn markings onto goods for the purpose of identification. Some of these lasers were put into operation but failed generally as a result of their inability to perform in a harsh industrial environment. The flash-lamps described in chapter 4 were developed for the purpose of generating large quantities of ultraviolet light. These performed well until such time as the vacuum seals failed around the quartz envelope. The corona discharge experiment is still in use daily for the purpose of generating ozone. The plasma switch described in chapter 6 is an ongoing project. The ultimate intention is to use the device to generate microwave radiation in a similar fashion to that of a linear magnetron device.

1.3 Structure of this Dissertation

This dissertation is divided into seven chapters focussing on five main activities:

(i) The investigation of a volume stabilised transient glow discharge between two parallel uniform electric field electrodes at atmospheric pressure.
(ii) The investigation of a confined transient streamer discharge at low pressure and large electrode separation.
(iii) The investigation of an unconfined surface corona discharge caused to occur at atmospheric pressure over a dielectric material and at high rate of repetition.
(iv) The investigation of a discharge caused to occur between two concentric cylindrical electrodes in vacuum due the injection of a plasma, and the interaction between the discharge and a the magnetic field due to the centre current carrying electrode.
(v) The theory, design and manufacture of a the fast rise-time current measurement probes used on each of the above experiments.

In chapter two the basic theory of the gaseous discharge is presented. The three main discharge mechanisms

(i) The Townsend discharge,
(ii) The Streamer discharge, and the
(iii) Vacuum discharge

are identified and their theory discussed.

In chapter three an investigation of a volume stabilised glow discharge is presented. An analysis of the glow discharge is specifically applied to the case of two TEA CO_2 lasers and results presented.

In chapter four an investigation into the streamer discharge at high electric field strength and low pressure is presented. A theoretical analysis and mathematical model of the streamer discharge is specifically applied to the case of a linear low pressure xenon flash-lamp. Modelled and measured results are presented and compared. The details of the high-current pulsed power-supply are given.

In chapter five an investigation of a surface corona discharge at atmospheric pressure is presented. A theoretical analysis and mathematical model of the corona discharge is specifically applied to the case of the corona discharge caused to occur over the surface of an aluminium-oxide dielectric slab. Modelled and measured results are presented and compared. The details of a low-current high rate of repetition pulsed power supply are given.

In chapter six an investigation of a vacuum discharge between two concentric cylindrical electrodes due an injected carbon plasma is presented. The influence of the magnetic field due to the current carrying centre conductor is calculated and a theoretical model of the combined vacuum discharge and magnetic field / vacuum discharge interaction is applied to the case of the plasma opening switch. Modelled and measured results are presented and compared. The details of the plasma opening switch and high-current pulsed power supply are presented.

In chapter seven the current measurement techniques applied in the above experiments are discussed. The theory of current measurement by means of magnetic field sampling is discussed and the design, manufacture and mathematical modelling of the popular Rogowski coil current probe presented. Rogowski coil results are presented and compared to theoretical expectations.

Chapter 2

Transient Discharges Through Gaseous Media

2.1 Introduction

When a volume of gas is stressed under the influence of an applied electric field, a flow of electrons through the gas, that is to say an *electric discharge*, may result. Any gas at standard temperature and pressure (STP) is expected to be a non-conductor of electricity. That is to say a gas is typically an *insulator*. However, certain conditions may lead to an increase in the conductivity of a gas, such as an increase in temperature, or a rearrangement of molecular / electronic structure as a result of an applied electric field. The theory of gaseous discharges describes many phenomenon known to all. Probably the most common is lightning, an example of which is shown in figure 2.1. A common man made example is that of the fluorescent lamp, a stable low pressure gaseous discharge tube which provides us with light to see by. In comparison, however, lightning would be considered to be a transient event due to its short duration and unstable behaviour.

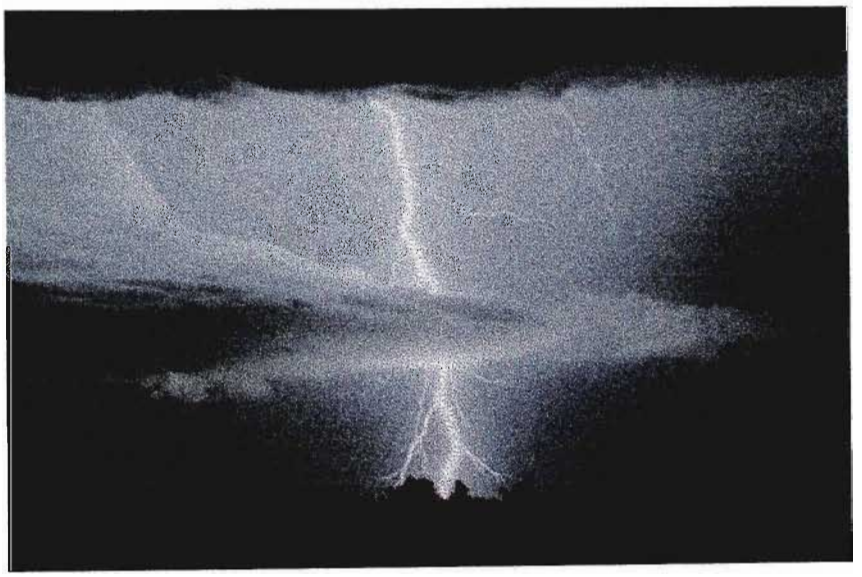

Figure 2.4 : Lightning – an arc discharge familiar to everyone.

2.2 Basic Discharge Theory

2.2.1 The Townsend Discharge

Two well known breakdown mechanisms exist whereby an initially non-conducting column of gas between two electrodes inside a sealed tube may be forced to conduct electricity. One is *Townsend* breakdown and the other is *Streamer* breakdown. Even today the fundamental physical processes that govern gas breakdown are not well understood [**1**]. However, the effects of macroscopic parameters such as electrode shape, electrode separation, gas pressure, gas type, applied voltage and voltage rise-time have been documented to the extent that the development of a discharge from an initial electron to the point of gas *breakdown* (that point at which the discharge becomes self sustained) is believed to proceed primarily as a function of the applied electric field. According to Kunhardt [**2**], if the voltage applied to a discharge tube exceeds the self breakdown voltage by less than a few percent, then breakdown occurs via avalanche processes requiring secondary mechanisms to maintain the discharge. This is referred to as a Townsend discharge. If the applied voltage exceeds the self breakdown voltage by more than a few percent, then streamer breakdown will dominate.

If the cathode of the discharge tube is irradiated with photons from an *external* source, any photon of energy greater than the work function of the cathode material will eject an electron from the cathode surface [**3**]. Electrons ejected from the surface of the cathode are carried down the tube under the influence of the applied electric field. As these electrons drift down the tube collisions with other gas molecules may occur. If N_0 electrons per second are generated at the cathode surface ($x=0$) due to the external source, then the number of electrons reaching the anode ($x=d$) is given by [**4**]:

$$N_e(d) = N_e(0)e^{\alpha d} \qquad \textbf{(2.1)}$$

where α is Townsend's first ionisation coefficient and d the electrode separation. Townsend's first ionisation coefficient is the number of ionising (that is to say electron yielding) collisions per unit distance, and is a function of both the electric field strength E (which is not necessarily uniform) and the gas pressure p.

If the external photon source is removed from over the cathode of the discharge tube the discharge will cease since no mechanism exists to sustain the emission of electrons from the cathode surface. However, if sufficient photons are generated from within the discharge column, due to collisions, sufficient photons may be returned to the cathode to sustain the emission of electrons from the cathode *without the requirement* for the external photon source. The return of photons to the cathode due to the discharge is a secondary process. Secondary processes can occur either at the cathode or in the volume of the gas. Secondary processes, according to Kunhardt, include:

- Photons striking the cathode, δ processes.
- Positive ions striking the cathode, γ processes.
- Gas ionisation by photo-ionisation.
- Gas ionisation by collision with positive ions, β processes.

Townsend assumed in his work that the sole secondary process was that due to ions travelling in the reverse direction along the tube to the cathode. γ is Townsend's second ionisation coefficient. He related the outgoing electron current to the incoming ion current according to:

$$N_e(0) = \gamma N_p(0) + N(0) \qquad \textbf{(2.2)}$$

Since a new ion is created each time an electron is created, Townsend related the ion current at the cathode ($x=0$) to the ion current at the anode according to:

$$N_p(0) = N_p(d) - N_e(d) + N_e(0) \qquad \textbf{(2.3)}$$

Combining equations 2.1, 2.2, and 2.3:

$$N_p(d) = \frac{N_O}{\gamma} - \frac{N_e(0)}{\gamma}\left(1 - \gamma\left(e^{\alpha d} - 1\right)\right) \qquad \textbf{(2.4)}$$

However, since at low current the anode will not emit ions, $N_p(d) = 0$. Hence:

$$N_e(0) = \frac{N_O}{\left(1 - \gamma\left(e^{\alpha d} - 1\right)\right)} \tag{2.5}$$

which, by equation 2.1, is written as:

$$N_e(d) = \frac{N_O e^{\alpha d}}{\left(1 - \gamma\left(e^{\alpha d} - 1\right)\right)} \tag{2.6}$$

This is the very famous Townsend equation describing the electron current at the anode in a Townsend discharge. If the external photo-ionisation source is removed from over the cathode N_O will be reduced to zero and discharge will cease unless the denominator in equation 2.6 equates to zero. This is the well known requirement for a self-sustained Townsend discharge. Hence:

$$\gamma\left(e^{\alpha d} - 1\right) = 1 \tag{2.7}$$

Solving equation 2.7 for the discharge length:

$$d = \frac{\ln\left(1 + \frac{1}{\gamma}\right)}{\alpha} \tag{2.8}$$

Note, Townsend's first ionisation coefficient α is a function of the electric field $E(x)$ between the electrodes, due to the applied voltage V, and a property of the gas. Townsend's second ionisation coefficient is a property of the cathode material and the gas. At that point beyond which the production of electrons at the cathode no longer requires an external source of photons the discharge is termed *self sustained*, and the gas is said to be *broken down*. Since one electron may incur many collisions while *en route* to the anode, one electron may be responsible for the generation of many more. The process whereby a single *primary* electron generates many *secondary* electrons is termed an *avalanche*.

Since the electric field strength is a function of distance x along the discharge tube, Townsend's first ionisation coefficient is likewise a function of x. It is common therefore to replace α with $\overline{\alpha}$ where:

$$\overline{\alpha} = \frac{1}{d_c}\int_0^{d_c} \alpha(x)dx \qquad \textbf{(2.9)}$$

where d_c is defined as the length of the cathode fall region, or that distance from the tip of the cathode to that point in the discharge where the electric field is zero. Hence, the cathode fall region is that region of the discharge, beginning at the surface of the cathode, over which the majority of the applied potential is dropped. The self-sustained discharge condition therefore becomes:

$$d_c = \frac{\ln\left(1+\frac{1}{\gamma}\right)}{\overline{\alpha}} \qquad \textbf{(2.10)}$$

Ward [**5**] described Townsend's first ionisation coefficient in terms of the electric field strength E and gas pressure p according to:

$$\alpha = Ape^{-B\left(\frac{p}{E}\right)^{\frac{1}{2}}} \qquad \textbf{(2.11)}$$

where A and B are empirically determined constants for a particular gas. For example, in the case of argon gas, A=29.2/cm.torr and B=26.62V/cm$^{1/2}$.torr$^{1/2}$. In order to relate the properties of the gas and electric field to an electron current an additional equation is required. According to Ingold [**6**], under the assumption that the movement of the ions through the tube are mobility limited, and independent of the electric field, the ion current density is written:

$$J_p(0) = \frac{\left(9\varepsilon\mu_p/8e\right)}{d_c^{\,3}}V^2 \qquad \textbf{(2.12)}$$

where V is the voltage across the cathode fall region, ε is the permittivity of free space, e is the charge of an electron, and μ_p is the ion mobility.

According to equation 2.2 the electron current density J_e at the cathode is therefore:

$$J_e(0) = \gamma \frac{(9\varepsilon\mu_p / 8e)}{d_c^{\,3}} V^2 \qquad \textbf{(2.13)}$$

For every electron that leaves the cathode an electron must be supplied by an external current source. Equation 2.13 describes the electron current supplied to the discharge tube, and may be measured with a series connected ammeter. Equation 2.10, the self-sustained discharge condition, is substituted into equation 2.13. Hence:

$$J_e(0) = \frac{\gamma \bar{\alpha}^3 (9\varepsilon\mu_p / 8e)}{\left(\ln\left(1+\frac{1}{\gamma}\right)\right)^3} V^2 \qquad \textbf{(2.14)}$$

Equation 2.14 relates the density of the supplied electron current to the voltage across the cathode fall region within a self-sustained discharge. It is often assumed that the electric field over the cathode fall region is approximately linear, expressed as:

$$E = E_O\left(1 - \frac{x}{d_c}\right) \qquad \textbf{(2.15)}$$

where:

$$E_o = 2\frac{V_O}{d_c} \qquad \textbf{(2.16)}$$

Hence, equation 2.11 may be evaluated using equation 2.16 in order to determine Townsend's first ionisation constant. With α determined as a function of x, equation 2.9 may be evaluated to determine $\bar{\alpha}$, and substituted into equation 2.14 to determine the VI characteristic of a self-sustained Townsend discharge. While the above analysis is useful, it applies only to a stable low pressure Townsend discharge, and requires that the attachment coefficient, μ, be disregarded. Furthermore, If the applied electrode potential is substantially higher than the self break voltage then the induced space charge (due to the separation of ions and electrons) can be sufficient to cause the onset of a *streamer* discharge, transforming an otherwise orderly avalanche into a rapidly propagating plasma arc.

2.2.2 The Streamer Discharge

A streamer discharge occurs when electrons and ions created during electron-specie collisions separate under the influence of the applied electric field due to the greater mobility of electrons compared to the lesser mobility of ions. If the applied electrode potential is large compared to that required to sustain the discharge, then the electron-ion separation will be large, creating localised regions of high field strength, termed and *avalanche*. Each *avalanche* may be seen as a small cone shaped accumulation of locally separated charge, with a localised anode and a localised cathode, experiencing localised secondary electron and photon emission, which in turn causes secondary avalanches to form in front of and behind the head of the primary avalanche. These anode and cathode directed secondary avalanches develop and propagate at a rate faster than the primary avalanche (due to the increase in the space-charge enhanced electric field) along the axis of the primary avalanche (where the localised space-charge field supplements the already large applied field). As the negatively charged primary avalanche head propagates towards the anode it leaves behind it a positively charged tail which continues to grow until the anode is effectively connected to the cathode via the highly conductive, highly ionised plasma streamer or *arc*. Figure 2.2 details the formation of a streamer.

In the case of streamer formation it would not be expected that the streamer *self stabilise* or 'spread out' (inhibiting the growth of the arc) since the *longer* the streamer the *stronger* the localised space-charge field and the *stronger* the localised field the *greater* the tendency of the streamer to follow the lines of electric field, until the space-charge field eventually compares to the applied field. This explains the filamentary appearance of the streamer discharge. It therefore seems intuitively correct to assume that the likelihood of streamer formation would be greater if the applied field were increased by raising the electrode potential or decreasing the electrode separation, which is known from experience to be true. Streamer formation can be forced to occur at *any* pressure due to its dependence on the *magnitude of the applied electric field*, but becomes harder to force to occur at lower pressures due to the decreased localised space-charge fields and decreased secondary electron and photon emission due to the decreased gas density.

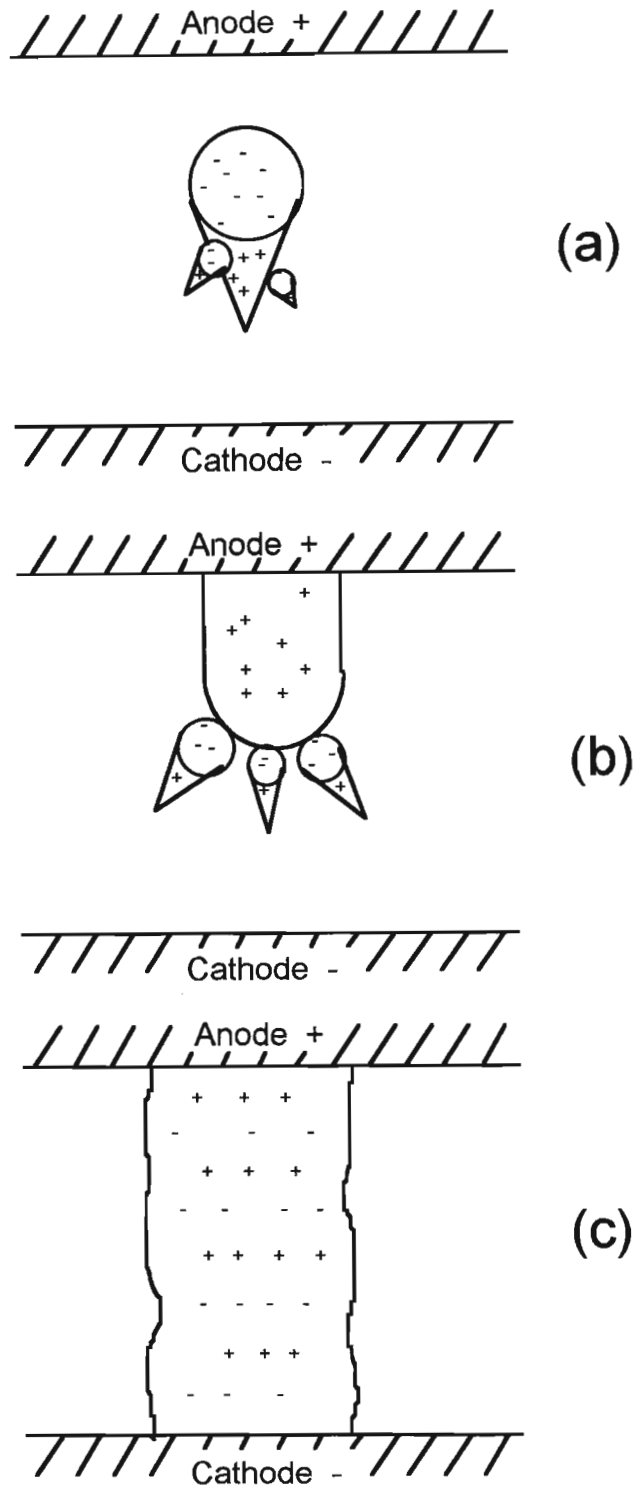

Figure 2.2 : Diagrams showing (a) streamer development around a single primary avalanche, (b) the cathode directed plasma streamer after the primary avalanche has reached the anode and, (c) the complete bridging of the gap by the plasma streamer.

2.2.3 The Vacuum Discharge

The vacuum discharge is, despite its name, a gaseous discharge, since no matter how low the absolute pressure that may be *practically* obtained within a vacuum chamber, some molecules or atoms of the gas which previously filled the chamber must remain present. The theory of a vacuum discharge is however markedly different to that which governs low pressure and high pressure gaseous discharges. However, since the vacuum discharge was investigated for the purposes of this dissertation, a brief introduction to the vacuum discharge is now presented.

A vacuum discharge may be observed to occur between two electrodes in an evacuated discharge tube under the influence of a sufficiently high electric field. In the absence of a gaseous medium electrons emitted from the cathode surface will be carried across the cathode-anode gap with few ionising collisions *en route*. Hence, at low current density, no ions will be returned to the cathode to sustain the discharge. The discharge must instead be sustained by an external source of photo-ionisation incident upon the cathode surface. If the ionisation source is removed, the photoelectric effect at the cathode will cease, and the discharge will self-terminate. However, at high current densities ions will be released both at the cathode and anode surface, causing the discharge to self sustain for as long as the high current discharge is supported by the discharge power supply.

If no external mechanism is available to break down the vacuum gap, then the applied electric field must be raised sufficient to cause the onset of *field-emission*. Field-emission occurs in vacuum when electrons are caused to break-away from the cathode surface and enter the gap under the influence of an extremely high electric field. In this way a high current vacuum discharge may commence. However, at a substantially lower potential a discharge may be caused as a result of an injected source of electrons and ions. For example, an arc discharge may be caused between two small closely positioned electrodes adjacent to the cathode, or a plasma of ions and electrons may be injected into the vacuum gap from an external plasma source. Electrode erosion is almost always a problem in vacuum gaps since ions from one or both electrodes may be caused to enter the gap at high electron current in order to sustain the discharge. A stainless steel cathode may, for example, be used to chrome plate the inside of a discharge tube due to chrome ions released from the cathode surface.

2.3 Conclusions

A basic introduction to the Townsend, streamer and vacuum discharge has been presented. In the case of the Townsend discharge the attachment coefficient, μ, has been ignored. The above theory is therefore applicable only to non-attaching gasses. Impurities in such a gas could lead to a modification of the Townsend coefficients as a result of electron-specie attachments. In both the case of the high pressure and vacuum discharge thermionic emission has been ignored. In any sustained discharge localised heating will occur, causing electrons to eject from the cathode surface as a result of increased kinetic energy. Thermionic emission is of little interest in the case of a vacuum discharge required to break down promptly due to the time scale over which the cathode would be required to be heated. In chapters three through six of this text a detailed investigation into the four types of discharge is presented. Namely:

- The volume stabilised glow discharge
- The arc discharge
- The surface corona discharge
- The magnetically Interrupted vacuum discharge.

The theory of these four topics form specific sub-sections of the above discussion. Detailed theory and a practical investigation into each is presented.

Chapter 3

A Volume Stabilised Glow Discharge

3.1 Introduction

In accordance with the work presented in chapter two a glow discharge is not expected to form at near atmospheric pressures. Due to the strong electric field required to achieve breakdown and large number of specie per unit volume the tendency will be towards streamer formation. A filamentary streamer is by nature (and appearance) a highly conductive narrow path formed through an otherwise essentially non-conducting medium. While the filament of a streamer is highly conductive, the surrounding volume is essentially non-conductive. That is to say, a filamentary discharge is *inhomogeneous*. Streamer breakdown is caused by the onset of strong localised space-charge fields associated with individual primary electron avalanches randomly initiated within the discharge gap. This is unlike the classical glow discharge which relies on the generation of secondary electrons at the cathode.

It *is* possible, however, to prevent the formation of an arc at near atmospheric pressure by promoting the growth of *many* primary avalanches, as opposed to one *single* avalanche, which would grow into a streamer. By promoting the growth of many avalanches throughout the discharge volume the current density associated with each individual avalanche may be kept below that limit beyond which a streamer might form. Such a discharge is termed *volume stabilised*, since it is the occurrence of the discharge through a *larger volume than would normally occur naturally* that promotes the stable discharge.

Levatter and Lin state [7] that homogeneous avalanche growth will be promoted in the discharge volume if the gaseous medium is *ionised* prior to the application of the electric discharge. The source of ionisation may be electron-beam, x-ray, or more commonly, photo-ionisation. According to Levatter and Lin, when an electric potential is applied to a pair of uniform-field electrodes in the presence of a sufficiently strong ionisation source, multiple primary avalanches form as a function of the density and uniformity of the ionised high pressure gaseous medium. In a pre-formed plasma of ions and electrons it would be anticipated that *all* (as opposed to isolated members)

of the available electron-ion cloud would begin to separate under the influence of the applied electric field, forming *many* localised space-charge fields, or *primary avalanches*. Indeed, streamer formation will continue in the manner described in chapter two unless the density of the multiple primary avalanches (caused to form as a result of the preionisation) is sufficiently high that the boundaries of the primary avalanches overlap. Under this condition any secondary ionisation will also overlap. Hence the *overall* space-charge field will effectively be *smoothed*, preventing the formation of *individual* streamers associated with the singular regions of high field strength that form when the secondary avalanches are closely associated with only *one* primary avalanche. The effect of secondary avalanche development is then one of *homogenising* the conducting medium since there is no *single* primary avalanche that secondary ionisation can influence, but rather *many*. The type of discharge is therefore a *volume stabilised multiple avalanche discharge,* rather than a volume stabilised *glow discharge*. Due to the similarity in appearance to a glow discharge, the name has remained unchanged.

In order to ensure the formation of a volume stabilised glow discharge at high pressure:

- The discharge volume must be ionised *prior* to the application of the electric discharge.
- the electric field between the discharge electrodes must be kept everywhere uniform in order to promote homogenous avalanche formation. If not, streamer formation, will be promoted in those regions of higher electric field strength.

Since the ionisation of the medium must precede the electric discharge the ionisation mechanism is often referred to as *preionisation*.

3.2 The TEA CO_2 Laser

The volume stabilised glow discharge is of specific interest due to its application in the transverse electric atmospheric (TEA) carbon-dioxide (CO_2) laser. Levatter and Lin state that the self-sustained volume discharge initiated by a homogeneous electron avalanche is a convenient method of gas laser excitation. The TEA CO_2 laser requires that energy be delivered to the numerous vibrational and rotational molecular CO_2 energy levels by means of a homogenous electrical discharge. Energy is withdrawn from the laser as a photon emission in accordance with the theory of stimulated emission. However, to extract a meaningful energy output the pulsed CO_2 laser must be operated at high pressure. Near atmospheric pressure is common. Hence, a stable glow discharge is, under normal conditions, not to be expected. If the discharge between the electrodes of a TEA CO_2 laser is allowed to favour the formation of an arc, then the efficient excitation of the medium is not possible.

An arc discharge, although not desired between the laser electrodes, is a rich source of hard UV [**8**], and is the preferred source of preionisation for the TEA CO_2 laser. UV is produced by means of multiple arc discharges formed between an array of spark-pins mounted in pairs parallel to the electrode gap. The arc that forms across each pair of opposing pins is responsible for the production of a fraction of the total UV required to preionise the gas volume between the electrodes. Each pair of spark pins is connected in parallel with the laser electrodes, but isolated from the electrodes by either one or two small value *'spark-pin'* capacitors. This is referred to as the *double discharge spark-pin technique*. The energy of the spark-pin generated UV is given up to remove electrons (temporarily at least) from their orbits in order to serve as conduction electrons. The shorter the wavelength of an incident photon the higher the probability of removing an electron from its orbit, since (according to Planck's relation $E=h/\lambda$) the shorter the wavelength the higher the energy. That is, the energy that *must* exceed the ionisation energy required to remove the electron from its particular orbit up into the conduction band. In this manner the surrounding volume of gas is raised from the *gaseous* state to the *plasma* state in order that the gas become, if only *momentarily* and *partially*, a *homogenous conductor of electricity*.

While providing an efficient source of preionisation, spark pins pose a specific problem. As a result of the high current density of each individual preionisation streamer, the dissociative reactions (common in any electron bombardment or arc

discharge situation) are abundant. Hence, the decomposition of CO_2 into CO and O^- ions at the spark pins within a TEA CO_2 laser can cause arcing between the primary laser electrodes if the decomposition products are free to circulate around the laser head *before* recombining. Pace *et al* [**9**] have examined the problem of dissociation in TEA CO_2 lasers and comment that the addition of as little as 2% oxygen to the gas mix can increase the negative ion concentration by an order of magnitude, causing severe arcing due to the increased formation of concentrated streamers. If the CO_2 dissociation can be prevented the occurrence of arcing can be reduced. Pace *et al* have examined the addition of up to 4% CO and 4% H_2 to the gas mix in order to address this problem. The addition of CO to the gas mix is known to prevent the production of oxygen ions by shifting the equilibrium of the CO_2-electron impact reaction

$$e + CO_2 \rightarrow e + O + CO \ , \qquad \textbf{(3.1)}$$

to the left. The dissociation of CO_2 is therefore forcibly discouraged. The addition of H_2 to the mix has been shown by Pace *et al* to act as a catalyst in the recombination of O_2 with CO by first reacting with O_2 or O^- ions to form hydroxide OH^- ions according to the reactions:

$$H + O_2 \rightarrow OH + O \, , \qquad \textbf{(3.2)}$$

and

$$H_2 + O \rightarrow OH + H \, . \qquad \textbf{(3.3)}$$

The OH^- ion is free to react with available CO according to:

$$OH + CO \rightarrow CO_2 + H \qquad \textbf{(3.4)}$$

The addition of H_2 to the gas mix therefore encourages the recombination of O^- and CO into CO_2. The released H^- ion further fuels reaction 3.2 or recombines with other H^- ions to form H_2. The H^- ion can also recombine with the OH^- ions to form H_2O, which further promotes arcing. Pace *et al* state that it is therefore important to keep the H_2 content below 4% in order to maintain the H_2O content at an acceptable level.

3.3 Results

The results of the work performed on two TEA CO_2 lasers is presented. Work was performed at the University of Natal, Durban, (UND) laser laboratory, and at the Atomic Energy Corporation of South Africa (AEC), Optical Energy Systems (OES) laboratory. The discharge circuit implemented on both lasers is shown in figure 3.1. Differences between the two lasers included the electrode length, electrode width, electrode separation, number of spark pin pairs, and number of spark-pin capacitors. Both lasers contained a row of spark-pins down either side of the discharge electrodes as a preionisation source. The AEC laser comprised a 100nF, 50kV double ended Maxwell™ capacitor C charged to 30kV, discharged into the laser head via a CX-1685 deuterium thyratron switch S. The UND researched device comprised a ~100nF hand-made cylindrical rolled foil capacitor C charged to 17kV, discharged into the laser head via a nitrogen spark-gap switch S. Inductor L_s was required for the purpose of providing a DC path to ground during the charging of capacitor C. During the laser discharge, inductor L_s carried negligible current in comparison to the discharge current due to its sufficiently high impedance, and was therefore excluded from any analysis of the head. The value of L_s was determined to be 25mH.

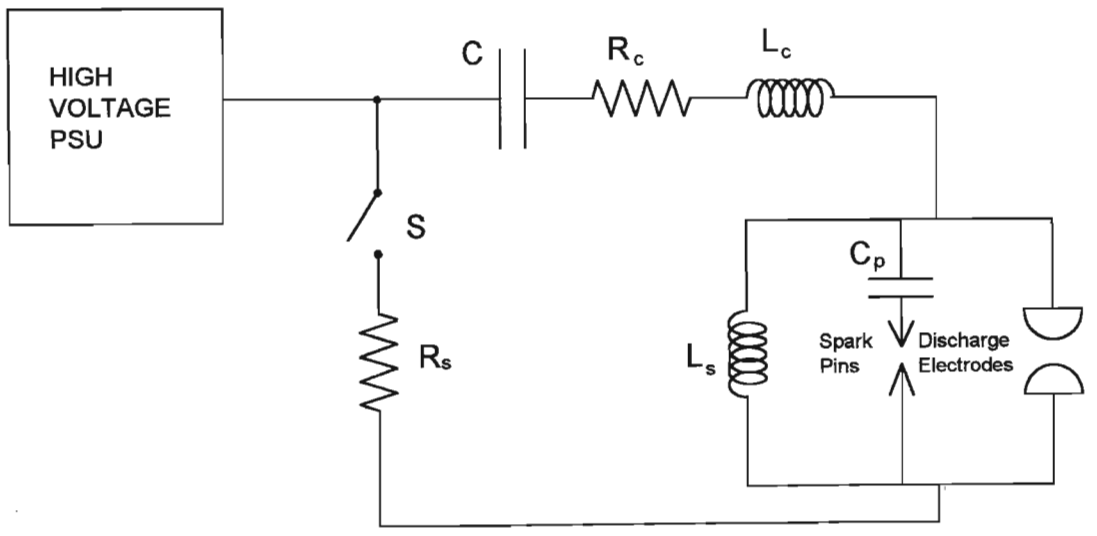

Figure 3.1 : A typical TEA CO_2 laser discharge circuit attached to the spark-pin assembly and laser electrodes.

In both TEA CO_2 laser variants each pair of spark-pins was connected to two spark-pin capacitors as opposed to one. The use of two spark-pin capacitors was advantageous since the voltage requirement of each spark-pin capacitor was halved. The capacitance of each capacitor did however have to be doubled. In addition the spark-pin capacitors provided mechanical support for the spark-pins. Figure 3.1 shows the spark-pin capacitors lumped into one equivalent capacitance, denoted Cp. Other lumped circuit parameters included the on resistance of switch S, denoted R_s, the equivalent series resistance of the capacitor C, denoted R_c, and the equivalent series inductance of capacitor C and the discharge circuit, denoted L_c.

The TEA CO_2 laser researched at UND is shown in figure 3.2. The laser head comprised an assembly of forty 1nF, 15kV disc ceramic capacitors arranged in pairs along both sides of the laser electrodes. The electrode separation was 16mm. The electrodes were of the Ernst profile. The spark pins were manufactured from M3 grub screws inserted into two hollowed out 15 mm × 20 mm × 450 mm Perspex slabs and locked in place with M3 nuts. The ceramic capacitors chosen for this device were of the flexible lead type and were simply soldered between a copper plate attached to the upper surface of either electrode and to solder tabs placed over each of the spark pins. The Perspex slab was inserted into the two Perspex blocks which support the electrodes and locked in place with M6 nylon screws. Spark-pin separation was set to 1.5mm.

The TEA CO_2 laser researched at the AEC is shown in figure 3.3. The laser (one of many developed at the AEC) comprised the upper and lower discharge electrodes attached to 35 vertically opposed spark pin pairs isolated from the discharge electrodes by a total of seventy 35kV, 600pF ceramic capacitors, eighteen and seventeen pairs per side respectively. The electrodes were of the Rogowski profile. The electrode separation was 30mm. The spark pins were manufactured from 15mm stainless steel M4 grub screws located in the end of each capacitor and locked in place with an M4 nut. The loosening of the nut and the screwing in or out of the grub screw facilitated the adjustment of the gap, which in this case was set to 2.0mm all round.

Figure 3.4 shows the complete TEA CO_2 laser experiment installed in the UND laser laboratory. Figure 3.5 shows the complete AEC manufactured TEA CO_2 laser.

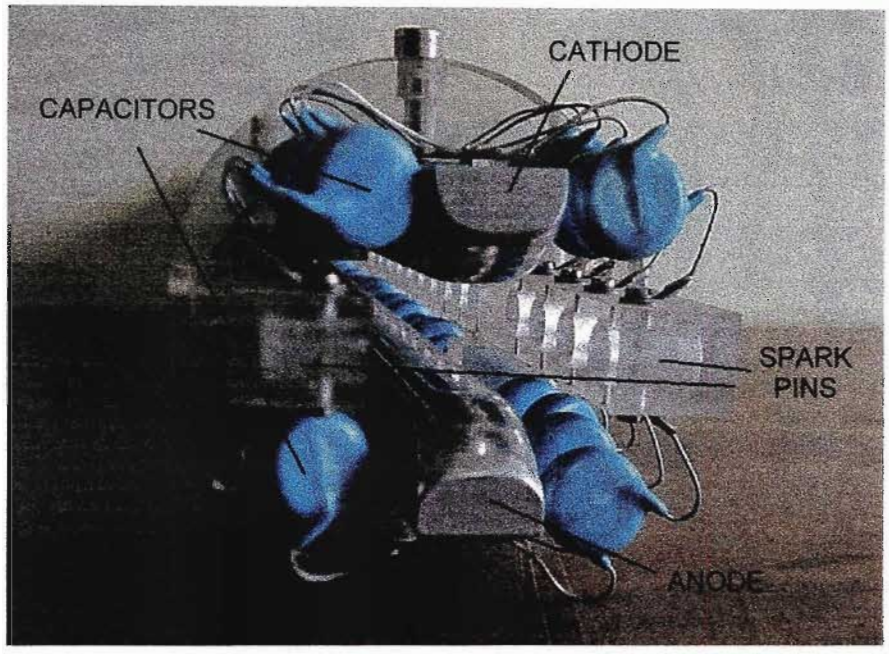

Figure 3.2 : Laser head from the pulsed TEA CO_2 laser researched at UND.

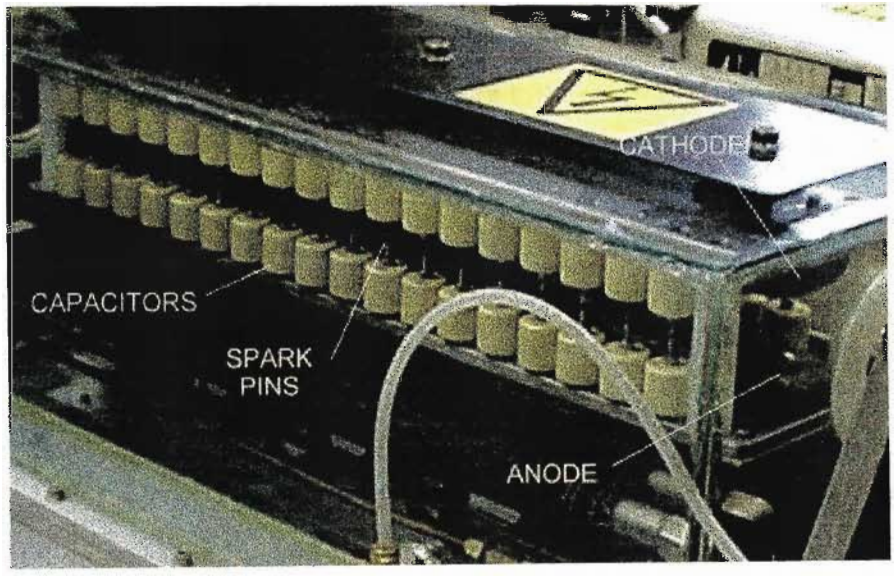

Figure 3.3 : Laser head from the pulsed TEA CO_2 laser researched at the AEC.

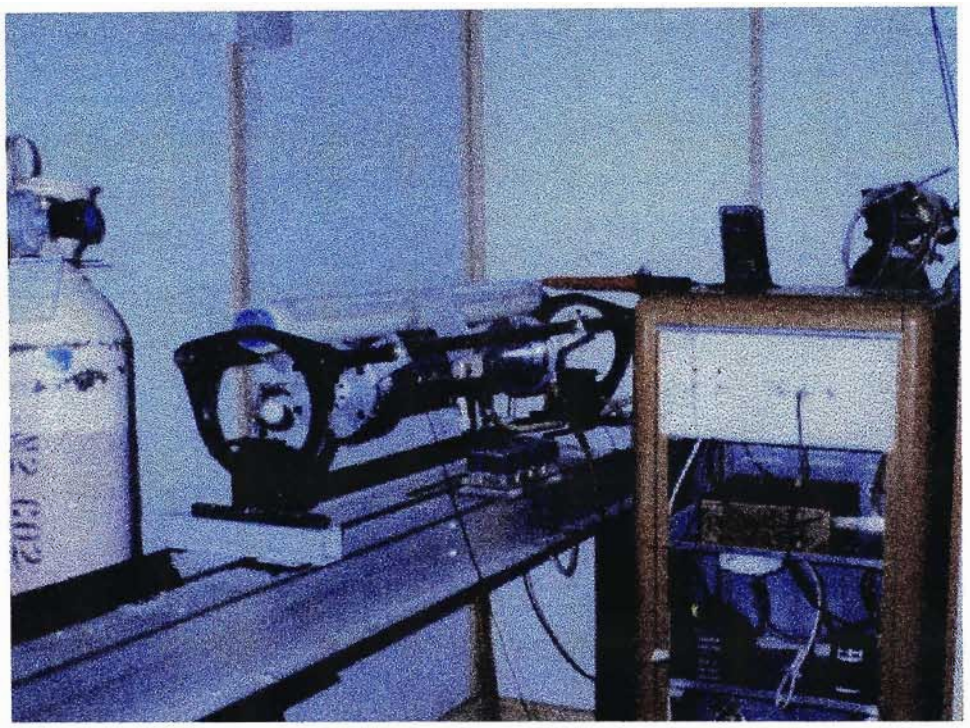

Figure 3.4 : The TEA CO_2 laser experiment at the UND laser laboratory.

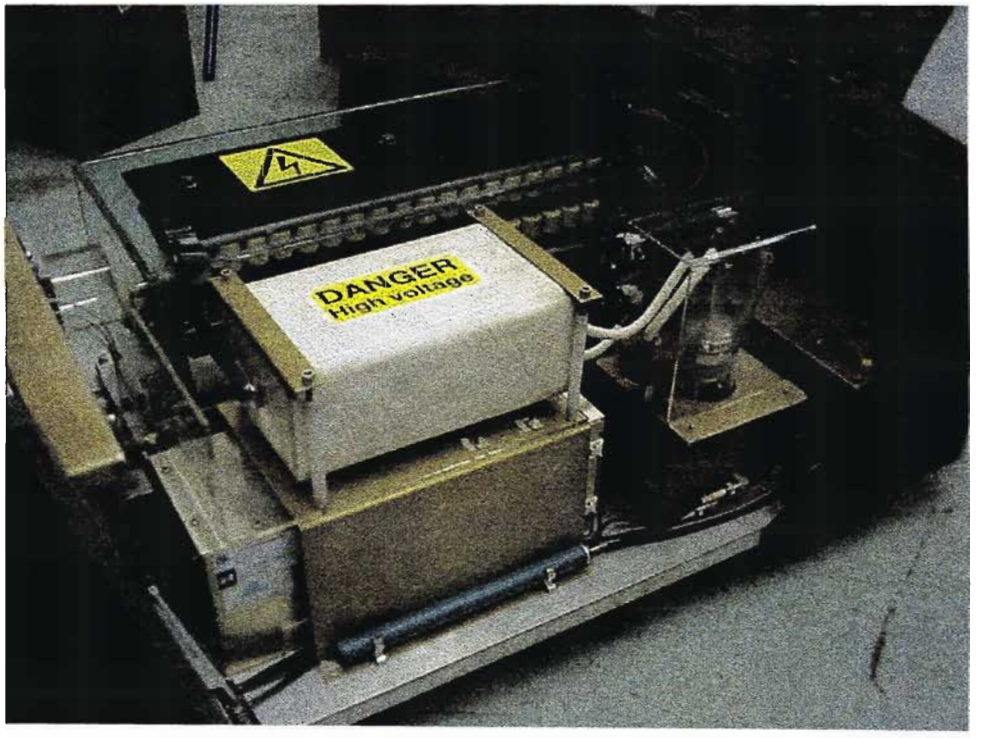

Figure 3.5 : The TEA CO_2 laser developed at the AEC.

In each case the discharge capacitor C was determined according to the required energy loading of the gas-mix at the chosen operating voltage V, where V was determined according to the required electric field strength at the electrodes as a function of the electrode separation and gas mix. In both cases a carbon-dioxide, nitrogen, helium (CO_2:N_2:He) ratio of 1:1:8 was used. In the UND case the gas mix was not of research grade. In accordance with the work of Denes and Lowke [**10**] a self sustained discharge voltage V_s of ~6.3kV/cm.atm was determined for the 1:1:8 gas mix. Hence a self sustained discharge voltage of ~15kV was determined for the UND laser operated at 1.5atm pressure, and ~19kV for the AEC laser operated at 1atm pressure. In order to ensure the successful operation of both devices it was necessary that the charging voltage of the respective storage capacitors *exceed* the determined self-sustained discharge voltage, but not exceed that limit at which the discharge showed a tendency to arc due to the overloading of the gaseous medium.

The active volume of the UND researched TEA CO_2 laser was determined to be 100cm^3. The chosen energy loading value at 1.5atm pressure was 0.15J/cm^3. Hence the required energy content of the storage capacitor was 100cm^3 × 0.15J/cm^3 = 15J. Given that energy stored in a capacitor is $\frac{1}{2}CV^2$, then at a chosen operating voltage of 17kV the required storage capacitance C was determined to be ~100nF. Given that the maximum allowable energy loading of the 1:1:8 gas mix at 1.5atm pressure is 0.25J/cm^3, storage capacitor C could theoretically be charged to ~22kV before the onset of electrode arcing. The discharge circuit shown in figure 3.1 is a typical capacitor-inductor-capacitor (CLC) type energy transfer circuit. Hence, provided the capacitance of the spark-pin assembly C_p was at least *ten times less* than that of the discharge capacitor C, voltage doubling was expected to occur across laser electrodes prior to the breakdown of the gas. Hence, a *maximum* peak voltage across the UND laser head of 34kV was predicted. This was assumed to be sufficient to ensure the breakdown of the gas between the electrodes in the presence of the UV preionisation. The total spark-pin capacitance C_p was approximated to one tenth C. Hence C_p = 10nF. Making use of the available 1nF units (2 in series = 500pF) it was determined that twenty 500pF capacitor pairs would be required.

In the same fashion as above the active volume of the AEC TEA CO_2 laser was determined to be 450cm^3. The chosen energy loading at 1atm pressure was 0.10J/cm^3. Hence the required energy content of the storage capacitor was 450cm^3 × 0.10J/cm^3 = 45J. At a chosen operating voltage of 30kV the required storage

capacitance C was also determined to be ~100nF. Given that the maximum allowable energy loading of the 1:1:8 gas mix at 1 atmosphere pressure is 0.17J/cm^3 storage capacitor C could theoretically be charged to ~39kV before the onset of electrode arcing. Again, provided the capacitance of the spark-pin assembly C_p was at least ten times less than that of the discharge capacitor C, then voltage doubling was expected to occur across laser electrodes prior to the breakdown of the gas. Hence, a *maximum* peak voltage across the AEC laser head of 60kV was predicted. This was assumed to be *more than* sufficient to ensure the breakdown of the gas between the electrodes in the presence of the UV preionisation. The total spark-pin capacitance C_p was approximated to one tenth C. Hence C_p=10nF. Making use of the available 600pF units (2 in series = 300pF) it was determined that 33 of the 600pF capacitor pairs would be required. Thirty-five pairs were installed.

According to the work of Denes and Lowke [**10**] the higher the applied peak voltage the faster the breakdown of the gas. Hence, the higher the peak voltage prior to breakdown the better. However, Since the self-sustained electrode potential V_s (after breakdown) is a function of the gas mix, gas pressure, and electrode separation, the difference in potential between the capacitor charging voltage V and the discharge potential V_s *must be dropped across some other circuit element.* In most cases this is across the stray circuit inductance L_s, the equivalent series resistance of the discharge capacitor R_c, and the *on* resistance of the switch R_s. In the case of the AEC built laser a deuterium thyratron switch was used. Hence the above was not seen to represent an optimum solution since thyratrons damage easily. However, a charging voltage of 30kV and self-sustained discharge potential of 19kV was considered to offer a suitable compromise between circuit speed and component lifetime. Since the UND device was intended purely for short duration experimental purposes component lifetime was not considered an issue. No extensive mathematical modelling of the circuit was performed.

In spite of the extensive effort placed into the UND researched TEA CO_2 laser, not one single homogeneous non-filamentary multiple streamer discharge was observed to take place. In accordance with the theory presented above, this discharge should have resembled a *glow* discharge. Instead only filamentary streamer (arc) discharges were observed. At the time it was speculated that this was as a result of insufficient preionisation. The number of spark-pin pairs was therefore increased from 20 to 50. No change in behaviour was observed. It was again speculated that the energy loading was beyond the arcing limit of the gas. The pressure was therefore raised (in

the presence of increased preionisation), but no change in behaviour was observed. Likewise the lowering of the charging voltage had no effect other than that below ~11kV no discharge of any sort, including the preionisation, was observed. It was later learned, while working on the AEC built laser, that electrode condition is absolutely critical to laser performance. Small micro-protrusions on an electrode surface are sufficient to cause distortions in the electric field at these points. In accordance with the theory of streamer development presented in chapter two, streamer growth will concentrate around regions of increased field strength, such as is experienced around micro-protrusions, thus promoting arcing.

Possible factors counting against the UND laser were:

- High circuit inductance due to the handmade rolled foil capacitor.
- Stagnation of the gas due to limited gas circulation, which in hindsight might have been improved if a small circulating fan had been installed inside the laser vessel.
- Poor quality gas mix. The gas mix supplied for use with the laser was *not* research grade, and carried few identifying markings. It was unfortunately impossible to replace the gas mix with research grade gas.

However, it is believed that the poor condition of the two laser electrodes were the primary cause of the lasers non-performance since small scratch marks were clearly visible to the naked eye on the surface of the electrodes. Despite attempting to polish the surface of the electrodes, no improvement was observed in the performance of the laser. Fortunately, the performance of the AEC researched laser was significantly better. Significant factors counting for the AEC laser were:

- Much improved switching by means of the deuterium thyratron.
- Gas circulation by means of fans.
- Research grade gas.
- Lower inductance circuit.
- Quality industrial grade electronic components.

With this laser a reliable and repeatable homogeneous non-filamentary multiple streamer discharge was achieved with every discharge. Arcing was observed only when the number of discharges per second was increased to around twenty, where the gas circulation rate was too slow to replace the decomposition products between the electrodes with *clean* gas. The charging power supply was a 30kV unit and therefore could not be raised above the 30kV limit in order to observe the onset of arcing due to the overloading of the gas. However, it was possible to lower the voltage to 21kV and still achieve a stable discharge. This was in accordance with the theory presented above, where the self sustained discharge potential was determined to be ~19kV.

Figure 3.6 shows the voltage measured across the laser head using Tektronix 6015 high voltage probe. This voltage waveform is similar to that reported by Denes and Lowke in that the voltage across the laser head is observed to rise until such point as the gas breaks down and conduction begins. Figure 3.6 indicates that the gas breaks down at ~43kV. The jagged appearance of the rising edge is due to the progressive breakdown of the spark-pins. Subsequent to the gas breakdown the measured voltage should drop to the self sustained discharge potential, which in this case was predicted to be ~19kV. The sampled waveform, however, indicates a self sustained discharge voltage of ~15kV. The oscillatory nature of the waveform is not understood, but was speculated to be as a result of the fact that it was not possible to measure the discharge potential directly across the laser electrodes. The closest that the voltage probe could be positioned to the electrodes was at the aluminium input plates, positioned directly above and below the laser vessel. Hence, the voltage was in fact measured across the electrodes and an undetermined quantity of series inductance.

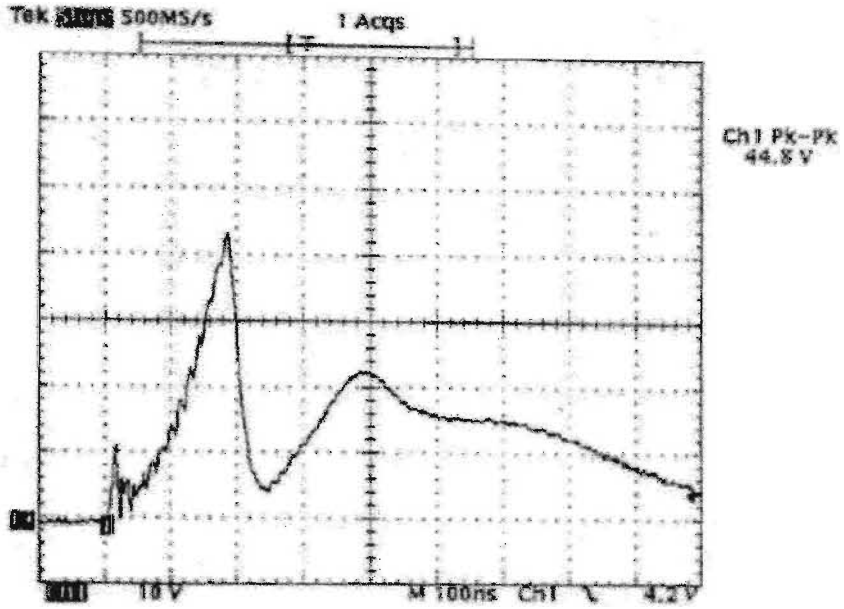

Figure 3.6 : Voltage measurement across the AEC TEA CO_2 laser head during a typical discharge. Vertical axis = 10kV/division, Horizontal axis = 100ns/division.

Since the laser electrodes *and* preionisation assembly were submerged in the laser vessel, it was not possible to measure the discharge current in isolation from the preionisation current. This was a physical impossibility since any object placed in or around the laser electrodes would have a) distorted the electric field and b) obstructed the preionisation. At a charging voltage of 30kV, an optical energy extraction of 6J was measured using a Vector SP50 pyroelectric joule meter. Wall-plug efficiency was therefore determined to be 6J/45J $\times$ 100% = 13.3%.

3.3 Conclusions

The theory of a volume stabilised glow discharge was discussed and results from two TEA CO_2 lasers presented. It was shown both in theory and in practice that the discharge formed at atmospheric pressure between the TEA CO_2 laser electrodes favours the formation of a filamentary streamer unless the pre-ionisation is precisely timed and the electrodes are of high surface quality and correct shape. Pre-ionisation was shown to be a successful means of promoting homogenous multiple streamer formation, otherwise termed a volume stabilised glow discharge. While the discharge is not a true glow discharge, the overlap of the multiple streamers causes the discharge to be both similar in appearance and electrical characteristics.

Basic calculations were performed to determine the self-sustained electrode discharge potential. For the gas mix and electrodes concerned the AEC manufactured laser was predicted to operate at a self-sustained voltage of 19kV. This proved to be difficult to measure, but appeared to occur at a potential closer to 15kV. To ensure a homogenous discharge, and consequently the efficient excitation of the medium, it was necessary to ensure that the electric field between the electrodes was uniform.

Chapter 4

The Arc Discharge

4.1 Introduction

Upon application of an electric potential of sufficient magnitude to cause the breakdown of a column of gas within a low pressure discharge tube, an electric discharge will commence in the manner described in chapter two. If, subsequent to the striking of the discharge, the current through the tube is restricted by a *ballast* resistor, then the discharge mechanism will be of the glow discharge or *Townsend* type. Primary electrons carried across the electrode gap (under the influence of the applied electric field) will generate secondary electrons both in the gap and at the cathode surface (due to the generation of secondary photons) which will impact upon the cathode surface. As the rate of removal of electrons from the cathode surface increases the discharge current will increase accordingly. However, by Ohm's law the potential across the ballast resistor will increase as the discharge current increases, and hence by Kirchhoff's voltage law the potential across the tube will decrease. As the initially applied tube potential decreases the production of secondary photons and secondary electrons will decrease until the production of electrons at the cathode will be balanced by the electric potential across the tube. The discharge will therefore be forcibly stabilised (regulated) since, owing to the ballast resistor, the flow of electrons from the cathode to the anode is restricted. Hence, the formation of streamers (which are typically associated with high electric field strengths) will be inhibited. The discharge will remain stabilised as long as the supply and ballast are connected.

When operated without a ballast resistor a discharge tube becomes a *flash-lamp*. Upon the application of an electric potential sufficiently high to cause the breakdown of the gas within the tube, the ohmic resistance of the gaseous medium will rapidly decrease (typically to around a few tenths of an ohm) until limited by the output impedance of the driving circuit. This differs little from the ballast limited case, with the exception that the output impedance of the driving circuit is significantly lower than a typical ballast resistor. Hence, the electric field strength and current density associated with the discharge are expected to be significantly higher. Due to the higher field strengths the discharge will be filamentary and streamer formation will dominate the discharge mechanism. Due to the higher current density the discharge

will be particularly luminous, emitting infra-red, visible, and ultraviolet light. A camera flash is a common example.

Large flash-lamps are commonly operated from pulsed power supplies. A charged capacitor may, for example, be discharged into a flash-lamp via a suitably fast closing switch, such as a spark-gap, ignitron or thyratron. Since the discharge is a transient no *single* stable electrode potential will be reached due to the *continuously* time varying current through the tube. When the energy storage capacitor is drained the discharge will cease, subsequent to which the resistance of the discharge column will rapidly increase and the flash-lamp will return to the non-conducting state. The continuous flow of current through a flash-lamp is not anticipated due to a) the magnitude of the current drawn by the tube in the absence of any ballast, and b) the temperature to which the lamp would be heated. Such discharges are however common in *arc furnaces*, where the discharge is unconfined and the heat of the discharge may be dissipated.

To understand the electrical behaviour of a filamentary arc-discharge formed inside a flash-lamp the work of Dishington, Hook and Hilberg [**11**] was studied. Based on this work a mathematical model was constructed to assist in the design a suitable test flash-lamp. The lamp and pulsed power supply was then constructed. Xenon gas was chosen to fill the lamp in accordance with the work of Frungel [**12**]. Based on the knowledge that a flash-lamp would emit UV due to streamer formation it was decided that the UV output of the lamp would be sampled in order to track the time histology electron-specie interactions within the filamentary discharge column.

4.2 The Flash-Lamp

The work of Dishington *et al* [**11**] describes the lamp as a non-linear ohmic resistance described according to the resistivity of the plasma as a function of the lamp current density and the diameter of the conductive filamentary arc down the inside of the lamp bore. Unlike other models the method of Dishington does not *assume* the filament diameter to initially conform to the inner bore of the lamp tube, but have shown the filament diameter to grow progressively to the inner diameter of the tube over time as a function of the energy deposited into the lamp. For long duration pulses the method of constant discharge diameter is useful since the duration over which the arc grows is negligible compared to the total flash duration. However, for the purposes of a short pulse model, the inclusion of the filament diameter is necessary. The work of Dishington *et al* is based on the work of Goncz [**13**], who showed that for an arbitrary selection of xenon flash-lamps the resistivity of the lamp is related to its current density according to:

$$\rho = \frac{1.13}{\sqrt{|j|}} \,, \tag{4.1}$$

where ρ is the resistivity of the conducting portion of the lamp in Ωcm and j the current density in A/cm^2. The multiplying factor in equation 4.1 was shown by Goncz to be only a weak function of the gas pressure and hence was assumed by Dishington *et al* to be a constant. Dishington *et al* substituted Goncz's relation into the equation for the resistance R of a conducting cylinder in Ω's of diameter d in cm, length l in cm, and resistivity ρ in Ωcm, given by:

$$R = \rho \frac{l}{\pi d^2 / 4} \,, \tag{4.2}$$

and determined the resistance R_f of a flash-lamp of time varying filament diameter d_a to be:

$$R_f = 1.28 \frac{l}{d_a} \times \frac{1}{\sqrt{|i|}} \,, \tag{4.3}$$

where i is the flash-lamp current as a function of time in Amperes.

The equivalent flash-lamp discharge circuit reported upon in this text is shown in figure 4.1. In accordance with the work of Dishington *et al* the flash-lamp was modelled as a variable non-linear Ohmic resistance R_f as a function of the time varying circuit current i. The circuit considered was a simple single mesh series RLC circuit. The capacitance C of the energy store was assumed constant. Since the flash-lamp filament diameter is never constant, neither is the inductance of the flash-lamp. However, since this contribution to the total series inductance is negligible, the stray circuit inductance, including the inductance of the capacitor, was considered constant, denoted L. Owing to the finite resistivity of the conductors the model included some finite resistance, denoted R_s, placed in series with the time dependant lamp resistance, denoted R_f.

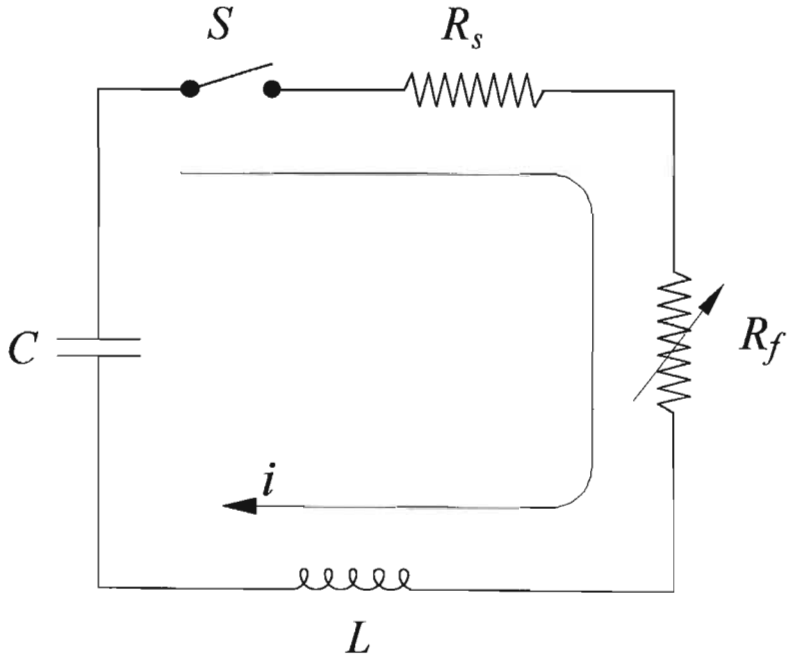

Figure 4.1 : The single mesh RLC flash-lamp circuit.

4.3 A Numerical Model

The analysis of the above circuit is presented in Appendix A. The relevant differential equations derived during the analysis of the circuit were solved using the Runge-Kutta-Fehlberg numerical method. The method was implemented using the MATLAB programming language in MATLAB-5 for Windows™. The program code is contained in appendix B. For the model to remain stable i (and hence I) were at all times kept non-zero. Hence the value of i at $t = 0$ had to be a finite value, corresponding to the small finite amount of energy deposited into the lamp in order to strike the lamp. Typically:

$$I_{(0)} \approx 5 \times 10^{-3} \tag{4.4}$$

and

$$\sigma_{(0)} = 8\frac{l}{V_o} \ . \tag{4.5}$$

The initial value of $\dot{I}$ was determined from equation A.11 (Appendix A) using equations 4.4 and 4.5.

The output of the above model was examined at 50cm electrode separation and various lamp bore diameters. C, the discharge capacitor, was eventually set to 470nF and 1μH of inductance was assumed at all times. A peak current of 38kA was predicted to flow through a 50cm long, 1.4cm diameter lamp at 12kV operating voltage. Current rise-time was predicted to be ~1.3μs and full-width-half-maximum (FWHM) pulse duration ~1.7μs. The current waveform was predicted to be near to critically damped, Figure 4.2 shows the modelled discharge current for a 30mbar xenon flash-lamp of length 50cm and inner bore diameter 1.4cm operated at a discharge voltage of 12kV. Of note is the steady growth in the rate of change in current predicted shortly after $t=0$. This is typical of a flash-lamp and has been explained by Dishington *et al* [**11**] as due to the growth in filament diameter as energy is deposited into the tube. Other models which assume a fixed filament diameter do not display this characteristic. The method of Dishington is therefore considered unique.

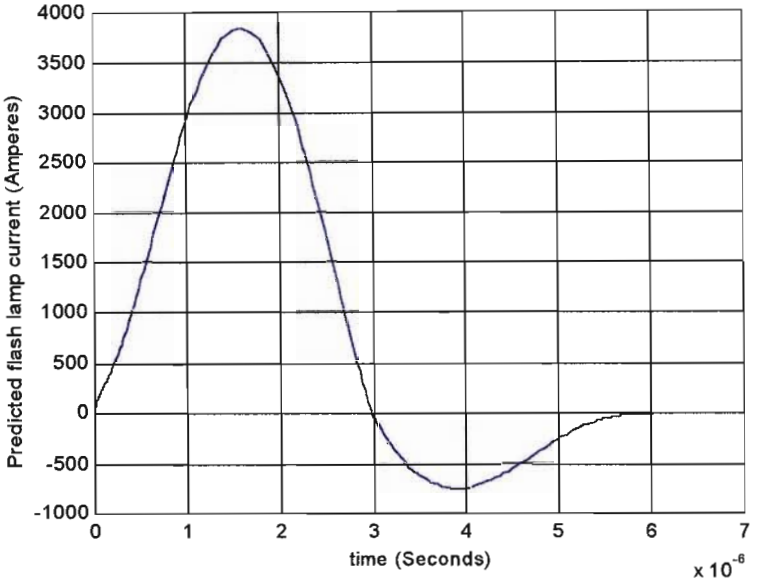

Figure 4.2 : Predicted discharge current through 50cm x 1.4cm flash-lamp as a function of time. C=470nF, L=1μH, R_s=25mΩ, Vo=12kV.

Figure 4.3 shows the predicted flash-lamp resistance during the breakdown of the discharge column. The graph is asymptotic to the vertical axis at $t = 0$. This is as to be expected since prior to $t = 0$ the resistance of the lamp is near infinite as it is in a non-conducting state.

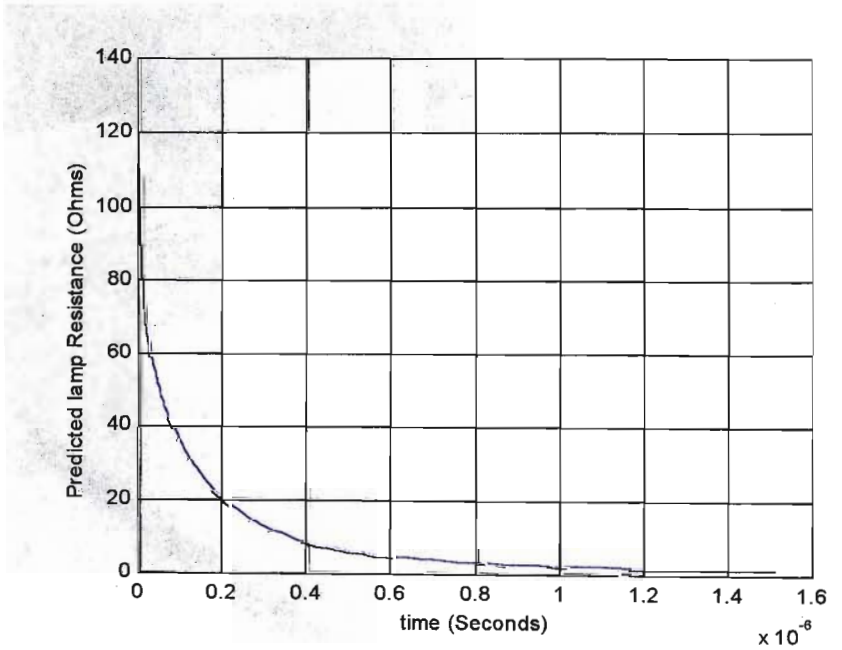

Figure 4.3 : Predicted resistance of a 50cm x 1.4cm flash-lamp discharge column as a function of time. C=470nF, L=1μH, R_s=25mΩ, Vo=12kV.

4.4 Results

A 50cm long × 1.4cm diameter quartz flash-lamp and pulse discharge circuit was manufactured in order to verify the above model. The flash-lamp was manufactured from a 40cm length of 1.4cm inner diameter quartz tubing fused to two 5cm pre-formed quartz to molybdenum end pieces. Thorium impregnated tungsten electrodes, chosen for their low work-function, were inserted inside the quartz to molybdenum end pieces and fused in place with an electron beam welder. An approximately 30cm length of ¼" copper piping was attached to the end of one of the electrodes in order to facilitate the evacuation and loading of the xenon gas. The flash-lamp was heated to 450°C at a pressure of 8×10^{-7}mbar for two days in order to bake out and de-gas the vessel interior. An industrial three phase furnace was used to heat the lamp and a turbo-molecular vacuum pump to evacuate the lamp vessel. Once cooled, the lamp was loaded to 30mbar with research grade xenon. The flash-lamp discharge circuit was manufactured from a 470nF, 40kV Maxwell capacitor and an English Electric Valve Company BK472 ignitron as a switch. At least 1μH of inductance was expected due to the predetermined inductance of the capacitor (a double ended device) and its connectors. The circuit geometry was coaxial in order to minimise unwanted stray circuit inductance. The manufactured flash-lamp and flash-lamp circuit is shown in figure 4.4.

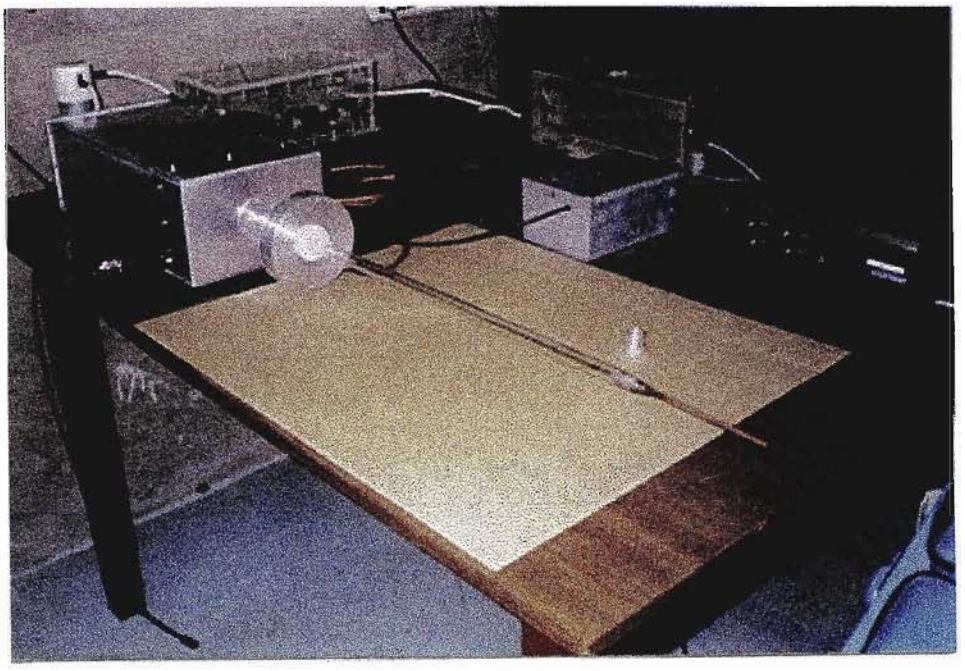

Figure 4.4 : The 50cm x 1.4cm manufactured flash-lamp with pulsed power supply. The flash-lamp return conductor was removed so as not to obscure the flash-lamp.

The flash-lamp current and UV emission were examined over a range of charging voltages in order to gauge the accuracy of the model. A good comparison between predicted and measured currents was observed. The flash-lamp current was measured using a Rogowski coil manufactured for the apparatus in accordance with the method described in chapter 7 of this thesis. The Rogowski coil is positioned at the base of the flash-lamp in figure 4.4. The circuit inductance was experimentally determined to be 1.2μH, 200nH larger than that predicted. The circuit capacitance was experimentally determined to be 440nF, 30nF lower than the indicated value on the capacitor. Figure 4.5 shows the measured current at a discharge voltage of 12kV. This compares well to the predicted wave form shown in figure 4.2.

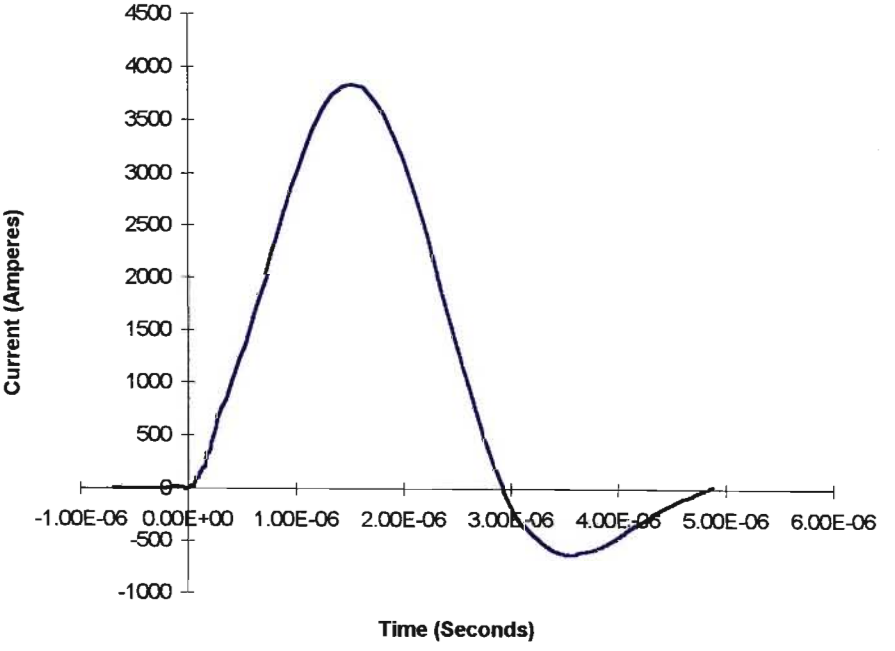

Figure 4.5 : Measured flash-lamp current for a 50cm x 1.4cm flash-lamp as a function of time. C=440nF, L=1.2μH, Vo=12kV.

The superimposed flash-lamp current and UV emission (in relative units) are shown in figure 4.6. The relative UV output was measured using a UV Corion band-pass filter placed over a silicon photo detector with quartz window. The output was amplified using a fast op-amp circuit and displayed on a Tektronix THS-720 storage oscilloscope.

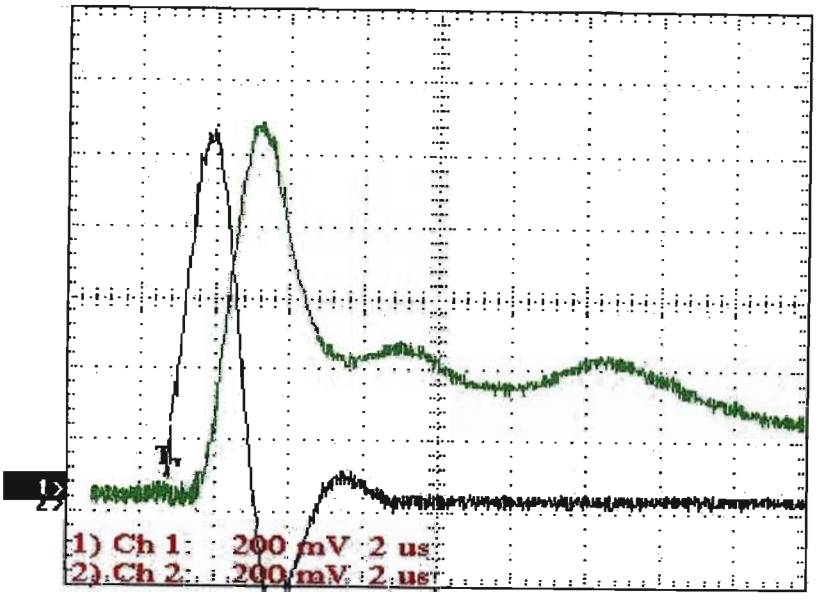

Figure 4.6 : Discharge current (black) through a 50cm × 1.4cm 30mbar xenon flash lamp and UV emission (green) in relative units as a function of time. X-axis = 2μS/div. Y-axis is arbitrary. C=440nF, L=1.2μH, Vo=12kV.

Figure 4.6 indicates that the radiated UV followed the rising edge of the current pulse by a delay of ~1.3μS. Measurements performed over a longer time scale indicated that the radiated UV continued for up to 40μS after the lamp current had ceased. In his review of xenon filled flash-lamps Frungel [**12**] refers to this as *after-glow*, an effect which may be attributed to the typical period over which electrons are re-paired with ions as a function of the gas pressure, gas type, and degree of ionisation.

Figure 4.7 shows the measured relative UV output as a function of the input electrical energy. Measurements were performed at a charging voltage of between 5kV and 12kV at 1kV increments. Figure 4.7 indicates that beyond an input electrical energy of 15J per event, the UV output increases linearly with an increase in input electrical energy. This is in accordance with the theory of a black body radiator *provided* the spectral bandwidth occupied by the total lamp output encompasses that of the detector. Since the lamp spectrum is typically wide this was most likely the case. This was further verified when at low input energies (below 10 Joule) little or no UV output was measured in spite of a very obvious and very bright visible discharge. This was due to the fact that at low input energies the spectral output of the lamp fell below that of the pass band of the UV detector.

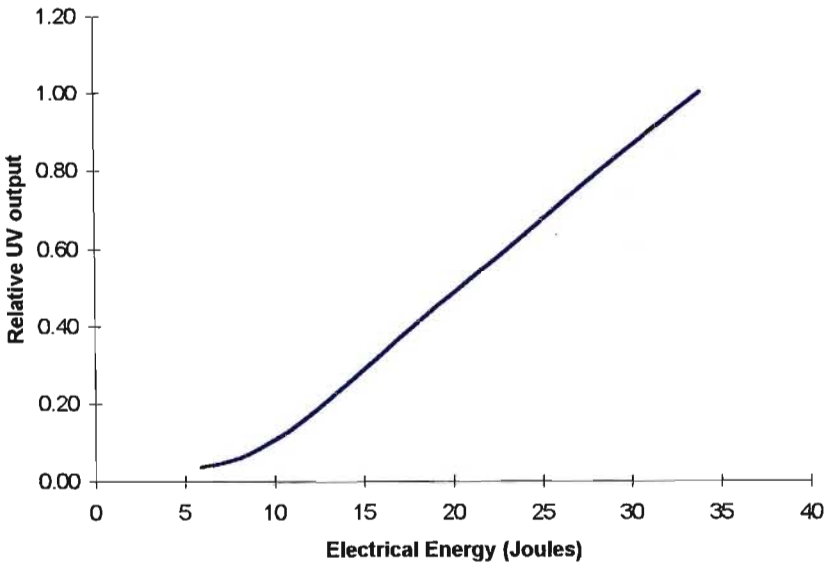

Figure 4.15 : 500 mm × 14 mm 30 mbar xenon flash lamp relative UV output as a function of input electrical energy. C=440nF, L=1.2μH, Vo=15kV.

In accordance with the theory of a black body radiator, as the input energy was raised, the spectral output of the flash lamp extended to include shorter wavelengths. Hence, both the total light output and the relative UV emission was observed to increase with increased input energy. Beyond that point at which the detectors pass band was encompassed by the lamp output, the rise in measured UV increased linearly with increased energy dissipated into the lamp.

4.5 Conclusions

The theory of the arc discharge was examined in order that a pulsed flash-lamp be designed and manufactured. The relevant theory has been presented and a mathematical model constructed using the MATLAB mathematical programming language. A flash-lamp and pulsed power-supply was constructed and measurements of the discharge current presented. The measurements were compared to the predictions obtained from the model. The model was shown to provide a reasonable mathematical description of the processes believed to occur within the arc discharge through the flash-lamp discharge tube. In accordance with the work of Dishington *et al* the rate of increase in the discharge current was shown to increase during the expansion of the discharge column inside the quartz lamp body. A peak current of 3.8kA was both predicted and measured.

Chapter 5
Surface Corona

5.1 Introduction

A corona discharge is typically observed around a stressed dielectric material under the influence of a strong electric field at 1 atmosphere pressure. Visible and ultraviolet (UV) emission results when the electric field strength is sufficient to transfer electric charge *to* or *from* the dielectric. For example, under the influence of a strong electric field, charge will be leaked from the tip of a sharpened conductor into the surrounding atmosphere [**15**]. The surrounding atmosphere (although generally classed as an insulator) will contain at least a few free electrons and ions which will be attracted to or repelled from the charged conductor under the influence of the applied electric field. Accelerated electrons will produce secondary electrons and photons due to collisions with other specie in their path, as discussed in chapter two, and a visible discharge will result. The production of secondary electrons guarantees the further flow of charge towards the tip of the charged conductor.

The specific corona discharge investigated and reported upon in this chapter is that caused to form around a dielectric slab placed between two flat electrodes. This is referred to as a *surface corona discharge*. Through the careful selection of the dielectric material a surface corona discharge may be caused to occur at a lower electric potential than a conventional corona discharge into open atmosphere since the electric field strength necessary to cause the onset of the corona may be generated through the choice of a dielectric material with a) high electric permittivity and b) good breakdown characteristics. Aluminium-oxide (Alumina) and barium-titanate are two such materials. Under the influence of a sufficiently high electric field either a) polar molecules within the dielectric will align themselves with the applied field, or b) non-polar molecules will deform sufficiently to become polar. If the rate of change of field strength is sufficiently high (~10^{12}V/s), electrons covering the surface of the dielectric may be sufficiently accelerated to momentarily break away. If one of the electrodes is porous, a wire grid for example, then a corona discharge will be observed to occur as electrons are accelerated away from the open areas of the dielectric towards the sharp edges of the positively charged grid. Likewise, if the grid

is negatively charged, electrons will be accelerated from the wire grid onto the dielectric surface.

Figure 5.1 shows a cross-section of a typical surface corona apparatus. The plate attached to the underside of the dielectric is typically grounded, while the upper grid may be raised to an extreme positive or negative potential.

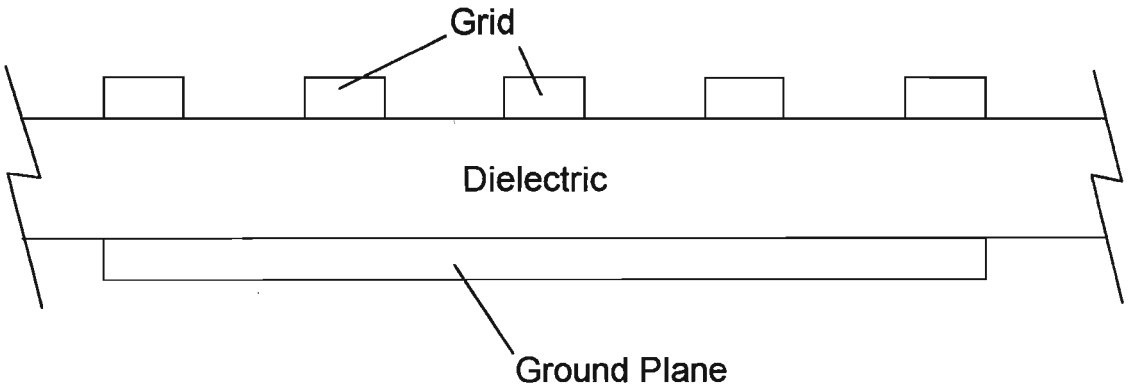

Figure 5.1 : A cross-section of a corona discharge apparatus.

5.2 The Surface Corona Discharge

An equivalent circuit of a *surface corona discharge*, based loosely on the work of Larsson [**16**], is shown in figure 5.2. The capacitance of the electrode-dielectric assembly, denoted C_O, was determined as a function of the surface area of the grid, surface area of the lower plate, thickness of the dielectric, and dielectric permittivity. In the absence of a corona discharge the circuits behaviour was dominated by the electrode-dielectric capacitance C_O. The capacitance of the dielectric surface onto which charge is deposited or withdrawn *during the discharge* was denoted C_G. Capacitance C_G can was determined in a similar fashion to C_O.

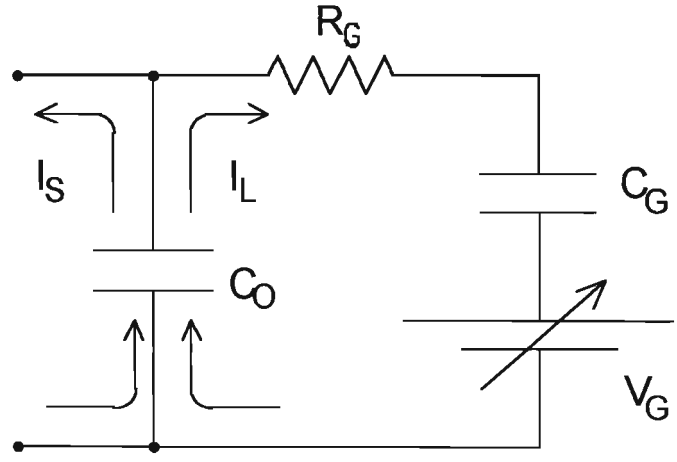

Figure 5.2 : The implemented equivalent circuit of the corona load.

As per the work of Larsson [**16**], the discharge was approximated by a barrier potential, denoted V_G, connected in series with an energy consuming (resistive) element, denoted R_G. Prior to the onset of a discharge no current may flow through resistor R_G. Hence, barrier potential V_G was defined such that if $\left|V_{C_O} - V_{C_G}\right| > V_{ion}$, then $V_G = V_{ion}$, else $\frac{dV_G}{dt} = \frac{dV_{C_O}}{dt}$. where V_{ion} is that potential above which electrons will possess sufficient kinetic energy to leave the surface of the dielectric slab or grid, and traverse the gap between the two. V_{ion} is commonly referred to as the *corona potential*. Under the conditions of a corona discharge the combination potential barrier and resistor is an effective model. However, if a streamer discharge were to form, the discharge potential, effectively V_G, would become a non-linear function of the discharge current. However, owing to the low current density and the large surface area of the corona apparatus, the above holds approximately true.

Note, potential barrier V_G is by definition a *sink* of energy, and cannot operate as a *source*. Hence, at no time is the law of conservation of energy violated. V_G is effectively the potential that must be *exceeded* in order to dissipate energy into the corona (that is to say dissipate energy in resistor R_G). The product of V_G and the current flowing through V_G was used to verify that the direction of power flow was indeed *into the corona*, as stated. Secondly, unlike the *point source* corona discharge, where charge is disseminated out into the surrounding atmosphere, the surface corona discharge cannot continue *ad infinitum*. When a potential sufficient to cause the onset of the corona discharge is applied to the apparatus, capacitance C_G will begin to charge. As capacitance C_G charges the potential difference over the discharge resistance R_G will decrease until such point as the discharge ceases. Capacitor C_G is then fully charged. In the case of the point source corona discharge, the capacity of the surrounding atmosphere is near infinite. Charge is simply absorbed by the atmosphere and carried away. In the case of the surface corona discharge the capacity of the dielectric is *finite!* Hence, the greater the permittivity of the dielectric, the higher the resultant capacitance, the longer the corona discharge may be sustained. In order to extend the duration of the corona discharge the electrode potential can be increased with time. However, since the voltage cannot be raised *ad infinitum* the discharge will eventually terminate. In order to achieve *at least* a quasi-continuous corona discharge, capacitor C_G can be charged in the reverse direction when the charging in the forward direction is complete. In this way the movement of electrons *to* and *from* capacitor C_G can be maintained, and, as long as these electrons are forced to flow through the corona resistance R_G, the corona discharge will be sustained.

In order to model the behaviour of the corona two currents were defined; I_S and I_L, where I_S was the current flowing from an external current source into capacitor C_O, and I_L is the load current flowing from C_O into capacitance C_G and potential barrier V_G. The direction of these two respective currents is defined in figure 5.2. The voltage across capacitance C_O was determined from Coulomb's law according to:

$$\frac{dV_{C_O}}{dt} = \frac{I_S + I_L}{C_O} \qquad \textbf{(5.1)}$$

Similarly the voltage across capacitance C_G was defined according to:

$$\frac{dV_{C_G}}{dt} = \frac{I_L}{C_G} \tag{5.2}$$

The potential barrier V_G was therefore written as:

$$\frac{dV_G}{dt} = -k_{VG} \times \frac{dV_{C_G}}{dt} = -k_{VG} \times \frac{I_L}{C_G} \tag{5.3}$$

where the constant k_{VG} was defined according to:

$$\begin{aligned} k_{VG} &= 1 \quad , \quad V_G < V_C \\ k_{VG} &= 0 \quad , \quad V_G \geq V_C \end{aligned} \tag{5.4}$$

Equations 5.3 and 5.4 ensure that the potential barrier V_G will increase at the same rate as the voltage across capacitor C_O, until such time as the corona potential V_{ion} is reached. At that point V_G is prevented from increasing any further by setting the constant k_{VG} to zero. According to Kirchhoff's voltage the sum of the voltages around current loop I_L was written as:

$$\frac{dI_L}{dt} = \frac{-1}{R_G} \times \left(\frac{dV_{C_O}}{dt} + \frac{dV_{C_G}}{dt} + \frac{dV_G}{dt} \right) \tag{5.5}$$

Equations 5.1 to 5.5 are the state equations required to describe the electrical operation of the corona discharge. The solution to these equations, in conjunction with the equations required to describe the current source which supplies current to the corona apparatus, enable the currents I_S and I_L to be calculated, and hence the power dissipated into the corona to be determined.

Note, while the corona potential V_G (in air) is a function of altitude and humidity, C_O and C_G are a function of the corona electrode geometry and dielectric material.

5.3 A Corona Current Source

To study the electrical behaviour of a corona discharge and facilitate a comparison between results and predictions a corona current source power supply was designed and constructed. The block diagram of the chosen power supply is shown in figure 5.3. In order to maintain a quasi-continuous corona discharge the power-supply was designed to supply current to the discharge in a cyclic fashion. The power-supply was therefore an alternating current (AC) device. To keep the design cheap and compact a high frequency switching power-supply design was chosen over the low frequency linear AC power-supply described in the work of *Feng* et al [**17**]. The power-supply design was an original design loosely based on the work of Chrysis [**18**]. More specifically a *buck-derived converter* was employed to supply between 300v and 450v DC (adjustable) to a resonant half-bridge converter, which in turn drove current into the corona discharge through a high voltage, high frequency, ferrite core, step-up transformer. The circuit operation was controlled and monitored by a control circuit which employed integrated circuits common to other switching power supplies. The control circuit comprised the usual oscillator, power transistor drive electronics and voltage and current monitoring. The control circuit was indeed elementary and controlled the switching actions of the power circuitry in a simple and effective manner.

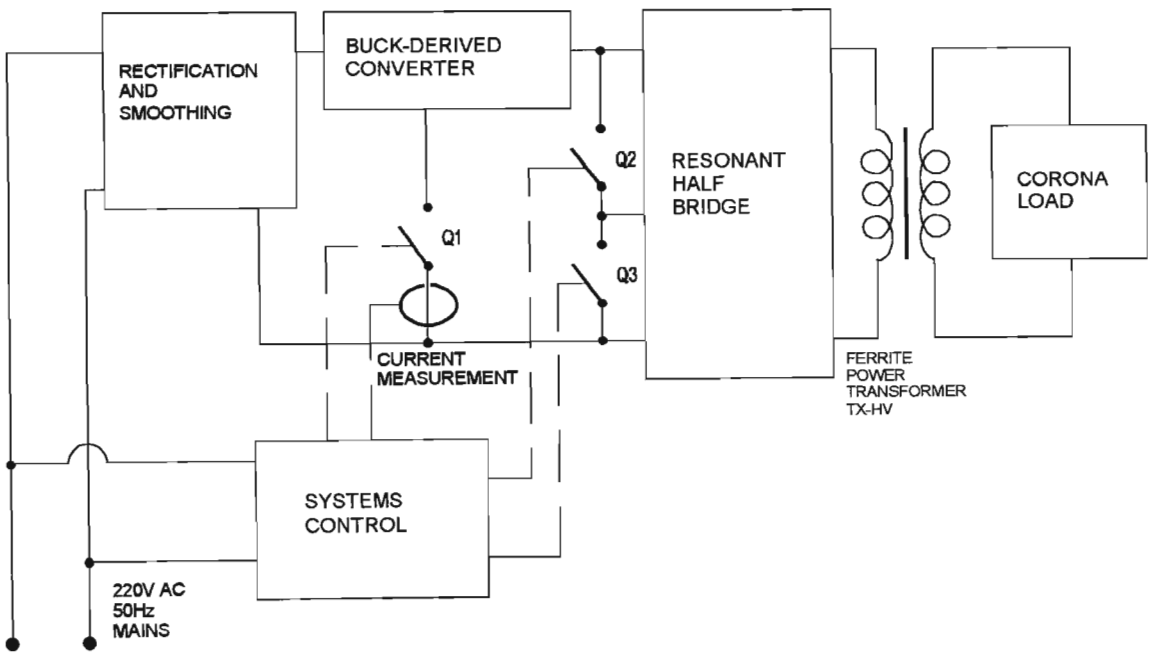

Figure 5.3 : A block diagram of the high frequency corona discharge current source.

The half-bridge converter was operated in a resonance with the corona load. Since the load characteristic of a surface corona apparatus is predominantly capacitive prior to the onset of the corona discharge (that is to say before the voltage is sufficiently high for electrons top be ejected) it was logical to facilitate the resonant transfer by including an *energy storage inductor* in the half bridge design. The inductor was resonantly coupled to the capacitance of the corona apparatus through the ferrite transformer. However, due to the non-linear behaviour of the corona discharge, the discharge current was not expected to be sinusoidal in nature. Since a *surface* corona discharge cannot be sustained without the continued increase in the voltage applied to the electrode geometry (causing the further movement of charge over the dielectric surface) it was a requirement that the voltage across the apparatus be reversed in order that the next corona discharge commence (subsequent to the recharging of the energy storage inductor). That is to say, the charge redistribution over the dielectric surface was reversed. By repetitively redistributing charge over the dielectric surface the corona discharge was expected to appear as a continuous *glow* discharge. The repetition rate (discharge frequency) was expected to be both a function of the supplies output power, and the ability of the corona discharge to draw current from the supply. It was intended that the repetition frequency be maintained above 20kHz in order to avoid the generation of uncomfortable audible noise due to magnetostriction in the ferrite components. The complete design of the corona discharge power supply is presented in Appendix C.

5.4 A Numerical Model

To facilitate the analysis of the corona power supply and make predictions with regard to the electrical operation of the corona apparatus, a mathematical model was constructed. From figure C.1 (Appendix C) and by Kirchhoff's voltage law:

$$V_O = (L_P + L_2)\frac{dI_P}{dt} + M\frac{dI_S}{dt} + R_P I_P + V_{C_P} \qquad \textbf{(5.6)}$$

where I_P and I_S are the transformer primary and secondary currents respectively, V_O is the supply voltage (measured at the output of the buck-derived converter), L_2 is the storage inductor, L_P is the self inductance of the primary winding of the transformer, M is the mutual inductance shared between the primary and the secondary windings, R_P is the resistance of the primary winding,

$$C_P = C_6 + C_7 \qquad \textbf{(5.7)}$$

and, by Coulomb's law:

$$\frac{dV_{C_P}}{dt} = k_{CP} \times \frac{I_P}{C_P} \qquad \textbf{(5.8)}$$

where:

$$\begin{aligned} k_{CP} &= 1 \quad , \quad 0 < V_{C_P} < V_O \\ k_{CP} &= 0 \quad , \quad V_{C_P} \le 0, \; V_{C_P} \ge 0 \end{aligned} \qquad \textbf{(5.9)}$$

Equation 5.9 models the clamping action of diodes D_2 and D_3, thus preventing the C_6-C_7 pair from straying beyond the limits of the supply rails. Since the corona load is attached to the secondary winding of the transformer, then again by Kirchhoff's voltage law:

$$L_S\frac{dI_S}{dt} + M\frac{dI_P}{dt} + R_s I_S + V_{C_o} = 0 \qquad \textbf{(5.10)}$$

where L_S is the self inductance of the secondary winding, R_S is the resistance of the secondary winding and V_{C_o} the voltage across the corona apparatus, as described in section 5.2.

Equations 5.1 to 5.10 are the state equations required to model the transfer of energy from the half bridge to the corona load. These equations, mostly ordinary differential equations, were solved simultaneously using the Runga-Kutte-Fehlberg numerical technique. The program code, listed in Appendix D, was implemented in the MATLAB™ programming language and run. Given that Q_3 was set *on* and Q_4 set *off*, V_O was set to between 310v and 450v DC (typically 310v if the buck-derived converter was idle). However, when Q_3 was set *off* and Q_4 set *on*, V_O was set to 0v.

Figure 5.4 shows a prediction of the transformer primary current and corona voltage for a particular discharge apparatus. The corona discharge was predicted to commence at ~1kV. The apparatus comprised two 150mm long × 100mm wide × 0.63mm thick aluminium-oxide slabs, relative permittivity μ_r = 5.0, copper plated on both sides. Approximately three-fifths of the one face was etched away with acid to form a number of open areas over which the corona could form. The capacitance C_O of the apparatus in the absence of any discharge, was predicted to be 1.2nF, while the remaining capacitance of the apparatus C_G, charged during the discharge, was predicted to be 2.1nF. Detailed component values are presented in Appendix C.

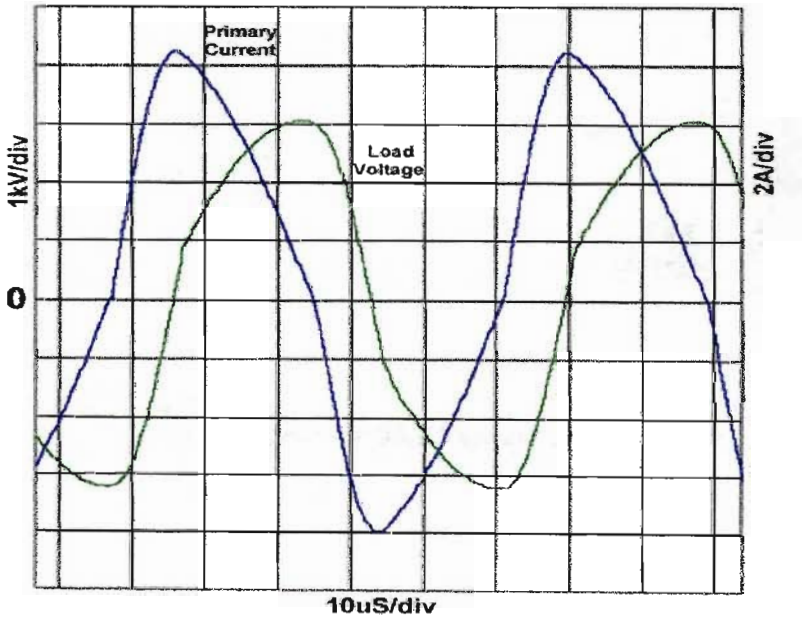

Figure 5.4 : A prediction of the power transformers primary current and the corresponding voltage across the corona discharge as a result thereof. Scale = 2A/div or 1kV/div on the Y-axis, and 10μS/div on the X-axis. Predicted peak voltage = ± 3kV and peak current = ± 8A.

5.5 A Manufactured Corona Power-Supply

Figure 5.5 shows the Mark-I power-supply manufactured in the University of Natal (UND) laser laboratory. The circuitry was built into the upper shelf of a renovated (butchered) filing cabinet. The basic circuit configuration was the same as that in figure 5.3. This particular power-supply, in spite of suffering many failures, served as a proof-of-principle device. One of the particular set-backs on this design was the method employed to generate the high voltage, a Cockroft-Walton multiplier, which was capable of generating its own corona discharge around its edges, regardless of any load! This design also employed a full-bridge in place of the later implemented half-bridge. At the time the full-bridge design was preferred due to its perceived higher power capability. It ran at 300W maximum continuous power. The half-bridge design eventually ran at 1kW and was less than a quarter of the size of the original power-supply, thus proving the initial assumption incorrect.

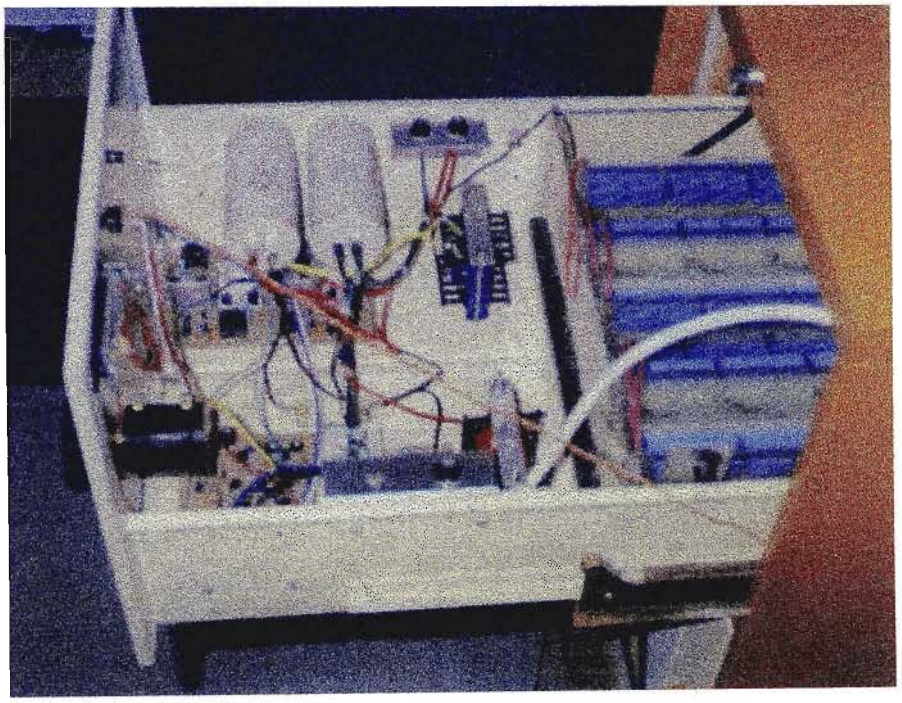

Figure 5.5 : The Mark-I power-supply manufactured at the UND laser laboratory.

Figure 5.6 shows the Mark-II power-supply manufactured at the Atomic Energy Corporation (AEC) Pulsed Power Radiation Research (PPRR) laboratory. The Mark-II power-supply was a refinement of the Mark-I device. Significant improvements included the replacement of MOSFET switching transistors with IGBT devices, an improved high voltage transformer design, and a substantial reduction in

weight and size. As with the Mark-I design, the circuit was divided into two circuit boards. The control circuit was mounted above the power delivery circuit. Switches Q_1, Q_2 and Q_3 were each mounted on their own heat-sink. The heat sensitive switch SW_2 was mounted on the face of the left hand heat-sink. The printed circuit boards (PCB's) were designed using the EASYTRAX™ program for PCB design.

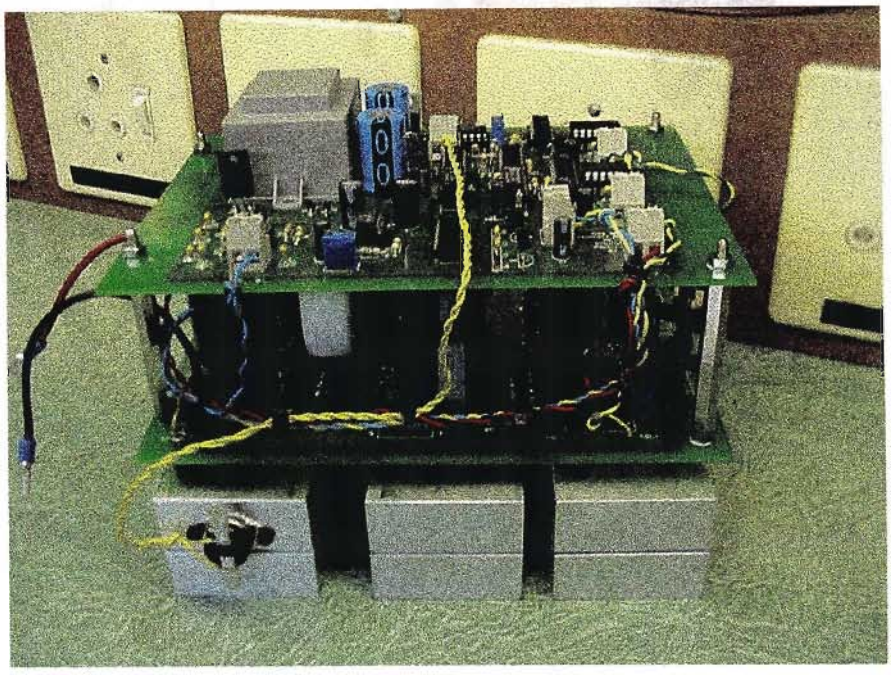

Figure 5.6 : The Mark-II power-supply.

The high-voltage transformer *TX-HV* is shown in figure 5.7. A 20 turn primary winding was wound in a single layer from 3 parallel 1mm diameter enamelled copper strands, 60 turns total, over a cardboard former. The former was made to fit over two U93/76/30 N27 Siemens ferrite U-cores. Packing-tape was used to hold the former together. A 240 turn secondary was wound in 2 layers from 0.4mm diameter enamelled copper wire. Approximately 160 turns on the first layer, the remaining 80 on the second layer. Three layers of 0.25mm Mylar insulating sheet were placed between the primary and the secondary, and between the two layers of the secondary. Copious quantities of enamel spray and fixative were used to secure the windings in place. The secondary was terminated in a 0.5m length of 10kV rated silicone wire.

Figure 5.7 : The high voltage power transformer mounted on an aluminium frame next to the power and control circuitry.

5.6 Results

Figure 5.8 shows a typical measurement of the current flowing through inductor L_2 into the primary of the transformer, and the voltage applied to the corona load as a result of this current. The current was measured using a small 3V/A Pearson current transformer. The voltage measurement was performed using a Tektronix P6015-A 1000:1 voltage probe with an input capacitance of less than 3pF. Measurements were recorded on a Tektronix TDS-320 digital storage oscilloscope.

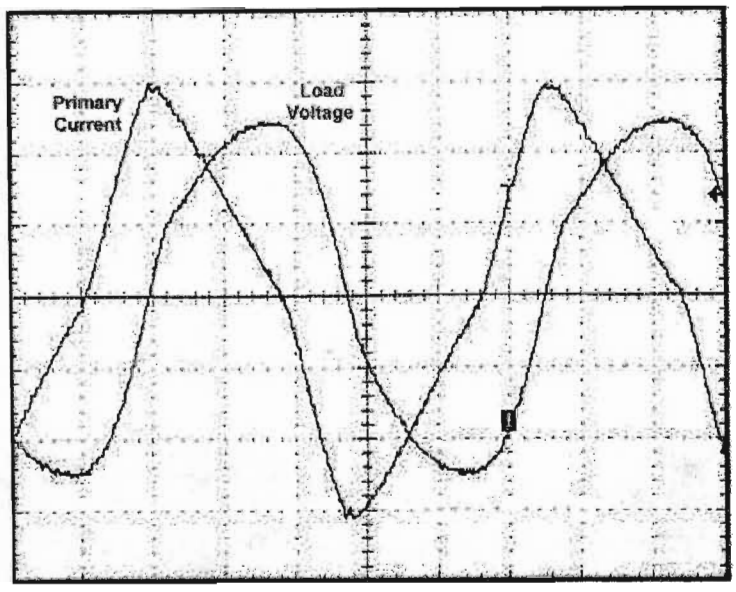

Figure 5.8 : A measurement of the transformers primary current and the corresponding voltage across the corona load as a result thereof. Y-axis = 3A/div and 1kV/div, X-axis = 10μS/div. Peak voltage = ± 3kV and peak current = ± 9A.

Figure 5.8 indicates that the corona discharge began when the supply voltage reached 1kV. This was in accordance with the output of the model, as shown in figure 5.4. During the rising edge of the current pulse no corona was observed to form. This was as intended during the charging cycle of inductor L_2. However, once charged, inductor L_2 was observed to transfer its energy through the transformer to the corona apparatus, causing the corona discharge to commence. For as long as inductor L_2 was able to deliver current to the corona, the voltage across the discharge was observed to increase. This was exactly as expected in accordance with the finite capacitance model. When inductor L_2 was exhausted, the cycle was observed to repeat itself in the opposite direction.

Figure 5.8 compares well with figure 5.4, indicating that the model is reliable. The model predicted a resonant frequency of 18.6kHz. This was slightly higher than the measured value of 17.9kHz. This was most likely due to the fact that the oscillator was not tuned to the exact resonant frequency of the circuit. Note, the frequency of the oscillator was preset and was not self-adjusting. The predicted peak primary current was also approximately an Ampere lower than the measured value of 9A. The predicted power dissipation into the corona load was 360W. Actual power consumption was measured by multiplying the 220VAC RMS supply voltage by the measured RMS current.

Figure 5.9 shows the corona discharge formed over the surface of the dielectric slab. The corona discharge was identified by its characteristic violet glow, and was observed to be a rich source of ultraviolet radiation and heat. The corona discharge was observed through a sheet of commercial soda-glass in order to prevent contact with the radiated UV.

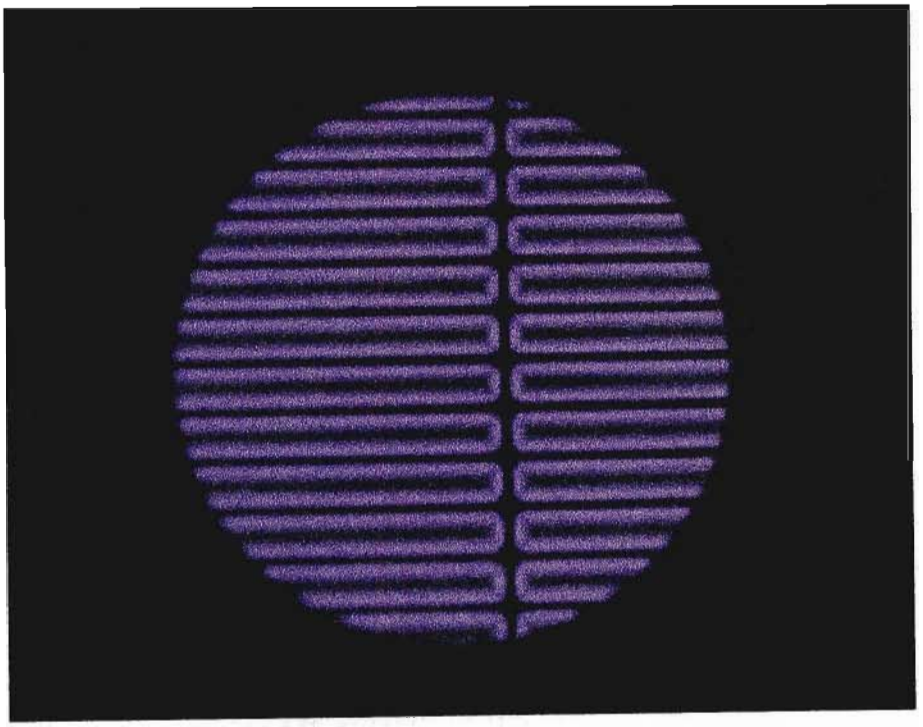

Figure 5.9 : A corona discharge over an aluminium-oxide dielectric slab.

More electrical power was delivered to the corona discharge by replacing capacitors C_6 and C_7 with larger values. However, in order to keep the resonant frequency above the audible frequency range the number of turns on inductor L_2 had to be reduced. Hence, the current through inductor L_2 and the transformer primary was observed to peak at an increased value. At a peak current of 24A it was possible to dissipate 1kW of power into the corona. Power dissipation above 1kW was not attempted due to the heating of inductor L_2 and the heating of the dielectric slabs. It was necessary to water cool the corona apparatus in order to dissipate the heat of the dielectric. Little or no heating of any of the power transistors was observed, probably due to the large heat-sinks to which the power transistors were attached.

5.7 Conclusions

The theory, design, manufacture and operation of a high voltage AC current source and surface corona apparatus has been presented. The design was implemented by method of a mathematical model constructed using the MATLAB mathematical programming language. A power-supply was constructed and measurements of the discharge current and voltage performed. The measurements were compared to the predictions obtained from the model. The model was shown to provide a reasonable mathematical description of the processes believed to occur within the surface corona discharge. The model accurately predicted the onset of the corona discharge at 1kV for the particular dielectric material and power-supply. As a result of the emphasis on energy transfer from inductor L_2 to the corona load, typical conduction and core losses were required to been minimised. The use of specialised low permeability high working magnetic flux density materials have enabled a substantial size reduction in the Mark-II design compared to the Mark-I design.

Chapter 6

A Magnetically Interrupted Vacuum Discharge

6.1 Introduction

An electric discharge is formed between two electrodes in vacuum when electrons are caused to leave the cathode and enter the discharge space. In vacuum few specie are available to promote ion formation due to electron-ion collisions. Hence, secondary emission of electrons from the cathode due to ion bombardment is limited. The mechanism of the vacuum discharge differs from that of the arc (streamer) discharge and glow (Townsend) discharge described earlier. If the electric field is sufficiently high electrons will leave the cathode as a result of field-emission. Field-emission is the term given the release of electrons from a cold cathode in vacuum as a result of an electric field sufficiently high to pluck electrons from the cathode surface. Field emission is dependant on electrode geometry and is unlikely to occur below 350kV/cm electric field strength in high vacuum ($>10^{-7}$torr). The probability of field emission is improved if the geometry of the cathode is sharpened in order to enhance the electric field around the electrode tip. Mesyats and Proskurovsky [**19**] describe in detail the mechanism of vacuum electrical breakdown under the headings of field electron emission; secondary emission of electrons, ions and photons; metal impurity particles; electric field pondermotive forces; non-metallic inclusion of films; and gas desorption.

In the absence of field emission a plasma of ions and electrons may be injected between the electrodes to trigger a discharge. Ions accelerated through the plasma due to the applied electric field collide with the cathode surface and stimulate electron emission. A flow of electrons from the cathode surface further promotes ion formation in the discharge space as a result of collisions with neutral specie. Some neutral specie accompany the plasma as a result of either insufficient ionisation in the plasma injection system (that is to say neutrals are injected into the gap) or recombination of ions and electrons in the discharge space. Electron-ion interaction in the gap results in a luminous discharge providing a source of photo-ionisation,

causing additional electrons to leave the cathode surface due to the photo-electric effect. If the electric field strength is sufficiently high ions are liberated from the anode surface as a result of electron bombardment. These ions are accelerated towards the cathode by the applied electric field and further bombard the cathode. However, the electron flux dominates the ion flux due to the lesser mobility of ions in comparison to electrons. The electron current caused to flow from the cathode to the anode is a function of three specific characteristics of the injected plasma, namely:

- The plasma ion density
- The plasma injection velocity (as a function of ion mass and ion mobility)
- The charge state of the ions

as well as the electric field strength between the electrodes.

Given that plasma is injected upon command the vacuum switch is made possible. The plasma closing switch is essentially a spark-gap switch operated in vacuum, with the major difference that the discharge is supported by electrode material rather than, in the case of the pressurised spark-gap, the filler gas. Ionised electrode material is commonly injected into the gap as a result of a small arc caused to occur between two small trigger electrodes recessed in either the anode or cathode. The rapid condensation of metal vapour onto the electrodes, after the discharge has ceased, permits the vacuum switch to recover in a few microseconds. Since the breakdown voltage of a vacuum switch is predominantly a function of electrode shape, rather than electrode spacing, the vacuum switch may be used reliably over a wide range of voltages. In some specialised cases the plasma source may be mounted adjacent to the gap equidistant from either electrode. Kristiansen and Hagler have extensively reviewed both pressurised and vacuum switches [**20**].

6.2 The Plasma Opening Switch

It is well known from z-pinch and plasma-fusion experiments that a magnetic field may be used to propel or confine a conducting plasma. The plasma opening switch (POS) is a vacuum switch in which the magnetic field associated with one or both discharge electrodes is used to drive the discharge out of the discharge space, causing the discharge to self-extinguish. The discharge is caused to terminate at a predefined current since the magnetic field strength necessary to drive the discharge out of the discharge space is an exact function of the electrode current. The functionality of the POS is therefore similar to that of a fuse. The POS has been experimented with as an alternative to the fuse opening switch (FOS), but is in general operated with a FOS as a complimentary device. The POS has four advantages over the FOS:

- The POS is reusable, provided the plasma source is reusable,
- The POS opens significantly faster,
- The POS can support a much greater current, and
- Less energy is expended into the POS than into the FOS in order to cause the switch to move from the closed to open circuit state.

Two POS geometries are popular, the coaxial POS and the parallel plate POS. For the purpose of this work a coaxial POS was investigated. Figure 6.1 shows the cross-section of a typical coaxial POS.

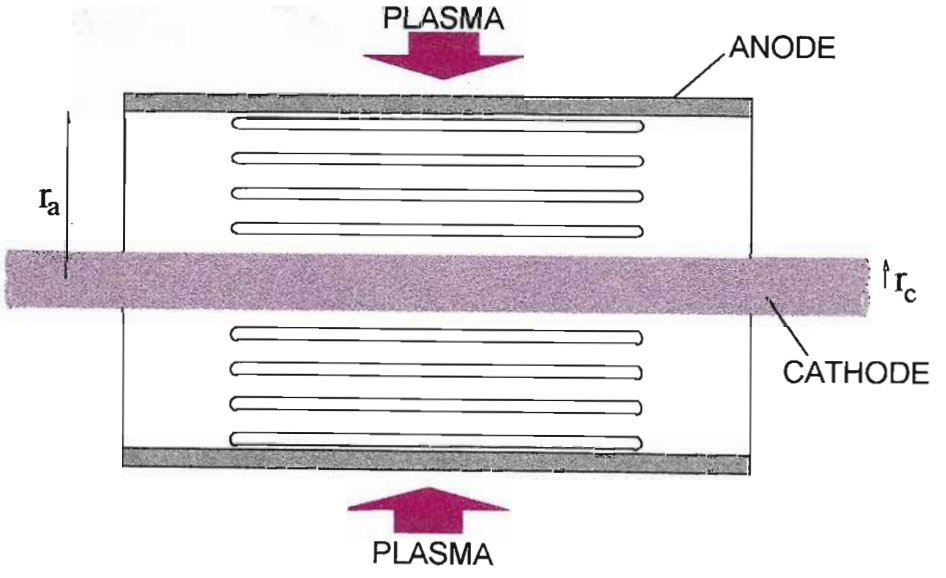

Figure 6.1 : A cross-section of a typical coaxial POS.

Figure 6.2 shows the POS manufactured and tested at the Atomic Energy Corporation (AEC) of South Africa's Pulsed Power Radiation Research (PPRR) laboratory. The POS comprised a cylindrical stainless steel anode positioned concentrically around a cylindrical brass cathode in high vacuum (~10^{-6}torr). The vacuum chamber was manufactured from Pyrex and stainless steel. Conduction between the anode and the cathode was supported by a carbon plasma injected from four concentrically mounted plasma guns. The anode was slotted in order that the plasma penetrate the gap between the anode and the cathode. While many such POS have employed the Mendel plasma gun [**21**] as a plasma source, most new POS have achieved significantly improved results using the flash-board method of T.J. Renk [**22**]. Four flash-boards were employed in this experiment.

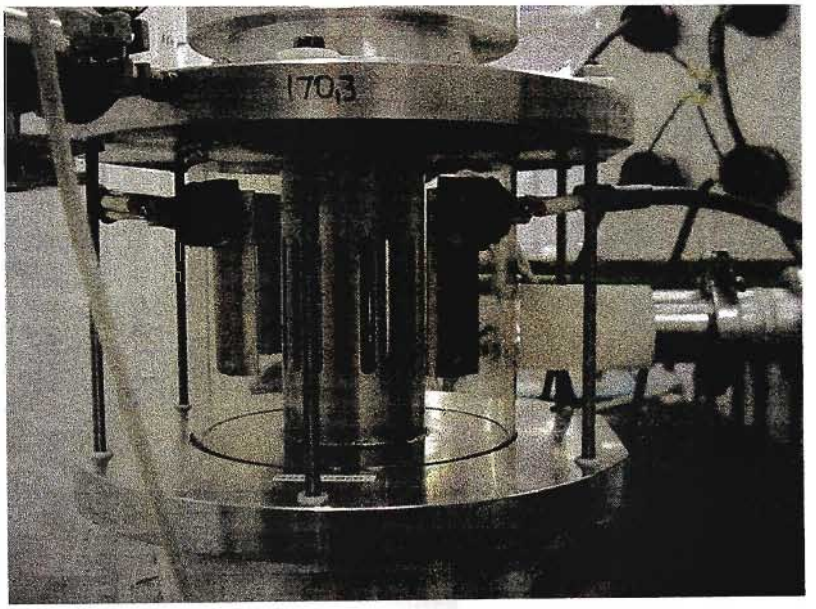

Figure 6.2 : An experimental coaxial POS manufactured and tested at the Atomic Energy Corporation (AEC). The slotted anode is clearly visible inside the glass vacuum chamber. The cathode is obscured from view by the anode.

As with all POS experiments a *generator* circuit was required to supply current to the POS, and a load circuit was required to draw current away from the POS subsequent to the termination of the POS discharge. To this end a pulsed discharge power supply was constructed from a high voltage capacitor bank and closing switch, and connected to the POS via a manufactured coaxial feed. The centre conductor of the coaxial feed was connected to the POS cathode and the outer conductor connected to the anode. A coaxial load was manufactured and attached

to the opposite end of the POS in much the same way as the generator. Conduction between the anode and the cathode was observed to be interrupted as a result of a bipolar space-charge limited discharge current, and the interaction between the cathode magnetic field (due to the cathode current) and the injected plasma. The POS was researched for use in applications requiring large peak current with fast rise time. Elsewhere POS have been considered for use with electron and ion beam experiments, pulsed microwave (MW) generation and electromagnetic pulse (EMP) simulation. A POS is a useful high power transient generator and a useful rise-time sharpening component in large current pulsed power supplies.

Ottinger *et al* [**23**], Commisso *et al* [**24**] and Hinshelwood *et al* [**25**] describe the behaviour of the POS according to four phases of operation: the *Conduction phase*, the *Erosion phase*, the *Enhanced Erosion phase* and the *Magnetic Insulation phase*. Each of these phases, detailed in figure 6.3, is identified according to the manner in which electrons cross from the cathode to the anode, and the properties of the plasma. The theory of POS operation, as it is generally accepted, is described in sections 6.2.1 to 6.2.4.

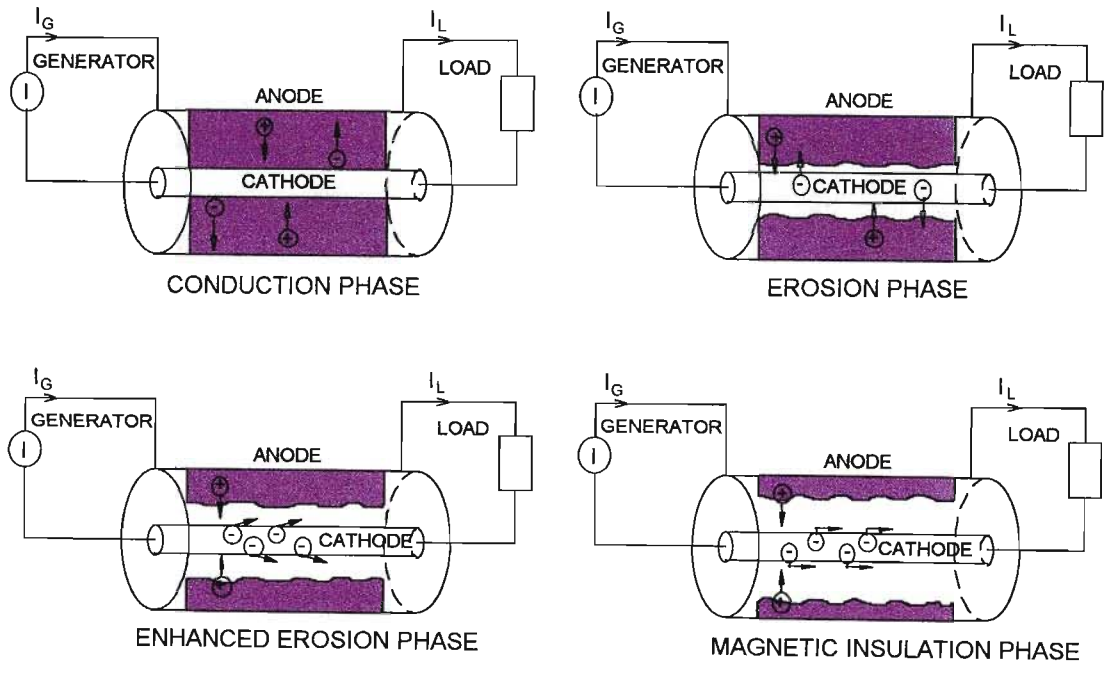

Figure 6.3 : The four phases of POS operation.

6.2.1 The Conduction Phase

At time $t=0$ a plasma of carbon ions and electrons of constant ion density n_i per cm^3 is injected through the porous anode, radius r_a cm, towards the cathode, radius r_c cm, travelling at an average velocity of v_d cm/s. The ions are assumed to form a homogenous cloud around the cathode. When the ions contact surface the cathode the generator is fired and an electron current is passed from the generator down the cathode into the discharge gap in a bipolar space-charge limited fashion described according to:

$$I_e = I_i \sqrt{\frac{m_i}{m_e Z}} \qquad \textbf{(6.1)}$$

where I_e and I_i are the electron and ion discharge current in Amperes, m_e and m_i are the electron rest mass and ion mass in kilograms, and Z is the predominant charge state of the carbon ions. For a C^{++} carbon plasma Z is 2. Equation 6.1 is not unlike equation 2.2, where the factor $\sqrt{\frac{m_i}{m_e Z}}$ may be compared to Townsend's second ionisation coefficient γ. Indeed, Shumacher and Harvey **[26]** term this the *secondary electron yield coefficient*, denoted γ_e, but do not relate γ_e to any *particular* process other than to say that it may range from a few percent to in excess of unity depending on the cathode material, cathode surface condition, ion mass, ionisation state of the plasma, and the cathode-sheath potential. The injected ion current is described as a function of its velocity, density and charge state according to:

$$I_i = n_i v_d A Z e \qquad \textbf{(6.2)}$$

where A is the time varying area of the electron emission surface in cm^2, and e the charge of an electron in Coulombs. When the electron current is small the radiating area A is small due to the low demand placed on the ion current. Hence only a small fraction of the total cathode surface area illuminated by the ion flux emits electrons. However, as the generator current is increased the radiating area A grows until the entire area of the cathode radiates electrons out into the ion flux.

Since the cathode is cylindrical:

$$A = 2\pi r_c l \,. \tag{6.3}$$

where l is the time dependant length of the electron emission surface. Combining equations 6.1, 6.2 and 6.3:

$$l = \frac{I_e}{2\pi r_c n_i v_d Ze}\sqrt{\frac{m_e Z}{m_i}} \tag{6.4}$$

The maximum sustainable electron current *during the conduction phase* is reached when $l = l_c$. Hence:

$$I_e = 2\pi r_c l_c n_i v_d Ze\sqrt{\frac{m_i}{m_e Z}}\ , \tag{6.5}$$

where l_c is the length of the cathode surface exposed to the ion flux. Equation 6.5 is commonly used to determine the discharge current at which switch opening commences.

6.2.2 The Erosion Phase:

Since the ion flux can support only a limited electron current, determined by equation 6.5, any increase in the generator current will cause electrons to collect around the cathode surface in a cathode-fall region, or *sheath*, thickness D. As more electrons collect in the sheath the sheath dimension increases, effectively causing the surface area A of the cathode to increase. Hence an increased electron current is supported depending on how fast the sheath expands and to what dimension. The surface area A_s of the sheath is a function of the electron current I_e and determined similarly to equations 6.4:

$$A_s = \frac{I_e}{n_i v_d Ze}\sqrt{\frac{m_e Z}{m_i}} \tag{6.6}$$

The sheath dimension D is determined from the sheath surface area A_s according to:

$$\begin{aligned} D &= r_s - r_c \\ &= \frac{A_s}{2\pi l_c} - r_c \end{aligned} \qquad \textbf{(6.7)}$$

where r_s is the radius of the sheath.

As the sheath grows an increasing number of mobile electrons accumulate in the sheath. Commisso *et al* state that the effect of the cathode magnetic field on these electrons can no longer be neglected when the sheath dimension D becomes comparable with the typical electron Larmor radius, and occurs when the switch current I_e approximates some critical current I_c, where:

$$I_c = 1.36 \times 10^4 \sqrt{\gamma^2 - 1}\frac{r_c}{D} \quad , \qquad \textbf{(6.8)}$$

and γ is the ratio of the electron energy to its rest energy. It is assumed that the energy of any electron entering the sheath is equivalent to its rest mass energy, until such time as it is accelerated by the respective electric and magnetic fields within the anode cathode gap. This is typical of a laminar flow.

6.2.3 The Enhanced Erosion Phase

At switch currents greater than that defined by equation 6.8 the electron flux crossing the discharge gap does so via the indirect route dictated by the sheath electric field and the cathode magnetic field. A consequence of the modified electron trajectory is the enhancement of the electron space-charge within the sheath and, as a result, the demand placed upon the ion flux increases beyond that determined by equation 6.1 such that, according to Commisso *et al*:

$$\frac{I_i}{I_e} \approx \sqrt{\frac{2m_e Z}{m_i}(\gamma + 1)} \times \left(\frac{l_e}{D}\right) \qquad \textbf{(6.9)}$$

where l_e is the length of the modified path followed by the electron flux. As a consequence the sheath expands faster in order to meet the additional demand placed on the ion flux. The enhanced erosion of the ion flux, as determined by equation 6.9, is believed to be responsible for the observed fast opening of the switch since it occurs over a time scale significantly shorter than the time period over which the magnetic field is be expected to sweep the discharge out of the discharge space.

6.2.4 The Magnetic Insulation Phase

The effect of the cathode magnetic field on the switch current is to modify the space-charge relation and increase the demand for ion flux by modifying the path of electrons into and through the sheath, causing the rate of switch opening to increase markedly. The greater the switch current the faster the ion flux is eroded. Hence the faster the switch opens. As long as the *erosion* and *enhanced erosion* phases are executed over a time period too short for the cathode magnetic field to drive electrons completely out of the sheath it is unnecessary to include the cathode magnetic field in a description of the switch opening, other than the modification of the space-charge relation. While not required to *open* the switch, the cathode magnetic field *is* required to *keep* the switch open. When the magnetic field due to the cathode current becomes sufficiently large that *no electron leaving the cathode may reach the anode*, the cathode is said to be magnetically insulated. The switch current is therefore zero. All electrons leaving the surface of the cathode move towards the load end of the POS where they either rejoin the cathode *en route* or collide with the load. The ion current is no longer enhanced since the electrons within the sheath are held close to the surface of the cathode. Since no electron may cross to the anode, the load current is equated to the cathode current plus the Laminar sheath current. As long as the generator is capable of delivering a current of this magnitude the magnetic field surrounding the cathode is sufficient to maintain magnetic insulation. However, when the generator current terminates the switch action fails and the POS returns to the prior conducting state until such time as the discharge is exhausted.

Note, equations 6.1 through to 6.9 describe the *ion current* as a function of the *electron current*. They do not describe the *electron current* as a function of the *ion current*. While the *ion flux* is a function of the injected carbon plasma and is assumed constant, the *ion current* is not since the area A of that portion of the cathode from which electrons radiate is variable, as is the surface area A_s of the sheath subsequent to the conduction phase.

The above theory ignores secondary effects between the anode and the cathode. These effects include:

- The formation of a dense cathode plasma around the cathode due to the accumulation of the injected plasma prior to the injection of electrons,
- The secondary emission of ions from the cathode surface, and
- The non-negligible axial movement of the injected carbon ions towards the load at long conduction times (typically >100ns).

6.3 The Long Conduction Time Plasma Opening Switch

The above theory fails to describe the operation of a POS at long conduction times. If the switch current is small then the erosion of the ion flux is slow, and sufficient time may elapse for the cathode magnetic field to *significantly* modify the movement of electrons in the sheath. Under these circumstances the migration of electrons from the cathode to the anode is described as a function of the switch electron current I_e, the cathode magnetic flux density $\mathbf{B}$, and the sheath electric field $\mathbf{E}$. An electron, charge q, travelling at velocity v through an electric field $\mathbf{E}$ and magnetic field $\mathbf{B}$ will experience a force equivalent to $\mathbf{E}+(q\mathbf{v}\times\mathbf{B})$, and is caused to follow a curved trajectory. If the cathode magnetic field $\mathbf{B}$ is sufficiently strong an electron leaving the POS cathode under the influence of the sheath electric field $\mathbf{E}$ may be caused to return to the cathode. When all electrons leaving the cathode are caused to return to the cathode, the cathode is said to be magnetically insulated from the ion flux.

Despite an extensive literature search no reference material describing the POS electron interaction with the cathode magnetic field was found. It was decided, therefore, that such a theory would be postulated based on basic principles. In order to model the sheath current it was necessary to:

- Determine the cathode magnetic field $\mathbf{B}$ as a function of the cathode current I_C.
- Calculate the sheath Potential V_r.
- Determine the movement of electrons in the sheath due to the sheath electric field $\mathbf{E}$ and cathode magnetic field $\mathbf{B}$.
- Determine the modified space-charge condition.

The following assumptions were made with regard to the sheath:

- The sheath has an electric permittivity ε and magnetic permeability μ equivalent to that of free space.
- The sheath potential V_r is the same as the electrode potential. This is in accordance with the work of Shumacher and Harvey and similar to the cathode-fall described in section 2.2.1.

- If the sheath potential V_r is less than that required to move a unit charge across the sheath against the cathode magnetic field **B**, then no switch current flows.
- Electron emission occurs across the entire length of the cathode, but contacts the incoming ion flux through a cylinder of length l_p, ($l_p < l_c$) where l_p is determined according to the calculated electron drift.

The postulated electron drift and resultant contact area with the ion flux is shown in figure 6.4.

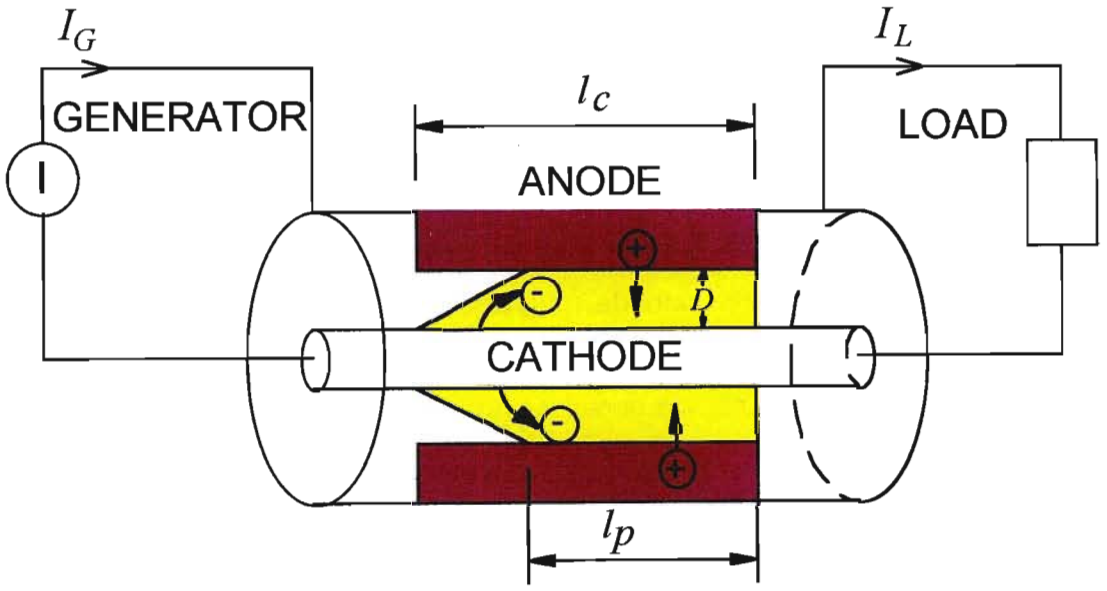

Figure 6.4 : If the erosion of the ion flux is sufficiently slow the trajectory of electrons moving through the sheath is significantly modified before the sheath current is terminated.

6.3.1 The Cathode Magnetic Field

The cathode magnetic field is a function of the cathode current. Since the cathode is the point of departure for electrons entering the discharge the cathode current is a function of distance along the cathode. The following assumptions were made with regard to the cathode:

- The cathode lies along the z-axis of the co-ordinate system.
- The cathode current is equal to the generator current I_G at $z=0$
- The cathode current is equal to the load current I_L at $z=l_c$, where l_c is the length of the cathode illuminated by the ion flux.
- The sheath current I_S is equal to the difference between the generator current and the load current, $I_G - I_L$.

Commisso *et al* state that electrons leave the POS cathode in a uniform manner. Hence, the current density was assumed constant over the surface of the cathode. The radial electron current density J_S at the cathode surface was written as:

$$J_S = \frac{I_S}{2\pi r_c l_c} = \frac{I_G - I_L}{2\pi r_c l_c} \tag{6.10}$$

where the sheath current I_s is the sum of the sheath electron current I_e and the sheath ion current I_i. The cathode current I_c was therefore described as a function of distance z along the cathode according to:

$$I_C = I_G - \frac{z}{l_c}(I_G - I_L) \tag{6.11}$$

The magnetic flux density **B** at any point around the cathode was described according to the sum of the magnetic field contributions due to three *zones*, namely:

- ZONE 1 - That region of the cathode along which the generator current I_G flows.
- ZONE 2 – That region of the cathode along which electrons are emitted and to which equation 6.11 applies.
- ZONE 3 – That region of the cathode along which load current I_L flows.

The three zones and the cathode are illustrated in figure 6.5. Using the Biot-Savart law it was shown that the density of the respective magnetic field components at some point **p** at distance *r* from the z-axis, due to zones 1 and 3 are:

$$B_1 = \frac{\mu I_G}{4\pi r}(\cos\alpha_1 + 1) \qquad \textbf{(6.12)}$$

$$B_3 = \frac{\mu I_L}{4\pi r}(1 - \cos\alpha_4) \qquad \textbf{(6.13)}$$

where angles α_1 and α_4 are indicated in figure 6.5. Angles α_1 to α_4 define the point **p** exclusively. Angles α_2 and α_3 were assumed to be π and 0 radians respectively.

The Biot-Savart law was applied to equation 6.11 in order to determine the density of the magnetic flux associated with zone 2. Since equation 6.11 is easily divided into two respective components, denoted *a* and *b*, the calculation was separated into two additional components:

$$B_{2a} = \frac{\mu I_G}{4\pi r}(\cos\alpha_4 - \cos\alpha_1) \qquad \textbf{(6.14)}$$

and

$$B_{2b} = -\frac{\mu}{4\pi}\frac{(I_G - I_L)}{l_c}\int_{z=0}^{z=l_c}\frac{zr}{\left(z^2 + r^2\right)^{\frac{3}{2}}}dz \qquad \textbf{(6.15)}$$

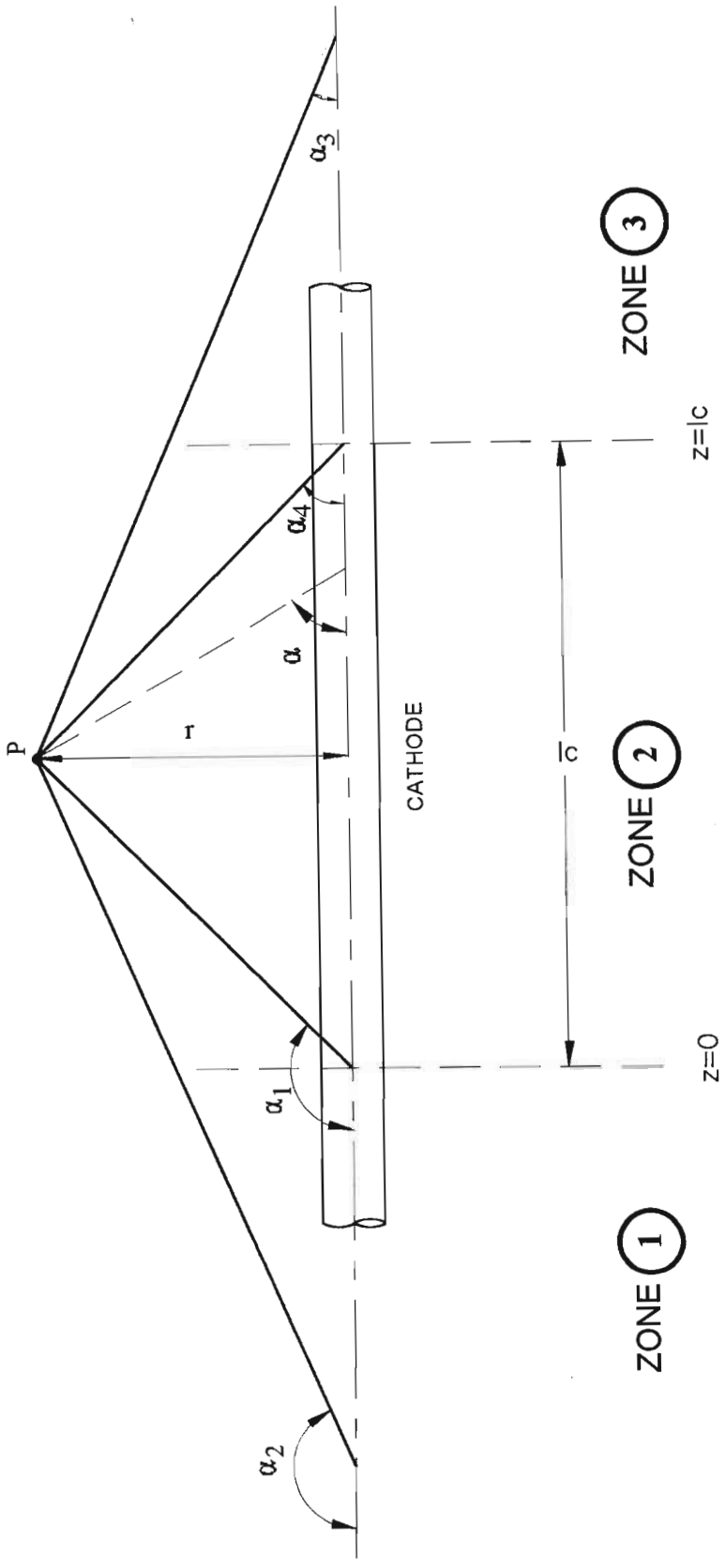

Figure 6.5 : The magnetic flux density B at some point **p**, distance r from the cathode axis, is determined as a function of the sum of the field contributions due to the three defined *zones* .

Equation 6.15 was solved by method of substitution:

$$B_{2b} = \frac{\mu}{4\pi}\left(\frac{I_G - I_L}{l_c}\right) \times \left(\sin\alpha_4 - \sin\alpha_1\right) \qquad \textbf{(6.16)}$$

After some manipulation and the substitution of various trigonometric identities the total magnetic field **B** was determined to be:

$$\begin{aligned}\mathbf{B} = B_\theta &= B_1 + B_{2a} + B_{2b} + B_3 \\ &= \frac{\mu}{4\pi}\left[\left(\frac{I_G + I_L}{r}\right) + \left(\frac{I_G - I_L}{r}\right)\cos\alpha_4 + \left(\frac{I_G - I_L}{l_c}\right)\left(\sin\alpha_4 - \sin\alpha_1\right)\right]\end{aligned} \qquad \textbf{(6.17)}$$

where again, α_1 and α_4 are as per figure 6.5.

Note, the Biot-Savart law determined the magnetic field to be in the azimuthal θ direction. Hence, for the specific purposes of this problem $\mathbf{B} = B_\theta$.

6.3.2 The Sheath Potential

Ottinger *et al* and Commisso *et al* determined the electric potential across the sheath according to the work of Child and Langmuir. Child and Langmuir determined the cathode-fall potential for the case where all charge entering the cathode-fall travelled across and consequently exited the fall region. Hence, the density of the electric charge contained in the sheath at any given moment was determined from the sheath current density and charge velocity. Using Poisson's equation the sheath potential was determined as a function of the sheath current, where the electric potential measured at any point in the sheath is equivalent to the kinetic energy of the charge crossing the sheath as a function of the charge's mass and velocity. In this manner Child and Langmuir derived their well known *three-halves law* for the planar geometry. However, since the POS is cylindrical it was necessary to derive the equivalent of the Child-Langmuir law for the cylindrical case.

By Gauss's law (from which Poisson's equation was derived):

$$\oiint \varepsilon \mathbf{E}.d\mathbf{A} = Q \qquad \textbf{(6.18)}$$

where $\mathbf{E}$ is the cathode electric field passing through some closed imaginary surface $\mathbf{A}$ which surrounds the cathode, and ε is the permittivity of the vacuum. $\mathbf{E}$ is assumed uniform and normal to the cathode surface. Hence $\mathbf{E}=E_r$. The surface $\mathbf{A}$ is typically a concentric cylinder around the cathode. Charge Q resides inside the cylinder. Since charge Q is due to the electron current I_e traversing the sheath then:

$$Q = \int_{r_c}^{r_c+D} \frac{I_e}{v_e} dr \qquad \textbf{(6.19)}$$

where v_e is the velocity of the electron flux as a function of radial distance r from the cathode. Electrons were assumed to leave the cathode surface with zero initial velocity and be accelerated across the sheath by the sheath electric field E_r. The kinetic energy acquired by an electron as it crosses the sheath must equate to the potential energy of the field in which it is accelerated.

Hence:

$$V_r e = \frac{1}{2} m_e v_e^{\,2} \tag{6.20}$$

where V_r is the electric potential measured at some distance r from the axis of the cathode, and e and m_e are the charge and rest mass of an electron respectively. Equation 6.20 was rearranged and solved for v_e according to:

$$v_e = \sqrt{\frac{2eV_y}{m_e}} \tag{6.21}$$

From equations 6.18, 6.19, and 6.21:

$$2\pi l_c \varepsilon E_r r = I_e \int_{r_c}^{r_c+D} \sqrt{\frac{m_e}{2eV_r}}\, dr \tag{6.22}$$

Equation 6.22 was then differentiated with respect to r :

$$r\frac{dE_r}{dr} + E_r = \frac{I_e}{2\pi l_c \varepsilon}\sqrt{\frac{m_e}{2eV_r}} \tag{6.23}$$

Hence:

$$\frac{dE_r}{dr} = \frac{I_e}{2\pi r l_c \varepsilon}\sqrt{\frac{m_e}{2eV_r}} - \frac{E_r}{r} \tag{6.24}$$

and by definition:

$$\frac{dV_r}{dr} = E_r \tag{6.25}$$

Spangenberg [**27**] showed that when r is large a closed form solution to the sheath potential as a function of the sheath current similar to that of Child and Langmuir may be derived. For the typical geometry with which this experiment was concerned this was unfortunately not applicable. Hence the differential equations 6.24 and 6.25 were solved numerically in order to determine the sheath potential V_r and the electric field E_r at a distance D from the cathode surface.

6.3.3 The Modified Electron Trajectory

The average path followed by an electron through the sheath to the ion flux was calculated as a function of the sheath electric field **E** and cathode magnetic field **B** in order to determine the approximate length l_p of the sheath-ion contact area A_s. An electron crossing the sheath was assumed to have velocity:

$$\mathbf{v} = (v_r, v_\theta, v_z) \tag{6.26}$$

due to force **F**, where in vacuum:

$$\mathbf{F} = q(\mathbf{E} + (\mathbf{v} \times \mathbf{B})) \tag{6.27}$$

where q is the charge of the electron. Since **E** and **B** are crossed fields in the r and θ directions respectively:

$$\mathbf{E} = (E_r(r),0,0) = E_r \tag{6.28a}$$

and

$$\mathbf{B} = (0, B_\theta(r,z),0,0) = B_\theta \tag{6.28b}$$

where the cathode lies on the z-axis. B_θ and E_r were determined from the solution to equations 6.17 and 6.25 respectively. Since force is equivalent to the time rate of change in momentum, then:

$$\mathbf{F} = m^* \frac{d\mathbf{v}}{dt} + \mathbf{v}\frac{dm^*}{dt} \tag{6.29}$$

where the relativistic mass m^* of an electron is determined from Einstein's theory of relativity using the standard Lorentz transform:

$$m^* = \frac{m_e}{\sqrt{1 - \frac{|\mathbf{v}|^2}{c^2}}} \tag{6.30}$$

m_e is the rest mass of an electron, and c the speed of light.

Equations 6.26 through 6.30 were combined and rearranged to solve for the vector velocity **v** of an electron passing through the sheath as a function of the electric field component E_y, the magnetic field component B_θ:

$$\frac{dv_r}{dt} = \frac{e}{m_e} \times \left(\frac{\left(\frac{E_r - v_z B_\theta}{v_r v_z} \right) - \left(\frac{v_r B_\theta}{c^2 - v_r^2} \right)}{\left(\frac{c^2 - v_z^2}{v_r v_z} \right) - \left(\frac{v_r v_z}{c^2 - v_r^2} \right)} \right) \times \frac{\left(c^2 - v_r^2 - v_z^2 \right)^{\frac{3}{2}}}{c} \qquad \textbf{6.31a)}$$

and

$$\frac{dv_z}{dt} = \frac{e}{m_e} \times \left(\frac{\left(\frac{v_r B_\theta}{v_r v_z} \right) - \left(\frac{E_r - v_z B_\theta}{c^2 - v_z^2} \right)}{\left(\frac{c^2 - v_r^2}{v_r v_z} \right) - \left(\frac{v_r v_z}{c^2 - v_z^2} \right)} \right) \times \frac{\left(c^2 - v_r^2 - v_z^2 \right)^{\frac{3}{2}}}{c} \qquad \textbf{(6.31b)}$$

By definition:

$$\frac{dr}{dt} = v_r \qquad \textbf{(6.32a)}$$

and

$$\frac{dz}{dt} = v_z \qquad \textbf{(6.32b)}$$

Note, both magnetic field B_θ and electric field E_r are position dependant. Hence, as an electron travels through the sheath at velocity **v** it experiences both B_θ and E_r changing with time. Hence, considering the description of B_θ and E_r an analytical solution to equations 6.31a, 6.31b, 6.32a, and 6.32b was not attempted. A numerical solution was however performed.

Figure 6.6 shows the modelled trajectory of an electron traversing the sheath due to the cathode magnetic field B_θ (perpendicular and pointing into the page) and the sheath electric field E_r. The graph was generated as a result of the numeric solution to equations 6.31a through 6.32b. Each plot corresponds to a different electric field spread due to the sheath potential V_r. Magnetic field B_θ was determined according to equation 6.17 for I_G=30kA and I_L=10kA, where these values were chosen arbitrarily.

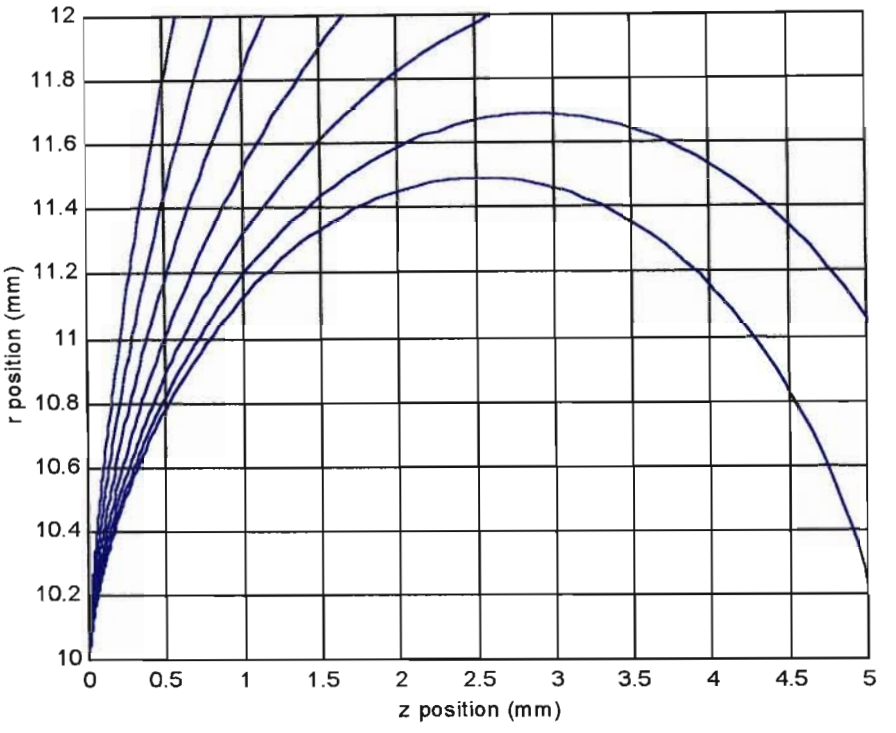

Figure 6.6 : Calculated electron trajectories through crossed $\mathbf{E}=E_r$ and $\mathbf{B}=B_\theta$ fields over surface of a POS cathode. Cathode radius r_c=10mm, cathode length l_c=5mm, sheath thickness D=2mm.

Clearly, two of the seven electrons identified in figure 6.6 do not reach the opposite surface of the sheath. Any and all electrons following a trajectory which does not contact the opposite surface of the sheath are considered magnetically insulated from the ion flux. The vacuum discharge is interrupted when electrons leaving the cathode can no longer reach the ion flux.

6.3.4 The Modified Space-Charge Relation

As electrons are caused to drift down the cathode the length l_p of the contact area between the outgoing electron flux and the incoming ion flux will reduce. The sheath thickness D will therefore increase to compensate for the lost length in an attempt to accommodate the electron flux. The sheath thickness D was written similarly to equation 6.7 according to:

$$D = \frac{A_s}{2\pi l_p} - r_c \tag{6.33}$$

where, from equation 6.6:

$$A_s = \frac{I_e}{n_i v_d Ze}\sqrt{\frac{m_e Z}{m_i}} \tag{6.34}$$

Hence:

$$D = \frac{I_e}{2\pi l_p n_i v_d Ze}\sqrt{\frac{m_e Z}{m_i}} - r_c \tag{6.35}$$

6.4 The POS Circuit

The generator, POS, and load circuit are shown in figure 6.7. Capacitor C_O is the primary energy storage element in the circuit. Inductor L_O and resistor R_O are the inductance and resistance of the feed between capacitor C_O and the POS. A mid-plane field-distortion spark-gap, denoted SG, was employed as the switch element. An ~18kV trigger signal was applied to the mid-plane of the spark-gap as a result of a ~300V signal applied to the primary of pulse transformer $TX\text{-}1$. Inductor L_L and resistor R_L are the inductance and resistance of the load respectively. Due to the anticipated rate of rise of the load current the load impedance was expected to be dominated by the load inductance.

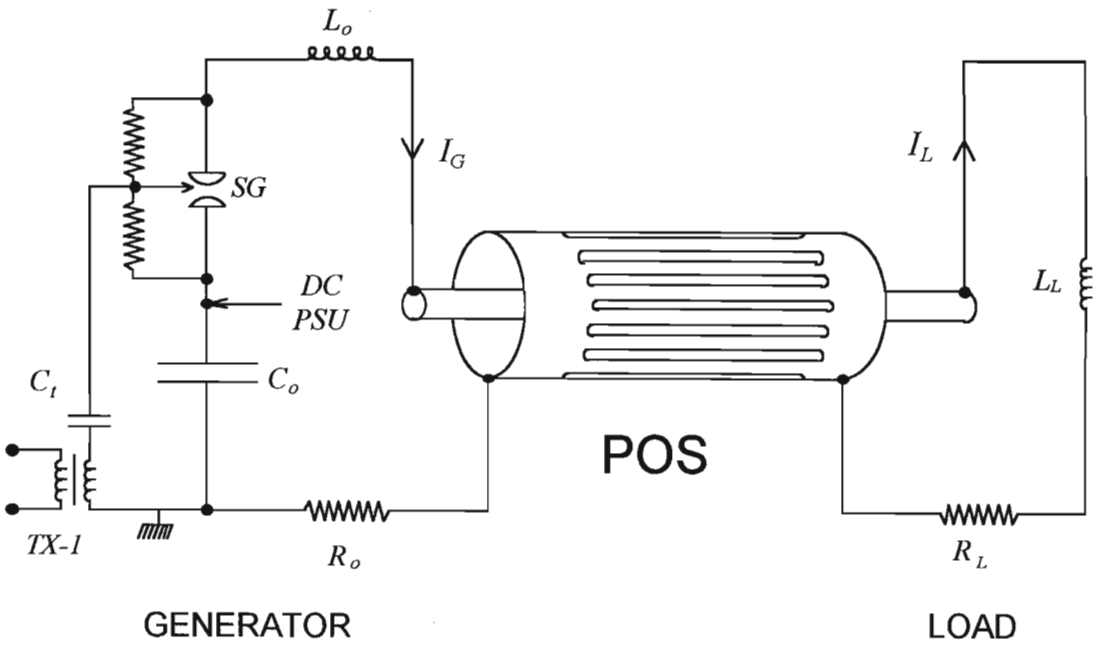

Figure 6.7 : The generator, POS, and load shown in schematic form.

6.5 A POS Numerical Model

A mathematical model of the POS was constructed from the macroscopic circuit equations and the sheath equations derived in sections 6.3.1 to 6.3.4. Kirchhoff's laws were invoked to determine the circuit equations describing the generator current and load current, as per figure 6.7. For the generator circuit:

$$V_C = L_o \frac{dI_G}{dt} + R_o I_G + V_r \tag{6.36}$$

where I_G is the time dependant generator current, V_C is the time dependent voltage across discharge capacitor C_O, V_r is the sheath potential, and L_O and R_O are the inductance and resistance of the generator circuit respectively. The time dependant voltage V_C across capacitor C_O was determined from Coulombs law according to:

$$\frac{dV_C}{dt} = -\frac{I_G}{C_o} \tag{6.37}$$

where the negative sign was due to current I_G defined flowing *out* of capacitor C_O, as opposed to *into* capacitor C_O. For the load circuit:

$$V_r = R_L I_L + L_L \frac{dI_L}{dt} \tag{6.38}$$

where I_L is the load current, and L_L and R_L are the inductance and resistance of the load circuit respectively. Rearranging equation 6.36:

$$\frac{dI_G}{dt} = \frac{1}{L_o}\left(V_C - R_o I_G - V_r\right) \tag{6.39}$$

Similarly, rearranging equation 6.38:

$$\frac{dI_L}{dt} = \frac{1}{L_L}\left(V_r - R_L I_L\right) \tag{6.40}$$

Equations 6.37, 6.39 and 6.40 are the three ordinary differential equations that were solved simultaneously in order to determine the circuit behaviour. The sheath potential V_r was determined from the solution to equations 6.24 and 6.25, where the sheath thickness D was determined from equation 6.35, and the length of the sheath-ion interface l_p from the numeric solution to equations 6.31 and 6.32, where:

$$l_p = l_c - z_D \tag{6.41}$$

and z_D is the z-position of an electron as it crosses the sheath-ion interface, determined from the solution to equation 6.32b when:

$$r = D + r_c \tag{6.42}$$

Finally, by Kirchhoff's current law:

$$\begin{aligned} I_e &= I_S - I_i \\ &= I_G - I_L - I_i \end{aligned} \tag{6.43}$$

where I_i is the ion current determined by equation 6.2.

The operation of the POS was determined from the simultaneous solution of no less than nine differential equations. Once again the variable step size Runga-Kutte-Fehlberg technique was employed to solve these equations. However, before a numeric model could be implemented it was necessary to determine the initial values of the dependent variables. At time $t=0$:

$$I_{G(0)} = I_{L(0)} = I_{S(0)} = 0 \tag{6.44}$$

$$v_{e(0)} = 0 \tag{6.45}$$

and

$$l_{p(0)} = l_c \tag{6.46}$$

Hence, from equation 6.37:

$$\frac{dV_{C(0)}}{dt} = 0 \qquad \textbf{(6.47)}$$

where $V_{C(0)}$ is the voltage to which capacitor C_o was initially charged.

$$I_{e(0)} = 0 \qquad \textbf{(6.48)}$$

Hence, from equation 6.35:

$$D_{(0)} = 0 \qquad \textbf{(6.49)}$$

and from equation 6.24:

$$V_{r(0)} = 0 \qquad \textbf{(6.48)}$$

From equations 6.39 and 6.40:

$$\frac{dI_{G(0)}}{dt} = \frac{V_{C(0)}}{L_o} \qquad \textbf{(6.49)}$$

and

$$\frac{dI_{L(0)}}{dt} = 0 \qquad \textbf{(6.50)}$$

The model described above was programmed in the MATLAB language using MATLAB-5 for windows. The complete MATLAB program code for the POS model is contained in Appendix E.

The assembled POS MATLAB model was used to determine the generator circuit, POS, and load behaviour as a function of the following parameters:

Generator components:

$$V_{C(0)} = 35\,\text{kv}$$
$$C_o = 2.8\,\mu\text{F}$$
$$R_o = 10\,\text{m}\Omega$$
$$L_o = 150\,\text{nH}$$

POS dimensions:

$$r_c = 10\,\text{mm}$$
$$r_a = 40\,\text{mm}$$
$$l_c = 60\,\text{mm}$$

Carbon plasma:

$$Z = 2$$
$$n_i = 5\times10^{18}\ \text{m}^{-3}$$
$$v_i = 6\times10^{4}\ \text{m/s}$$
$$m_i = 2\times10^{-26}\ \text{kg}$$
$$m_e = 9.11\times10^{-31}\ \text{kg}$$
$$e = 1.6\times10^{-19}\ \text{C}$$

and load components:

$$L_L = 79\,\text{nH}$$
$$R_L = 0.01\,\Omega$$

Figure 6.8. shows the predicted generator current I_G (blue), predicted switch current I_S (red) and the predicted load current I_L (green) as a function of time.

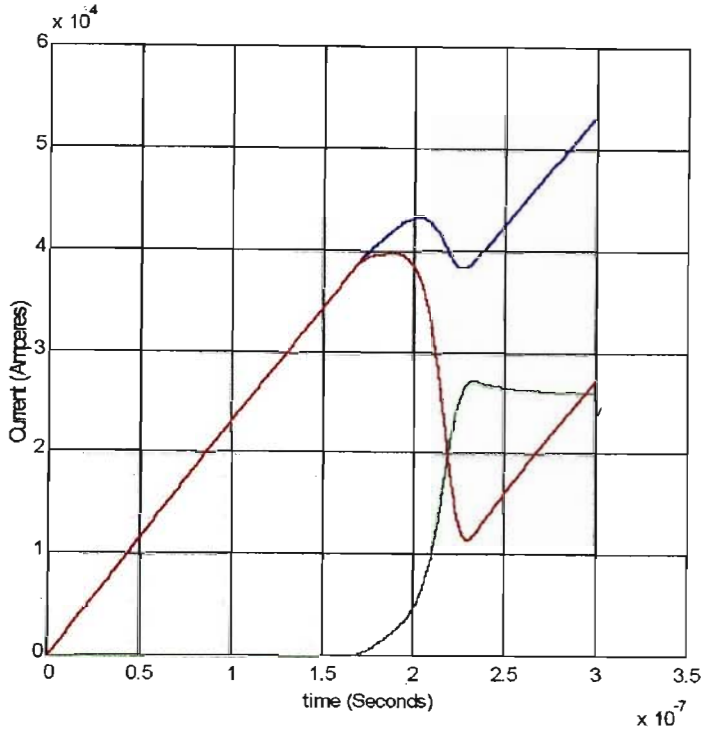

Figure 6.8 : The modelled generator current (in blue), switch current (in red) and load current (in green).

Note: The generator current is sinusoidal, but with period much greater than that shown in figure 6.8. Hence the linear appearance of the rising edge of the generator current. The entire switching event was predicted to occur well in advance of the peak generator current. The model predicted a peak switch current of ~40kA prior to the erosion of the ion flux. The model indicated that for the POS with which we were concerned the switch current would never fully terminate due to the incomplete magnetic insulation of the cathode. Approximately 225ns after the discharge had commenced the respective switch and generator currents were predicted to evolve in *parallel* manner, separated by a constant measure of current. This was as to be expected since once the switch current is re-established any current that continues to flow through the load is trapped in the load circuit until such time as it dissipates into the load resistance or the discharge.

Figures 6.9(a) through 6.9(d) show the modelled magnetic flux density in the θ direction around the cathode at various times as a function of distance along the axis of the cathode and distance from the cathode into the plasma. The darkest red indicates the maximum flux density (~1 Tesla), while the deepest blue indicates the minimum flux density (~0.01 Tesla). As the magnetic field grows in intensity the electrons within the sheath are displaced further down the cathode allowing the magnetic field to penetrate deeper into the plasma as a result of the localised growth in the cathode current. The magnetic field clearly penetrates deeper and deeper into the plasma with increasing time.

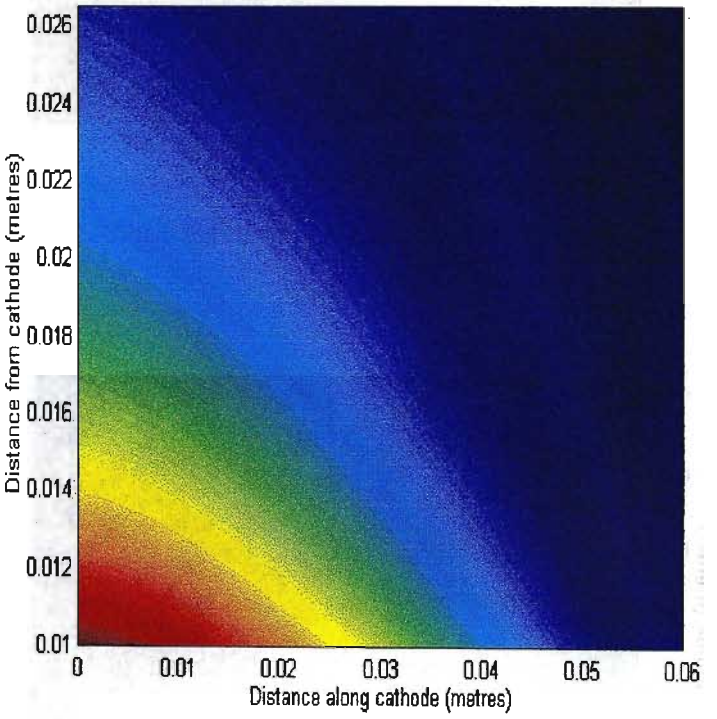

Figure 6.9(a) : Magnetic flux density around POS cathode at 200nS.

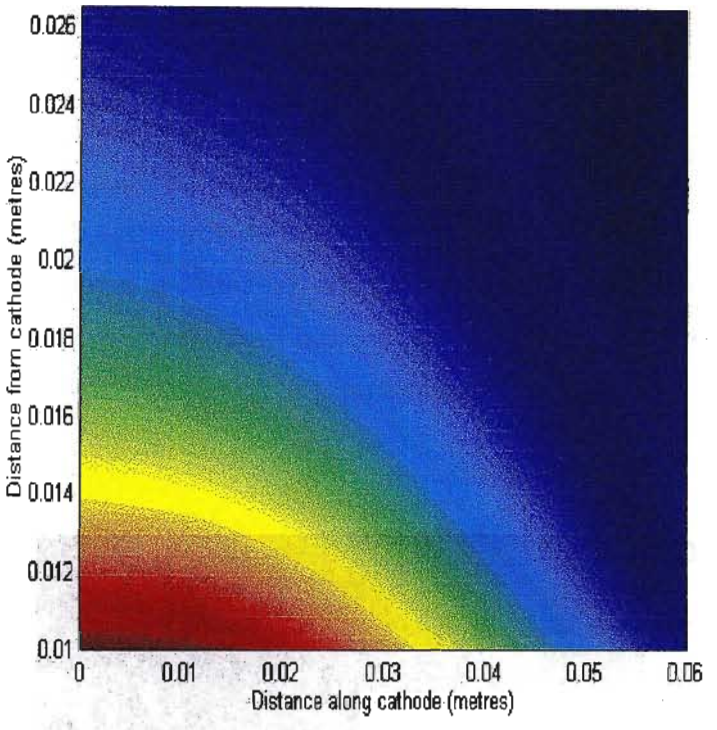

Figure 6.9(b) : Magnetic flux density around POS cathode at 210nS.

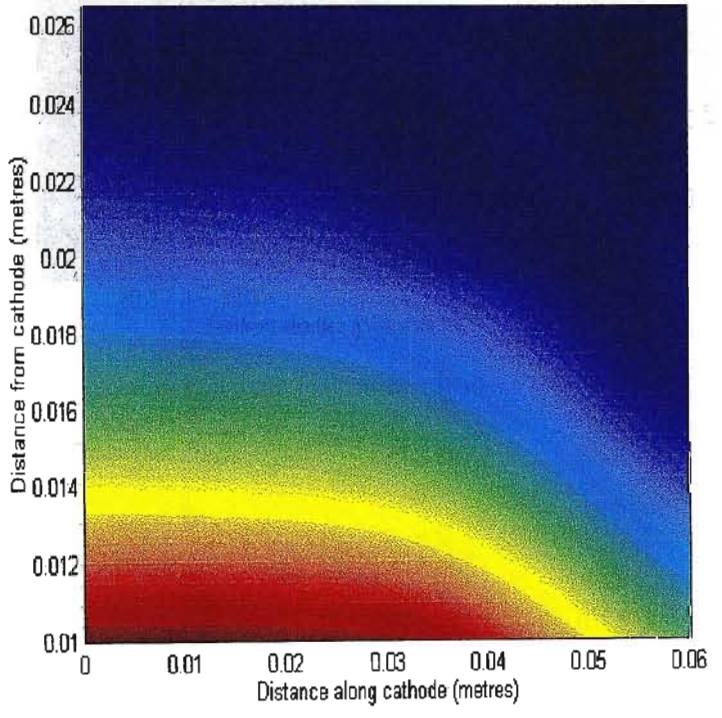

Figure 6.9(c) : Magnetic flux density around POS cathode at 220nS.

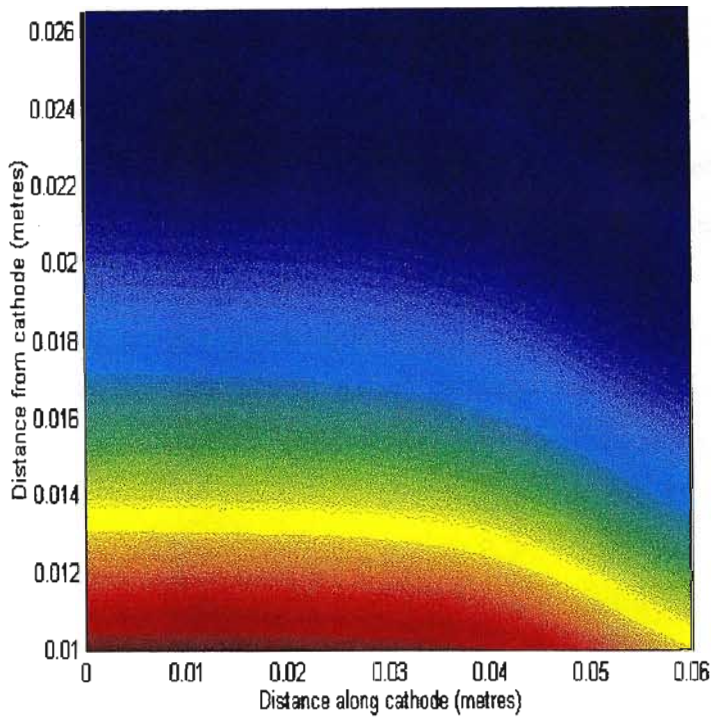

Figure 6.9(d) : Magnetic flux density around POS cathode at 230nS.

Note, figures 6.9(a) through 6.9(d) are not intended to provide a quantitative prediction of the magnetic flux density, but rather to illustrate the gradual penetration of the magnetic field into the plasma with time. Arad *et al* [**28**] have published similar data describing the magnetic field penetration into a parallel plate POS. While the geometry of the parallel plate device is significantly different to the coaxial POS described in this text, the movement of the plasma under the influence of the driving current and its associated magnetic field is undoubtedly similar.

6.6 Results

6.6.1 POS With FOS

In order to achieve as large as possible voltage across the POS load it was required that the POS storage inductor L_o be as large as tolerable. However, the model indicated that an excessively high generator inductance would slow the circuit performance beyond the lifetime of the conduction plasma (~2μS). It was therefore decided that a pre-POS pulse sharpening circuit should be implemented. The popular method of a fuse opening switch (FOS) was chosen. The POS circuit initially comprised a bank of four 2.8μF 50kV Maxwell capacitors connected in parallel, a 0.89μH storage inductor, a copper FOS, a 250μm Mylar over-volt dielectric closing switch, the POS, and a 3.8Ω liquid resistor. Figure 6.10 shows the implemented circuit:

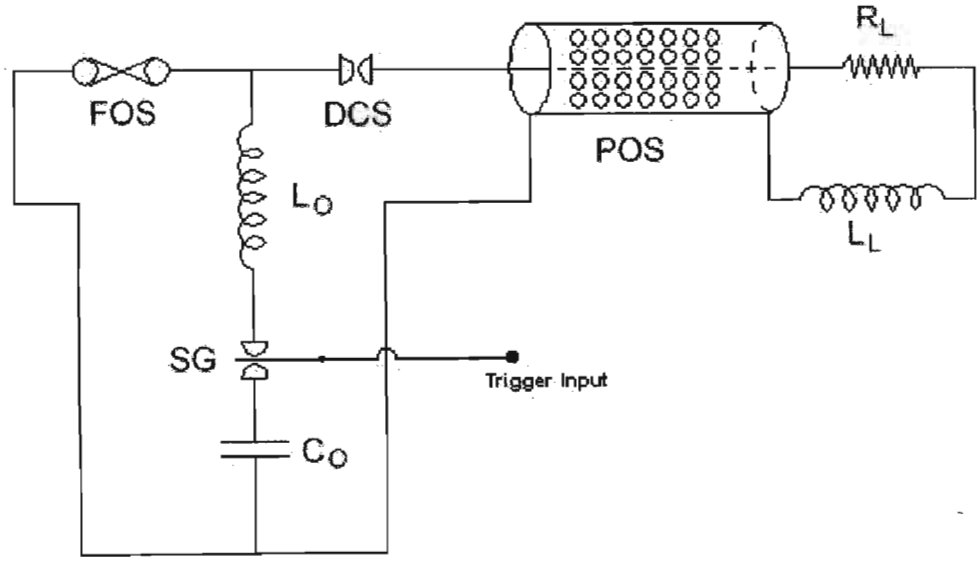

Figure 6.10 : The implemented pre-POS, POS and load circuit.

Figure 6.11 shows the assembled POS experiment. The lid of storage inductor L_o is visible beneath the POS. A glass-blower performed the manufacture of the Pyrex vacuum vessel and the interface between the vessel and vacuum station. A turbo-molecular vacuum pump, backed by a rotary-vane pump, was attached to the experiment via a flexible NW40 coupling. Typical operating pressure was 2-5 $\times$ 10^{-6} torr. The FOS was housed in the aluminium pipe to the left of the *'neck'*, and the POS to the right. The over-volt dielectric opening switch was mounted at the mouth

of the POS (not visible). The storage inductor, the 'neck', and the FOS housing were filled with SF_6 gas prior to each discharge event. The generator was triggered using a mid-plane field distortion spark-gap.

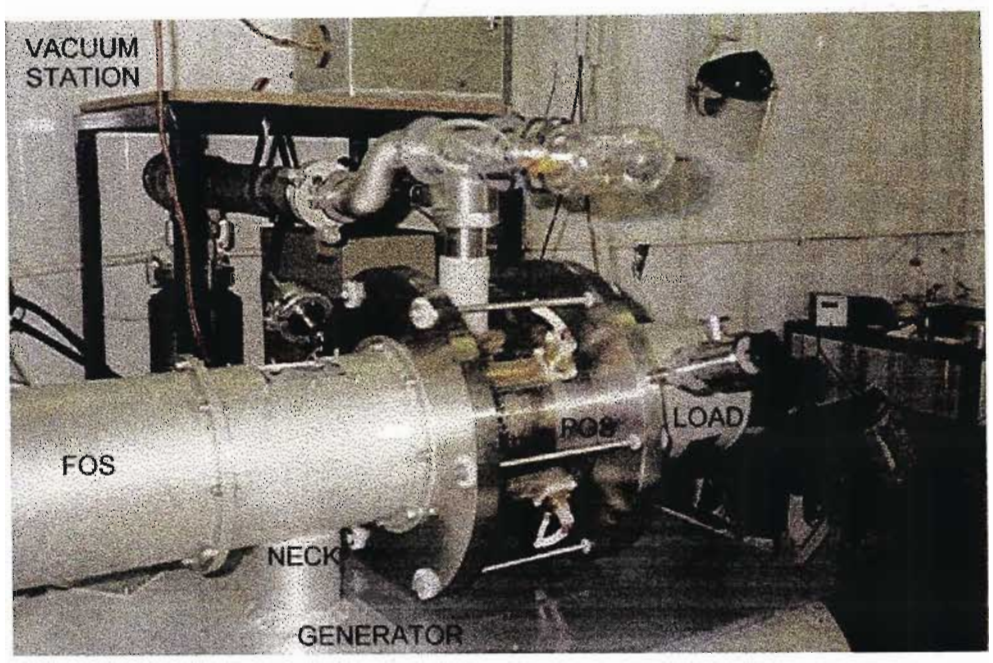

Figure 6.11 : The upper section of the initial pre-POS, POS and load circuit (energy storage capacitors not visible).

After numerous trials with other dimension fuses, a 0.7mm × 210mm copper wire was chosen. The fuse was observed to reliably burst in ~1μs at a current of 90kA. The measured FOS current is shown in figure 6.12. The fuse was observed to be completely open circuit at approximately 5.5μs after $t=0$.

In accordance with Faradays law, as the FOS current terminates an EMF develops across inductor L_O sufficient to breakdown the over-volt closing switch, pushing the generator current, equivalent to that stored in the inductor, into the POS. Figure 6.13 shows the typically measured POS input or *generator* current.

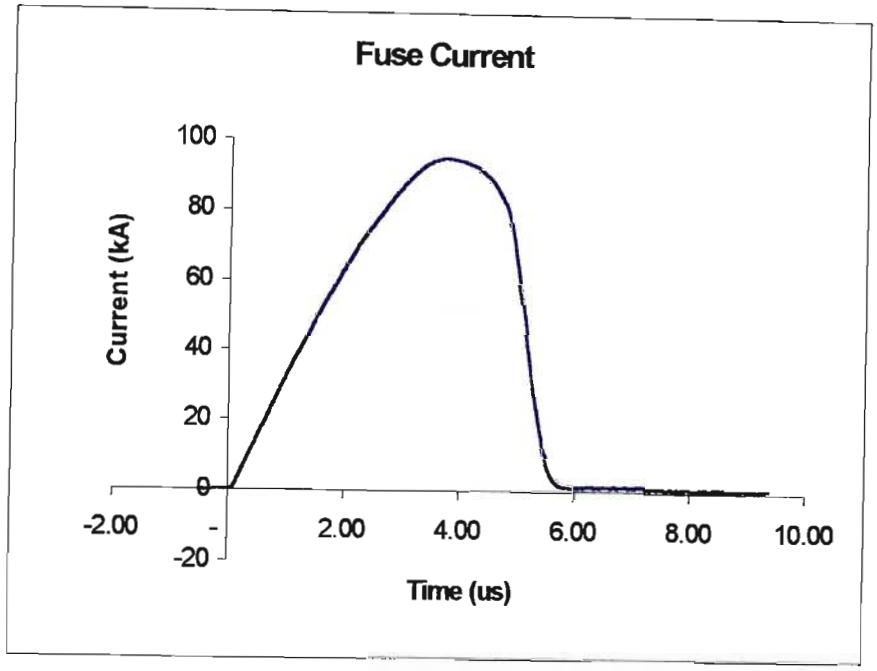

Figure 6.12 : Typical measurement of the generator current through a 0.7mm × 210mm copper fuse.

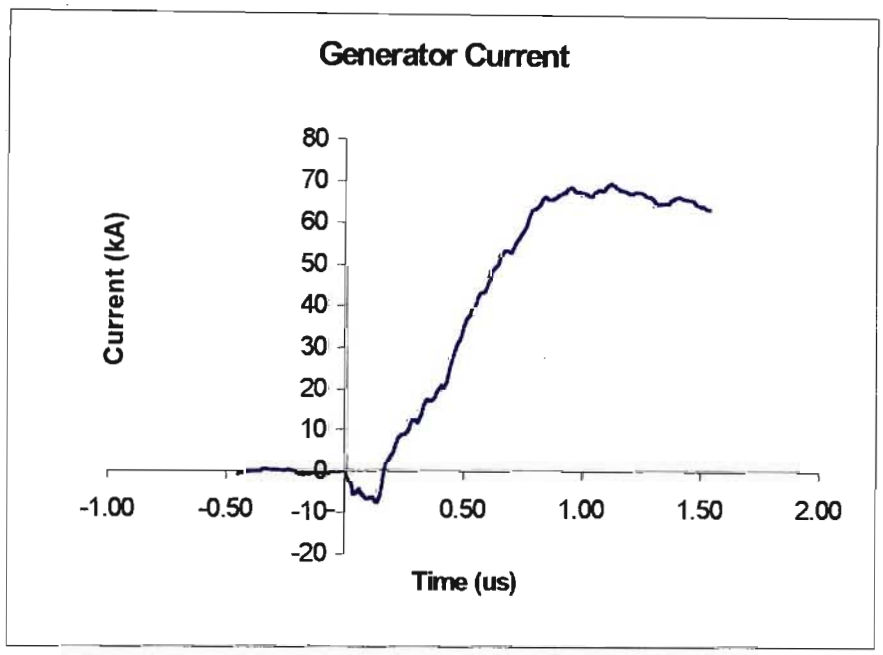

Figure 6.13 : Typical measurement of the POS input current.

The apparent initial negative deviation in the measured POS input current is erroneous, and is a function of the proximity of the current probe to the over-volt dielectric opening switch at the input to the POS.

The capacitor bank was charged and discharged into the FOS-POS apparatus approximately twenty times. However, no POS output was recorded with the experiment in the above configuration. Subsequent to the analysis of the sheath electron trajectory it was realised that the movement of the sheath electrons was obstructed by a plastic insulator positioned at the load end of the POS. It was decided, therefore, that the POS vacuum vessel should be extended and the insulator repositioned in order to prevent the further obstruction of the sheath electrons. Given that extensive modifications were to be performed on the POS it was decided to further upgrade the POS cathode such that the erosion phase would commence at ~50kA. This required the installation of a 20mm diameter cathode and the consequent remanufacture of most of the interior POS components, including the anode. The new cathode was manufactured from brass. The new anode was, however, once again manufactured from stainless steel. Figure 6.14 shows a cross-section of the new POS with its 20mm diameter cathode, plasma containment chamber and load resistor.

In addition, a non-conducting PVC tube (of inner diameter 35mm) was positioned around the cathode (of outer diameter 20mm) obscuring a portion of the cathode from the incident ion flux. The cathode length l_c was therefore the length of that area exposed to the ion flux. The cathode length did not include that portion of the cathode obscured by the PVC tube. Evidence of carbon ions striking the inside surface of the tube was found when the *interior* of the PVC tube was inspected subsequent to a number of discharge events. Carbon ions were observed to deposit themselves down the inside of the PVC tube during collisions with the inner wall of the tube. This was as expected since the injected ion flux is accelerated down the cathode in similar fashion to the electron flux, only much later in the POS discharge histology since the ions are significantly heavier than electrons.

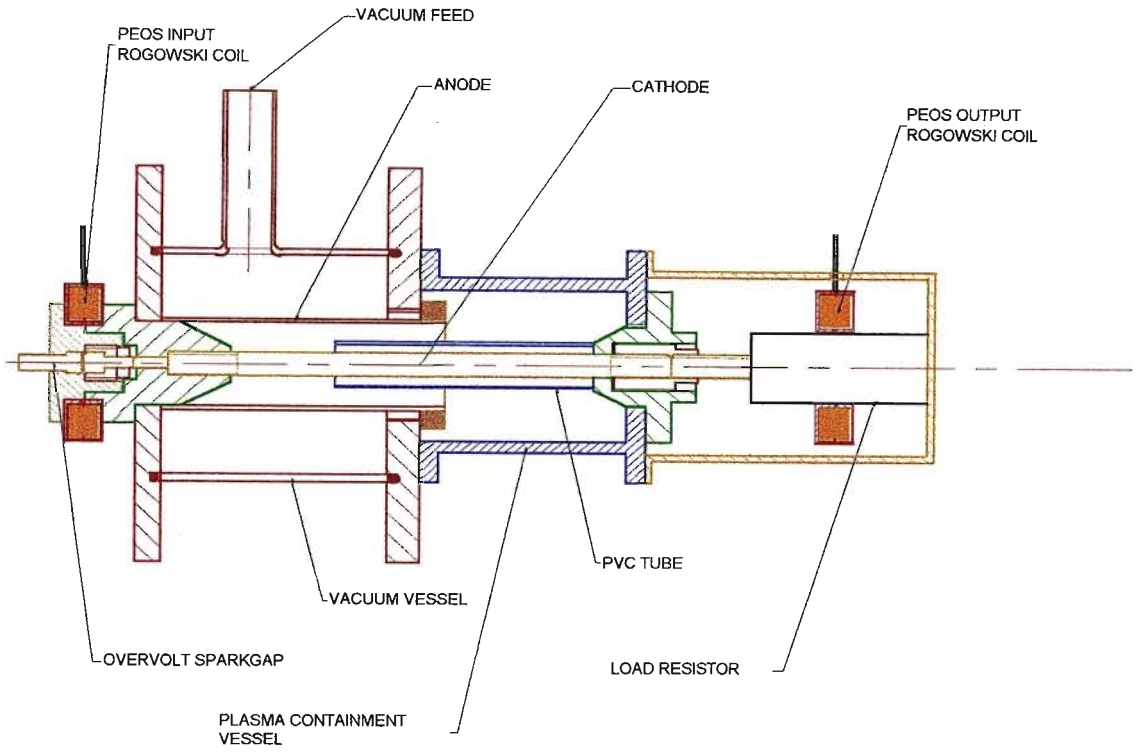

Figure 6.14 : A diagram of the POS, plasma containment chamber and load resistor.

Figure 6.15 shows the discoloration of the inside one such PVC tube that was cut open to expose its interior. The dark black discoloration occurs closet to the load end of the POS indicating that the carbon plasma was driven down the cathode all the way to the plastic insulator which separates the anode from the cathode while maintaining the vacuum. This discoloration was clearly caused by the carbon from the flash-boards since it could be easily wiped away with the tip of ones finger and had the texture and appearance of powdered carbon such as that painted onto the face of the flash-boards.

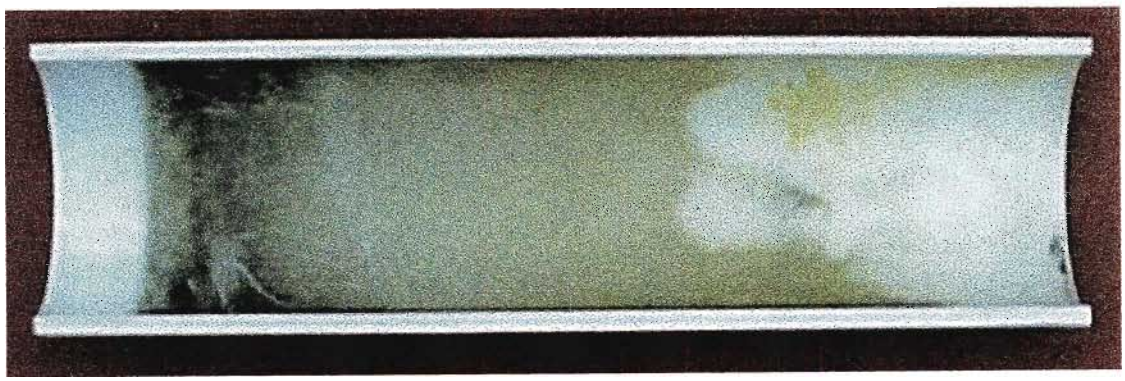

Figure 6.15 : The interior of the PVC insulating pipe placed around the cathode. The left side was closest to the load.

Subsequent to this modification meaningful results were extracted from the POS. Figure 6.16 shows the first significant simultaneous measurement of the POS generator current, switch current, and load current recorded using Rogowski coils placed around the modified experiment described above.

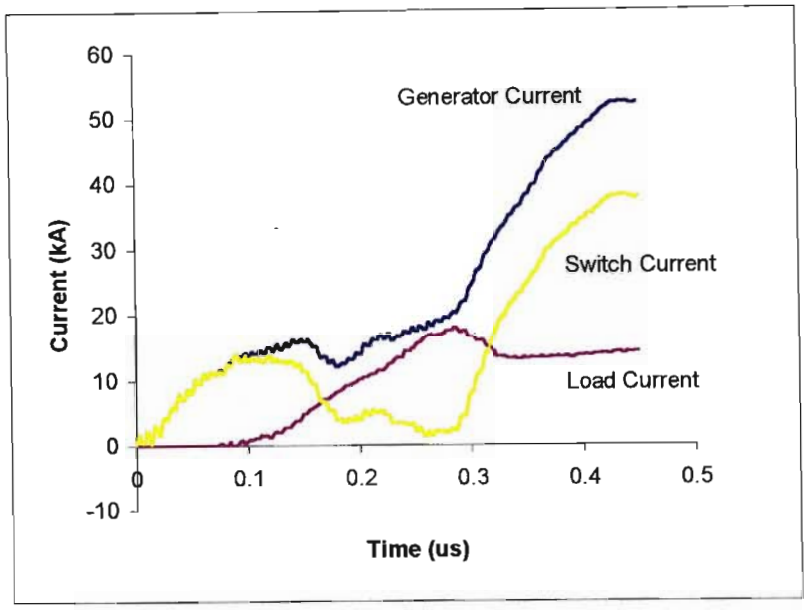

Figure 6.16 : The first significant POS data which shows a clear tendency in the switch current to decrease in order to drive current into the load.

Figure 6.16 indicates that the rate of rise of the load current is slower that the rate of rise of the generator current. This is contrary to the desired POS operation. However, of significance here is that the switch current (shown in yellow) is observed to drop significantly at ~100ns after $t=0$, indicating that some form of erosion of the plasma, as well as magnetic field interaction, did indeed occur.

A critical aspect of POS operation is the synchronisation of the generator output to the injected plasma. Since the useful lifetime of the plasma is known to be limited to around a microsecond or two, it is essential that the generator current be delivered to the POS while the plasma density is at its optimum. If the generator circuit is triggered prior to the flash-board discharge circuit then no conductive medium is available to carry the switch current between the anode and the cathode. Hence, the generator has no alternative other than to discharge into the POS load. If, however, the plasma is injected too soon, then a dense plasma collects around the cathode causing the erosion of the plasma to occur over a time period significantly

longer than expected. The demonstrated performance of the POS in figure 6.16 was attributed to the poor synchronisation of these two events. The flash-board discharge circuit was observed to introduce a delay of ~1μs between the trigger signal and the discharge of the plasma. The plasma was observed to traverse the distance from the flash-boards to the cathode in an additional ~1μs. Figure 6.12 indicated a further delay of ~5μs due to the FOS. Hence, by simple arithmetic it was determined that the generator should be triggered ~3μs before the flash-board discharge circuit.

Measurements were performed at various timing intervals to determine which delay provided optimum POS performance. The delay generator was initially set to 4.5μs and then gradually decreased. Figure 6.17 indicates that at a delay of 4.5μs the generator current preceded the injection of the plasma, since the load current preceded the switch current. It was concluded, therefore, that the switch was open when the generator was triggered, and that the plasma penetrated the anode-cathode gap while the generator was discharging into the load.

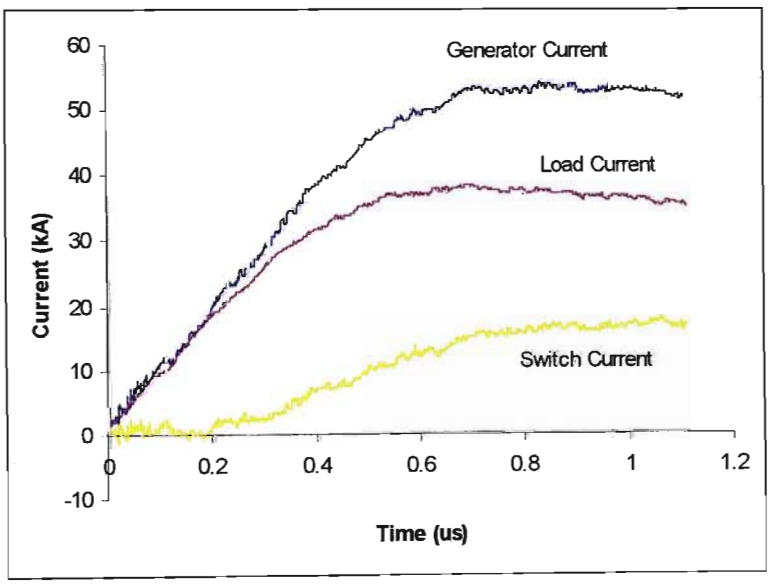

Figure 6.17 : Measured POS generator, load and switch currents with $\Delta t = 4.5\mu s$.

Figure 6.18 illustrates the converse situation where the flash-boards were triggered 2μs before the generator was triggered. Clearly the POS shows no tendency to move from the closed to open circuit state.

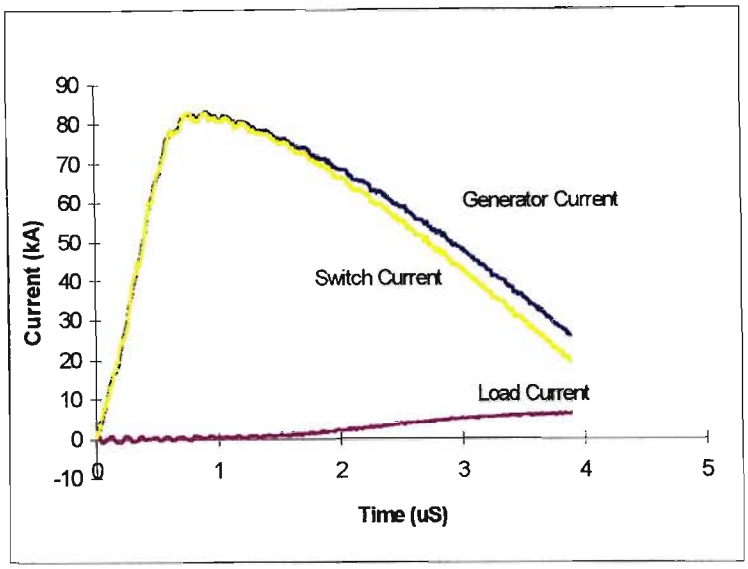

Figure 6.18 : Measured POS generator, load and switch currents with $\Delta t = -2.0\mu s$.

Figure 6.19 shows the measured generator, switch an load currents after the generator was triggered 1.5μs prior to the flash-boards. $\Delta t = 1.5\mu s$ was the delay observed to provide the optimum POS performance. Clearly the rate of rise of the load current is greater than the rate of rise of the generator current, as was expected. The switch current was observed to decrease as the cathode was magnetically insulated from the ion flux. The POS performance indicated in figure 6.19 is an improvement over that indicated in figure 6.16. However, the POS shows little ability to remain open for longer than typically 50-100ns.

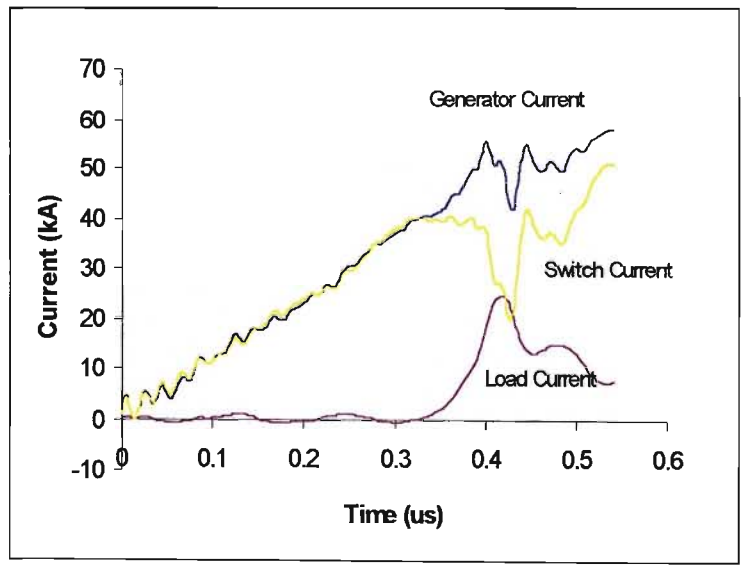

Figure 6.19 : Measured POS generator, load and switch currents with $\Delta t = 1.5\mu s$.

6.6.2 POS Without FOS

To simplify the operation of the circuit and hence speed up the rate of data collection the POS generator circuit was redesigned in order to specifically exclude the FOS and over-volt dielectric closing switch. In order to keep the circuit operation sufficiently fast in the absence of the FOS, the values of capacitor bank C_O and storage inductor L_O had to be significantly reduced. The POS circuit was manufactured as per the original circuit shown in figure 6.7. Figure 6.20 shows the manufactured experiment. The four channel flash-board discharge circuit is visible to the right-rear of the assembled circuit. The single 2.8μF energy storage capacitor C_O was separated from the POS by the mid-plane field-distortion spark-gap. The spark-gap was mounted inside the ~150nH pre-POS energy storage inductor L_O. The load R_L and L_L comprised an 0.15Ω, ~100nH graphite cylinder mounted in an aluminium housing on top of the POS.

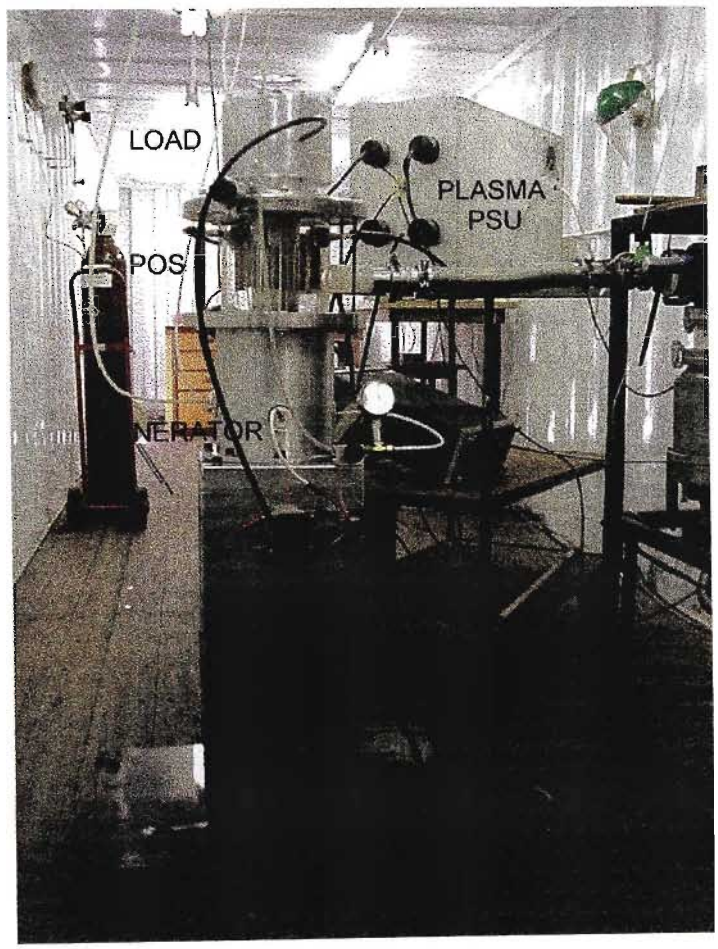

Figure 6.20 : The second generation assembled POS experiment.

Figures 6.21 and 6.22 show the typically measured generator, switch and load currents. Since the generator circuit no longer included a fuse-switch and an over-volt dielectric closing switch the optimum delay time Δt had to be re-evaluated. Hence, in the same manner as previously described, it was determined that the flash-boards should be triggered ~1.3μs prior to the generator.

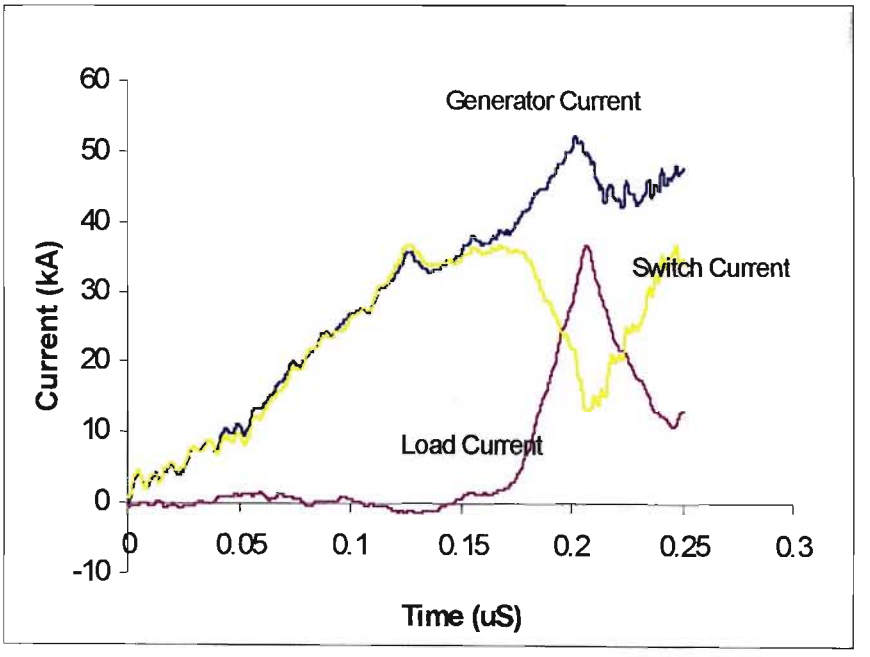

Figure 6.21 : Measured POS generator, load and switch currents with $\Delta t = 1.5\mu s$.

Figure 6.22 ($\Delta t = -1.3\mu s$) shows a similar result to figure 6.21 ($\Delta t = -1.5\mu s$). However, Figure 6.22 indicates that firing the generator slightly earlier caused the onset of the erosion phase at a slightly lower current of ~33kA compared to the ~38kA indicated in figure 6.21. Furthermore, a marginally higher degree of insulation is indicated in figure 6.22 compared to that indicated in figure 6.21.

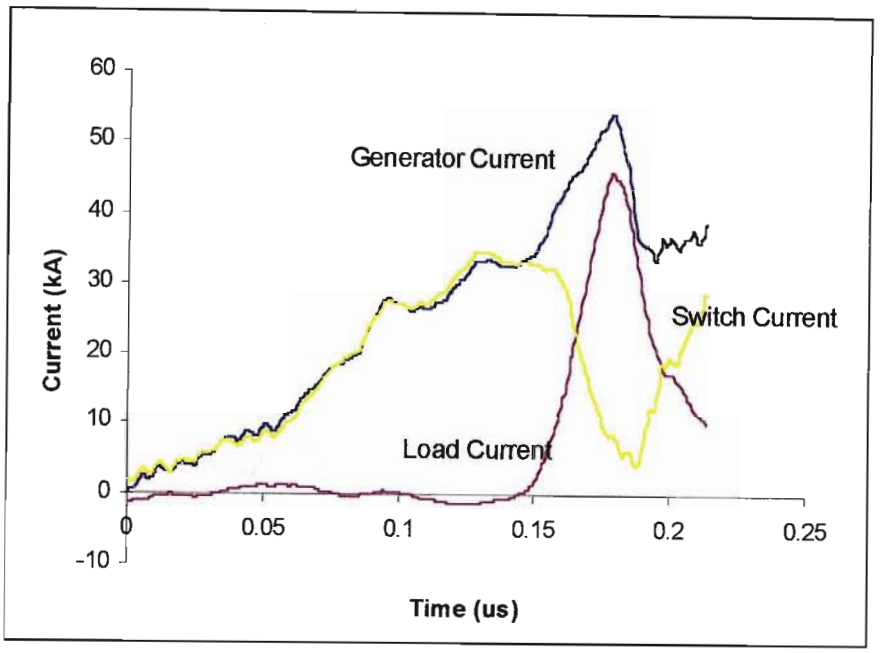

Figure 6.22 : Measured POS generator, load and switch currents with $\Delta t = -1.3\mu s$.

Both figures 6.21 and 6.22 indicate that the discharge through the POS anode-cathode space momentarily terminated, causing current to flow into the load. A peak load current of 45kA was measured, which was as predicted. Figures 6.21 and 6.22 compare well to the predicted currents of figure 6.8. The measured rise time of ~35ns was slightly faster than the predicted value of ~50ns.

Note, in terms of world-wide POS research, a rise-time of 35ns is slow. Commisso *et al* reported that ~250kA of current was delivered to a 10Ω e-beam diode load in ~10ns. In the above case a faster rate of increase in load current could not be achieved due to the limited generator current. As a general rule, the greater the cathode current the faster the ion flux is eroded and the faster electrons are caused to drift away from the ion flux. Hence, the faster the switch opens.

Figure 6.23 shows an open shutter photograph of a discharge through the first generation POS described in 6.6.1, and is identical to that observed on the second generation POS. The luminous pink appearance may be due to the response of the photographic film rather than the actual colour of the discharge. Due to soft x-ray and microwave emission from the discharge direct eye contact was avoided.

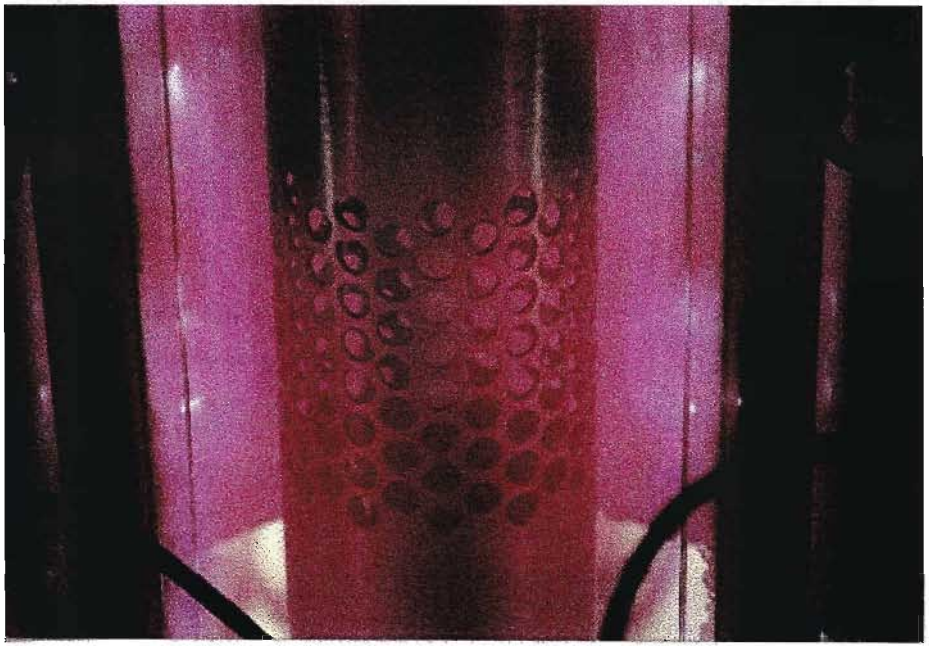

Figure 6.23 : An open-shutter photograph of a POS discharge,

6.7 Conclusions

The theory, design, manufacture and operation of a magnetically interrupted vacuum discharge was presented. The design was implemented by method of a mathematical model constructed using the MATLAB mathematical programming language. The model was based on an analysis of the circuit currents as a function of the sheath potential. The sheath potential was determined as a function of the plasma properties, the cathode magnetic field, and the sheath current.

A pulsed discharge power-supply, POS and load was constructed and tested in order to verify the theoretical model. Measurements of the generator, discharge, and load currents were performed. The measurements were compared to the predictions obtained from the model. The model was shown to provide a reasonable mathematical description of the processes believed to occur within the cathode sheath. The model accurately predicted the onset of the switch opening at ~40kA for a given set of generator, POS and load parameters. The load current rise-time and decay was shown to differ marginally from that of the model. Since it was impossible to measure the cathode magnetic field in the sheath it was impossible to verify the exact rate at which the sheath electrons were caused to drift. However, given the overall similarity between the model and the results, it was assumed that the method of the model was reasonably correct. No information on the plasma source was presented, but may be derived from the sited references.

Considering the promising results obtained and the interesting nature of the POS, it is intended that the POS will be remanufactured with a cathode of larger radius and bigger discharge power-supply in order to verify the operation of the POS at greater switch current.

Chapter 7

Pulsed Current Measurements

7.1 Introduction

In the preceding chapters numerous graphs illustrating measured current through various apparatus were presented. These measurements were performed using Rogowski (pronounced *ro-gof-ski*) coils. Rogowski coils are typically employed for the measurement of fast rate of change transient currents flowing in pulsed high power circuits. Rogowski coils are often used where conventional methods fail. Pulsed currents of a few mega-Amperes have been measured successfully with Rogowski coils.

The Rogowski coil was first demonstrated as a measurement tool in the Journal "Elektrotegnik" in 1912 by Rogowski and Steinhaus [**29**]. Since then Rogowski coils have been thoroughly investigated. Rogowski coils are just one in a family of devices designed to intercept a small portion of the magnetic flux surrounding a current carrying conductor in order to determine the current flowing in that conductor. A Rogowski coil comprises a length of conducting wire (of finite conductivity) wound onto a non-conducting, non-metallic, non-magnetic toroidal former (usually a polymer). A terminating resistance and a length of screened cable are attached to the coil. The coil is then placed around a current carrying conductor with the conductor running as close to the major axis as possible. Note, the coil is often encased in a similarly shaped, grounded, non-magnetic, conductive metallic casing (usually of aluminium or copper) to prevent lines of electric-field coupling to the coil. For example, the current carrying conductor may also be a high voltage conductor, and without a metallic screen the coil will function as a crude voltage probe! The output of a Rogowski coil is typically a time varying voltage signal which may be used directly or processed in some manner to derive a measurement of the current flowing in the conductor about which the Rogowski coil is placed.

Since there is no physical contact between the probe and the conductor the current under observation is essentially unaware that it is being measured, and hence behaves in an otherwise unperturbed manner. Of course no measurement

technique is truly unobtrusive. A Rogowski coil may, however, be designed in such a way as to minimise any effect that it may have on the conductor around which it is placed by keeping the mutual inductance that it shares with that conductor as small as possible. This is one of the primary reasons why Rogowski coils *specifically contain no magnetic core material*, and hence display an ability to measure fast rate of change currents due to their low self and mutual inductance.

The design of any Rogowski coil requires some mathematical problem solving, more so if the geometry of the current carrying conductor is complex. To design and manufacture the Rogowski coils employed in this work a knowledge of electromagnetics and the geometry of the assembly into which the coil was to be placed was required. During this work it was found that Rogowski coils are not easy devices to implement. This was not due to the complexity of the theory, but rather due to difficulties experienced in operating the coils within the harsh electromagnetic environment associated with pulsed power experiments. Typically, small volumes of low density magnetic flux were intercepted within regions of high electric field strength. It is *not* unusual, therefore, for Rogowski coils to be custom manufactured to suit difficult experiments, as was the case with the work presented in this text. Invariably the manufactured Rogowski coils have contributed to the increased size of the apparatus, and hence the increased inductance of the circuit under observation. Figure 7.1 shows two of the Rogowski coils manufactured for this research. Only the housings which surrounds the coils are visible.

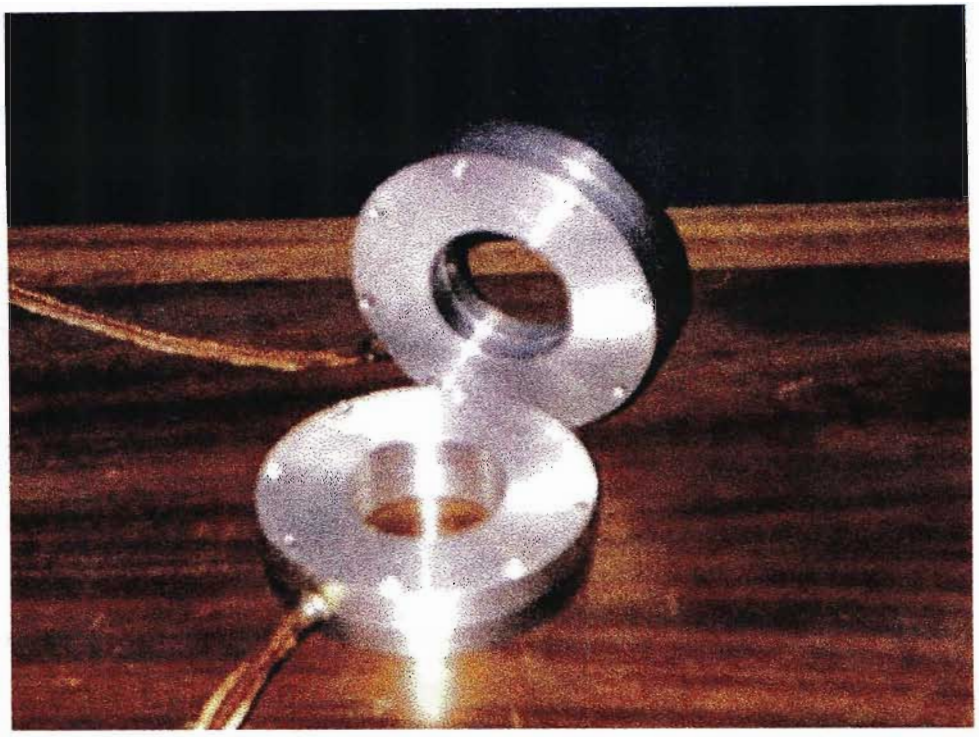

Figure 7.1 : Two of the manufactured Rogowski coils. The conductor whose current is to be measured is passed through the centre of the device.

A Rogowski coil operates on the principle that the electric potential that develops across its terminals is a function of the magnetic flux (due to the current flowing in a given conductor) coupled with the coil. Based on the work of Rogowski and Steinhaus, Krompholz *et al* [**30**], Nalty *et al* [**31**] and Stygar et al [**32**] a set of equations were constructed to describe the coil output as a function of the magnetic flux generated by a conductor about which the coil was placed. In order to do so it was necessary to calculate the magnetic field strength at a distance from the current carrying conductor equivalent to the major radius of the Rogowski coil.

7.2 The Rogowski Coil

The case of the magnetic field about an infinitely long conductor was considered initially. A current flowing through this conductor was determined to have an associated quantity of magnetic flux calculated according to the Biot Savart law [33]. The Biot Savart law states that a segment of an arbitrary shaped conductor of arbitrary length $d\mathbf{l}$ carrying the current I contributes the element of magnetic field intensity $d\mathbf{H}$ at the point **p** according to:

$$d\mathbf{H} = \frac{Id\mathbf{l} \times \mathbf{a}_r}{4\pi r^2} \quad , \tag{7.1}$$

where $\mathbf{a}_r$ is the unit vector passing through *both* the segment of current carrying conductor $d\mathbf{l}$ and the point **p** at which the magnetic field strength is determined. The scalar distance from $d\mathbf{l}$ to the point **p** is denoted r. Equation 7.1 was rearranged to suit the infinitely long straight conductor after assuming, for simplicity, that the current carrying conductor lay along the x-axis of the co-ordinate system in the x-y plane as per figure 7.2. The conductor segment $d\mathbf{l}$ was then simply written as $dx \cdot \mathbf{a}_x$, where $\mathbf{a}_x$ is the unit vector along the x-axis. The point **p** is positioned on the y-axis distance y from the x-axis.

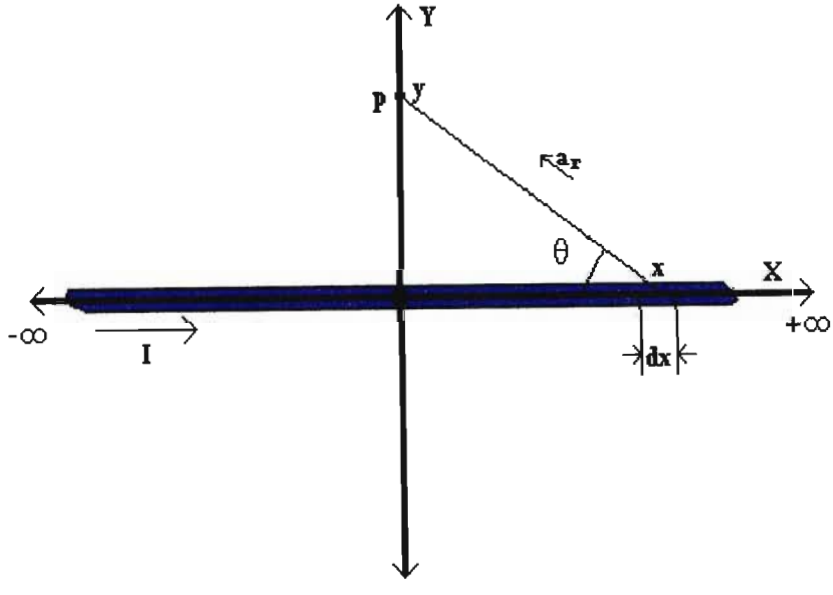

Figure 7.2 : Some point **p** positioned a distance y from an infinitely long current carrying conductor positioned on the x-axis in the x-y plane.

In accordance with figure 7.2 the distance between the segment dx and the point **p** is the root of the sum of x^2 and y^2, where x is the x co-ordinate of the segment dx parallel to the x-axis. Hence, equation 1 was rewritten as:

$$d\mathbf{H} = \frac{Idx.\mathbf{a}_x \times \mathbf{a}_r}{4\pi\left(x^2 + y^2\right)} \qquad \textbf{(7.2)}$$

The vector cross product of $\mathbf{a}_x$ and $\mathbf{a}_r$ is, from the geometry of this problem, in the direction of $\mathbf{a}_z$, the unit vector along the z-axis, perpendicular to both the x-axis and the y-axis. This vector was shown using vector calculus to be numerically equivalent to:

$$\frac{y}{\sqrt{x^2 + y^2}}.\mathbf{a}_z \qquad \textbf{(7.3)}$$

from equations 7.2 and 7.3:

$$d\mathbf{H} = \frac{I.y}{4\pi\left(x^2 + y^2\right)^{\frac{3}{2}}}dx.\mathbf{a}_z \qquad \textbf{(7.4)}$$

Since **H** is in the z-direction only the vector notation was dropped. Hence from equation 7.4:

$$dH = \frac{I.y}{4\pi\left(x^2 + y^2\right)^{\frac{3}{2}}}dx \qquad \textbf{(7.5)}$$

Equation 7.5 is one interpretation of the Biot Savart law applied to the geometry of this particular problem. In order to solve for the magnetic field strength H (determined to be in the direction of the z-axis) equation 7.5 was integrated along the entire length of the wire. That is from $x = -\infty$ to $x = +\infty$. Hence:

$$H = \frac{I}{4\pi}\int_{-\infty}^{+\infty}\left(\frac{y}{\left(x^2 + y^2\right)^{\frac{3}{2}}}\right)dx \qquad \textbf{(7.6)}$$

This integral was solved by method of substitution. Equation 7.6 was rewritten in terms of the angle θ (subtended between the vector a_r and the x-axis) by defining θ according to $\csc\theta = \frac{r}{x}$. Hence:

$$r^2 = \left(x^2 + y^2\right) = y^2 \csc^2 \theta \qquad \textbf{(7.7)}$$

Rearranging equation 7.7 yielded:

$$\begin{aligned} x &= y\sqrt{\csc^2 \theta - 1} \\ &= y.\cot\theta \end{aligned} \qquad \textbf{(7.8)}$$

The derivative of equation 7.8 was taken with respect to θ :

$$dx = -y \csc^2 \theta d\theta \qquad \textbf{(7.9)}$$

Equations 7.7, 7.8 and 7.9 were then substituted into equation 7.6. Hence:

$$H = -\frac{I}{4\pi}\int_{\pi}^{0}\left(\frac{y}{\left(y\csc\theta\right)^3}\right) y \csc^2 \theta d\theta \qquad \textbf{(7.10)}$$

which was rewritten as:

$$H = -\frac{I}{4\pi.y}\int_{\pi}^{0} \sin\theta d\theta \qquad \textbf{(7.11)}$$

Hence:

$$H = \frac{I}{4\pi.y}.\left(\cos(0) - \cos(\pi)\right) \qquad \textbf{(7.12a)}$$

$$= \frac{I}{2\pi.y} \qquad 1 \qquad \textbf{(7.12b)}$$

Equation 7.12b is the solution to the magnetic field strength H at some point **p** a distance y from an infinitely long current carrying conductor. The case of the infinitely long conductor is, however, unrealistic. The case of the conductor of finite length was solved by evaluating equation 7.11 between realistic limits. Note, to

extract *exceptionally* accurate measurements from a Rogowski coil it is important to know the geometry of the conductor about which the coil is placed, as well as the details of the coil itself. The case of the magnetic field intensity determined a distance y from a conductor of total length $6y$ was considered. A similar evaluation of this problem was performed by Parton [**34**]. Equation 7.11 was re-solved accordingly:

$$H = \frac{I}{4\pi.y}.\left(\left(\frac{3y}{y\sqrt{3^2+1^2}}\right)-\left(\frac{-3y}{y\sqrt{3^2+1^2}}\right)\right) \qquad \textbf{(7.13a)}$$

$$= \frac{I}{4\pi.y}.\frac{6}{\sqrt{10}} \qquad \textbf{(7.13b)}$$

$$\approx 0.95 \times \frac{I}{2\pi.y}$$

Equation 7.13b indicates that *provided the current carrying conductor projects at least three times the distance from the conductor to the point* **p** *beyond either side of that point* **p**, *the calculated magnetic flux intensity will be at least 95% of that calculated using the infinite conductor formula given by equation 7.12*. It seems reasonable then, that, *under this condition* equation 7.12 may be used with the assurance of at least 95% accuracy. However, under the more stringent conditions of a shorter current carrying conductor it would be advisable to evaluate equation 7.11 *as per the specific geometry of the problem*. Under such conditions this was specifically the methodology of this work.

The output of a Rogowski coil is known to be a function of its geometry and the strength of the magnetic field to which it is coupled. The problem is not unlike that of a transformer, whose operation is also typically described as a function of magnetic field coupling between two electrically isolated current carrying conductors. Figure 7.3 shows a Rogowski coil equivalent circuit. In accordance with transformer notation the unknown *primary* current was denoted i_p, and the *secondary* current caused to flow in the Rogowski coil as a result thereof denoted i_s.

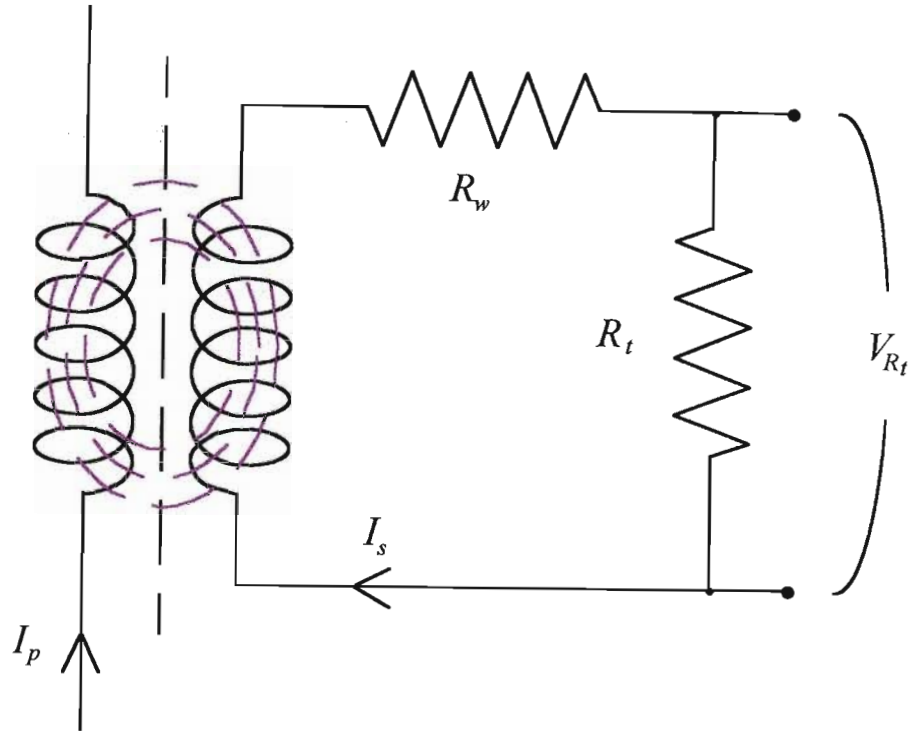

Figure 7.3 : Equivalent circuit of Rogowski coil magnetically coupled to a current carrying conductor

As is common with Rogowski coils, a terminating resistor, denoted R_t was placed across the output of the coil. The resistance of the coil, length l_w and of finite resistivity σ_w, was denoted R_w. The voltage measured across the terminating resistor was denoted V_{R_t}. The resistance of the wire R_w was calculated according to:

$$R_w = \frac{\sigma_w l_w}{A_w} \quad , \tag{7.14}$$

where A_w was the cross-sectional area of the wire wound onto the plastic former.

The case of a toroidal plastic former of major radius r, positioned concentrically around, but perpendicular to, a straight infinitely long current carrying conductor aligned along the x-axis of the co-ordinate system, was considered. The plastic former with windings is shown in Figure 7.4.

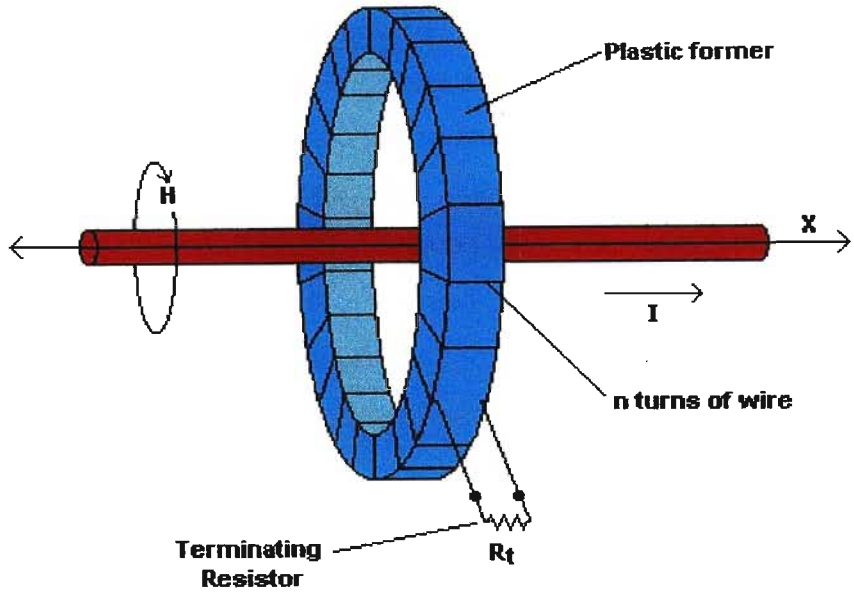

Figure 7.4 : A Rogowski coil positioned symmetrically around and perpendicular to a current carrying conductor.

Faraday's law states that the electromotive force V measured at the terminals of a loop of *perfectly conducting* wire is numerically equivalent to the negative rate of change of the magnetic flux ϕ intercepting that loop of wire. Hence, for n number of loops connected in series (termed a *solenoid*):

$$V = -n\frac{d\phi}{dt} \qquad \textbf{(7.15)}$$

Voltage V is therefore a function of the total magnetic flux ϕ which *links with* or is *coupled to* a conducting wire n times. This is referred to as n number of *flux linkages*. The magnetic flux ϕ is contributed to by numerous sources, including that due to a current caused to flow in the Rogowski coil. According to Kirchhoff's voltage law equation 7.15 was equated to the drop in potential across the finite resistance of the wire R_w, and the terminating resistor R_t. Hence:

$$-n\frac{d\phi_{ts}}{dt} = \left(R_w + R_t\right)i_s \qquad \textbf{(7.16)}$$

The subscripts t and s in the term ϕ_{ts} indicate that this is the *total* magnetic flux coupled with the *secondary* winding (the Rogowski coil), and *not* just that due the *primary*. In accordance with Ampere's law the Rogowski coil will generate its own *reciprocating* magnetic flux as a result of the current induced in the Rogowski coil windings. This magnetic flux opposes the magnetic flux of the current carrying conductor. The total magnetic flux ϕ_{ts} coupled with the Rogowski coil is therefore the sum of the *primary* magnetic flux ϕ_{ps} coupled to the secondary, and the *secondary* magnetic flux ϕ_{ss} coupled to the secondary. Equation 7.16 was therefore rewritten as:

$$-n\left(\frac{d\phi_{ps}}{dt}+\frac{d\phi_{ss}}{dt}\right)=\left(R_w+R_t\right)i_s \qquad \textbf{(7.17)}$$

The time derivative of the magnetic flux ϕ_{ps} was determined using equation 7.12 derived previously using the Biot-Savart law to determine the magnetic field strength H around the current carrying conductor. In a linear medium such as free space, where the relative magnetic permeability μ_r=1, the density B of any magnetic flux ϕ is known to be related to the magnetic field intensity H according to:

$$B=\mu_o H \qquad \textbf{(7.18)}$$

The quantity of magnetic flux ϕ_{ps} coupled to the coil (due to current i_p) is the integral of the magnetic flux density B integrated over the cross-sectional area S of the Rogowski coil.

Hence:

$$\phi_{ps}=\int_S B_p dS \qquad \textbf{(7.19a)}$$

$$=\mu_o\int_S H_p dS\ , \qquad \textbf{(7.19b)}$$

which, from equation 7.12b, was written as:

$$\phi_{ps}=\frac{\mu_o i_p}{2\pi}\int_S \frac{1}{y}dS \qquad \textbf{(7.20)}$$

Magnetic flux ϕ_{ps} is therefore proportional to the unknown current i_p. The dimensions of the Rogowski coil former were required to evaluate equation 7.20. Since the plastic Rogowski former was manufactured on a lathe it was convenient for the former to have a rectangular cross-section as per figure 7.4. The cross-section S was consequently defined as a rectangle of width $2a$ and height $2b$. Figure 7.5 shows the cross-section S positioned about the point **p** at a distance r from the current carrying conductor.

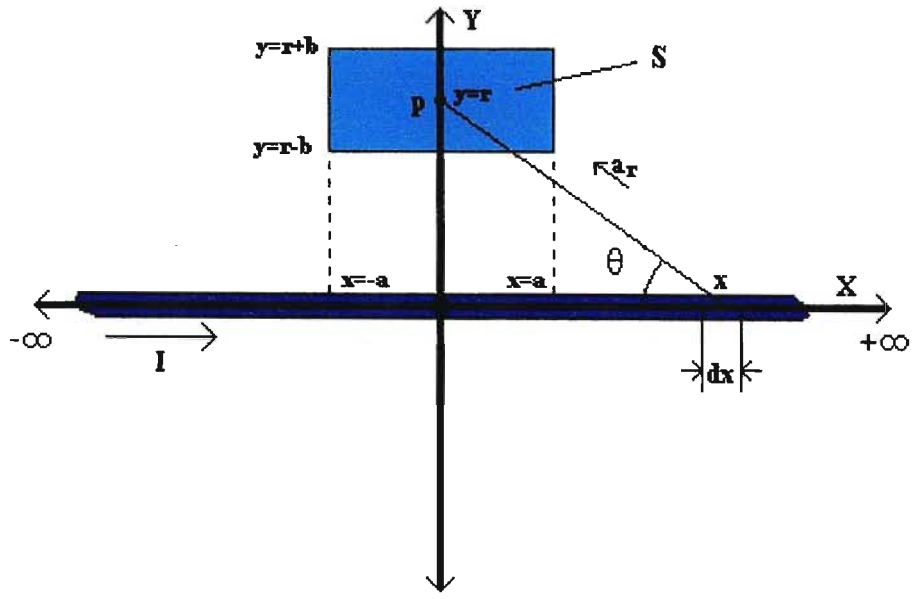

Figure 7.5 : Area S centred on the point **p** at a distance y from an infinitely long current carrying conductor positioned on the x-axis in the x-y plane.

Equation 7.20 was integrated between the limits of $x = \pm a$ and $y = r \pm b$ in order to determine the quantity of magnetic flux ϕ_{ps} coupled with the area S. Hence:

$$\begin{aligned}\phi_{ps} &= \frac{\mu_o i_p}{2\pi}\int_{x=-a}^{x=+a}\int_{y=r-b}^{y=r+b}\frac{1}{y}dydx \\ &= \frac{\mu_o i_p}{2\pi}\int_{x=-a}^{x=+a}\ln\left(\frac{r+b}{r-b}\right)dx \\ &= \frac{\mu_o i_p a}{\pi}\ln\left(\frac{r+b}{r-b}\right)\end{aligned} \qquad \textbf{(7.21)}$$

To complete the evaluation of equation 7.17 it was convenient to introduce the concepts of self and mutual inductance, as is typical in the analysis of any transformer. The inductance of any conductor is defined as the product of the magnetic flux and the number of flux linkages made by the magnetic flux with the conductor, divided by the current responsible for said magnetic flux. If the magnetic flux surrounding the conductor is purely as a result of the current flowing *in that same conductor*, then this is termed the *self inductance* of the conductor. If the magnetic flux is due to an *adjacent current carrying conductor*, then this is termed the *mutual inductance* of the conductor. The mutual inductance M of the Rogowski coil was therefore written as:

$$M = \frac{n \times \phi_{ps}}{i_p} \qquad \textbf{(7.22)}$$

where ϕ_{ps} was evaluated using equation 7.21. Similarly the self inductance L of the Rogowski coil was written as:

$$L = \frac{n \times \phi_{ss}}{i_s} \qquad \textbf{(7.23)}$$

Equation 7.21 was substituted into equation 7.22 to obtain a solution to the Rogowski coil mutual inductance M. Hence:

$$M = n \times \frac{\mu_o a}{\pi} \ln\left(\frac{r+b}{r-b}\right), \qquad \textbf{(7.24)}$$

It was preferred not to use the Biot-Savart law to determine the magnetic flux ϕ_{ss} coupled to the coil (due to current i_s), as was done for ϕ_{ps}. Instead an evaluation of ϕ_{ps} was made possible using the work of Grover [**35**]. Grover evaluated the self inductance of various geometry solenoids as a function of the magnetic flux coupled to these solenoids due to the current flowing therein. The self inductance L of the Rogowski coil, a toroidal solenoid, was determined by Grover to be:

$$L = L'k - \Delta L \ , \qquad \textbf{(7.25)}$$

where:

$$L' = \mu n^2 \frac{(2a)(2b)}{2\pi r} \tag{7.26}$$

and:

$$\Delta L = 2\mu n(G+\beta)\sqrt{\frac{ab}{\pi}} \tag{7.27}$$

For an air cored toroid k =1 and $\mu=\mu_o$. G is the winding space correction factor given as:

$$G = \frac{5}{4} - \ln\left(\frac{2p}{d}\right), \tag{7.28}$$

where p is the pitch of the windings and d the diameter of the wire. The pitch of the windings p is approximately equivalent to the mean circumference of the toroid divided by the number of turns on the solenoid. β is the empirical correction factor given by Grover as:

$$\beta = \sum_{i=0}^{3} c_i (\ln n)^i \ , \tag{7.29}$$

where:

$$\begin{aligned} c_o &= 0.00070 \\ c_1 &= 0.17730 \\ c_2 &= -0.03220 \\ c_3 &= 0.00197 \end{aligned} \tag{7.30}$$

Equations 7.22 and 7.23 were consequently substituted into equation 7.17 in order to evaluate Kirchhoff's voltage law as a function of the Rogowski coil self and mutual inductance parameters. Hence:

$$-\left(M\frac{di_p}{dt} + L\frac{di_s}{dt}\right) = (R_w + R_l)i_s \tag{7.31a}$$

$$= R_{tot} i_s \tag{7.31b}$$

where R_{tot}, the sum of the terminating resistor R_t and the resistance of the wire R_w, was defined as the total resistance of the Rogowski coil circuit. Since by Ohm's law:

$$i_s = \frac{V_{R_t}}{R_t} \tag{7.32}$$

then equation 7.31b was rewritten as

$$\frac{di_p}{dt} = -\frac{1}{M}\left(\frac{R_{tot}}{R_t}V_{R_t} + \frac{L}{R_t}\frac{dV_{R_t}}{dt}\right) \tag{7.33}$$

Equation 7.33 was then integrated in order to determine the primary current i_p (the current being measured) as a function of the known Rogowski coil output V_{R_t}. Hence:

$$i_p = \frac{-1}{MR_t}\left[\left(R_{tot}\int_o^t V_{R_t}dt\right) + LV_{R_t}\right] \tag{7.34}$$

Equation 7.34 determines the *primary* current *under all conditions* and is a general solution. Note, by definition, at time $t=0$, $i_p=0$.

In order to characterise a Rogowski coil such that its output V_{R_t} may be related back to the conductor carrying current i_p *with relative ease*, a number of substitutions and assumptions were made. Firstly, if the duration of the current pulse i_p is significantly less than L/R_{tot} (defined as the time constant of the coil) then the integral term in equation 7.34 will be small in comparison to the other of the terms. Hence, equation 7.34 reduces to:

$$i_p = \frac{-L}{MR_t}V_{R_t} \tag{7.35}$$

Equation 7.35 determines the primary current i_p as a *linear* function of the Rogowski coil output voltage under circumstances where the duration of current pulse i_p is

significantly *less* than the time constant of the Rogowski coil. In this *mode of operation* the Rogowski coil is referred to as being of the *"integrating"* type since it is as if the Rogowski coil output has already been integrated, such as would normally have to be applied to the output of the coil in order to solve equation 7.34. The *integrating* mode of operation is particularly useful since it enables one to view with ease the current flowing in the circuit under examination on an oscilloscope without the necessity for complex mathematical processing subsequent to or during the measurement process. The *integrating* type Rogowski coil may be manufactured to suit a specific application if the approximate pulse duration of the application is known. Integrating Rogowski coils can, however, be particularly difficult to engineer for long pulse durations since by adding more turns of wire to the coil (in order to increase the coils inductance) one is also automatically increasing the coils total resistance.

Secondly, if the duration of the current pulse i_p is significantly longer than the time constant of the coil, then the integral term in equation 7.34 will dominate over the other terms. Hence equation 7.34 reduces to:

$$i_p = \frac{-R_{tot}}{MR_t}\int_o^t V_{R_t}\,dt \qquad \textbf{(7.36)}$$

In this mode of operation the Rogowski coil is referred to as being of the *"differentiating"* type, since the Rogowski coil output is proportional to the time derivative of the primary current, and must be integrated in order to return a result linearly proportional to the measured current. This mode of operation is useful when one specifically desires to examine the rate of change of the measured current, but is, however, generally unavoidable for current pulses of particularly long duration where it is impossible to construct an integrating Rogowski coil. However, using modern technology it is not difficult to numerically integrate a sampled measurement from a differentiating Rogowski coil using, for example, a personal computer. Note, differentiating Rogowski coils are also more prone to electromagnetic noise due to the smaller current that flow in their windings.

7.3 A Numerical Model

The performance of a Rogowski coil within a given experiment may be predicted if the experiment in question has been mathematically modelled. Since the performance of the Rogowski coil is a function of its dimensions the geometric and size constraints of the experiment may very well determine the dimensions of the Rogowski coil. In this regard a combined model, which enables the output of the coil to be predicted as a result of the modelled experiment, is quite useful. Alternatively a Rogowski coil may be modelled as a standalone entity. In this case it is a requirement that the current within the known experiment be approximated in order to gauge the applicability and compatibility of the intended Rogowski coil to that experiment. For example, will the Rogowski coil be able to measure a current pulse of *such-and-such* duration, or, what will the approximate peak output voltage of the coil be into a *such-and-such* terminating resistor?

The classical solution to a simple RLC circuit may be used to approximate many pulsed power applications. Two or three lines of computer code are all that is required in order to define the primary current i_p to be measured by the Rogowski coil. This at least provides a basic foundation for the Rogowski coil design. The advantage of this sort of model is its simplicity. The disadvantage of this sort of model is that the reaction of the Rogowski coil to changes in the geometry of the particular experiment cannot be predicted. This author has included Rogowski coils, where applicable, in computer implemented mathematical models of various experiments. However, for the purpose of this text a standalone Rogowski coil model will be presented.

Given a *known* (that is to say predefined) time varying current $i_p(t)$ flowing in the primary conductor, equation 7.31 was solved for $i_s(t)$. Equation 7.31 contains the differential term $\frac{di_p(t)}{dt}$ which was determined from the time derivative of the defined current function $i_p(t)$. This was defined as the *"driving function"* $D(t)$ of equation 7.31, which was used to solve for the Rogowski coil current i_s. Equation 7.31 was therefore rewritten as:

$$R_{tot} i_s + L\frac{di_s}{dt} + MD(t) = 0 \qquad \textbf{(7.37)}$$

This particular 1st order differential equation was again solved numerically using the 4th/5th order variable step size Runge-Kutta-Fehlberg technique. Equation 7.37 was solved for its highest order derivative. Hence:

$$\frac{di_s}{dt} = -\frac{1}{L}\left(R_{tot} i_s + MD(t)\right) \qquad \textbf{(7.38a)}$$

$$= f\left(i_s\right) \qquad \textbf{(7.38b)}$$

At time $t=0$, i_p was zero by definition, therefore i_s was likewise zero. Equation 38a was evaluated to calculate $\frac{di_s}{dt}$ at $t=0$.

A Rogowski coil numerical model was implemented in the MATLAB mathematical programming language. The MATLAB program code for the Rogowski coil model is contained in Appendix F. The primary current was defined as an exponentially decaying sinusoid determined from the algebraic solution to a nearly critically damped RLC circuit. The variables R, L and C were included in the model in order that some control over the duration and magnitude of the current pulse could be exercised. By varying the period of the oscillation it was possible to examine specifically how well the Rogowski coil would respond to a primary current of longer or shorter duration.

Figure 7.6 shows the MATLAB predicted Rogowski coil output for both a *real* Rogowski coil (in blue) as defined by equation 7.34, and that for a fictitious *ideal* integrating Rogowski coil (in green) as defined by equation 7.35. This graph is unique to the specified parameters defined in the program code such as voltage, inductance, capacitance, number of turns, wire diameter etc. These values are all contained in Appendix F. Figure 7.6 indicates that the modelled *real* Rogowski coil is far from an ideal integrating device, in spite of the fact that it was designed as such. However, as the L/R_{tot} time constant of the Rogowski coil is increased the predicted *real* (blue) plot tends closer and closer to the predicted *ideal* (green) plot, causing the output of the Rogowski coil to tend closer and closer to the actual current under observation. The MATLAB model is a useful tool in the design of an *integrating* Rogowski coil since the ability of the coil to *integrate* may be visually evaluated. More importantly, an indication of sensitivity of the Rogowski coil is obtained. The

predefined driving function, $D(t)$, to which the Rogowski coil was predicted to respond is shown in figure 7.7.

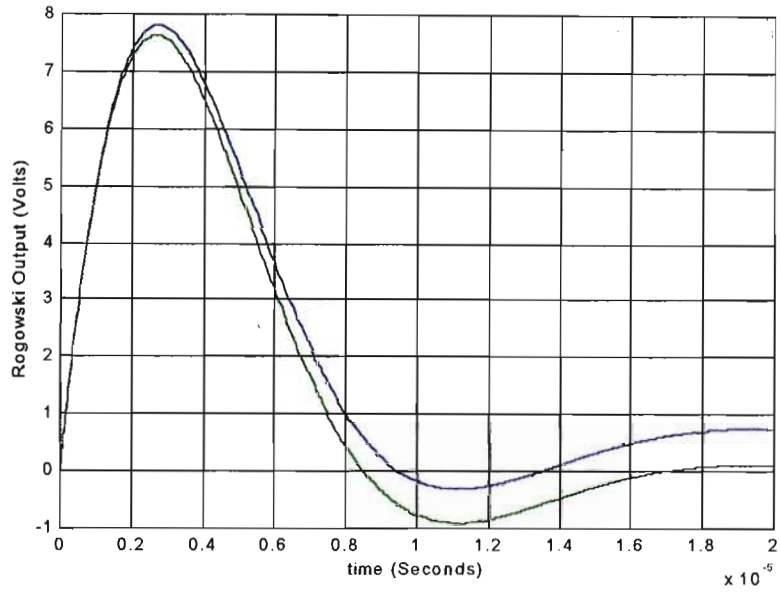

Figure 7.6 : Rogowski coil output verses time, predicted real coil in blue, predicted ideal integrating coil in green.

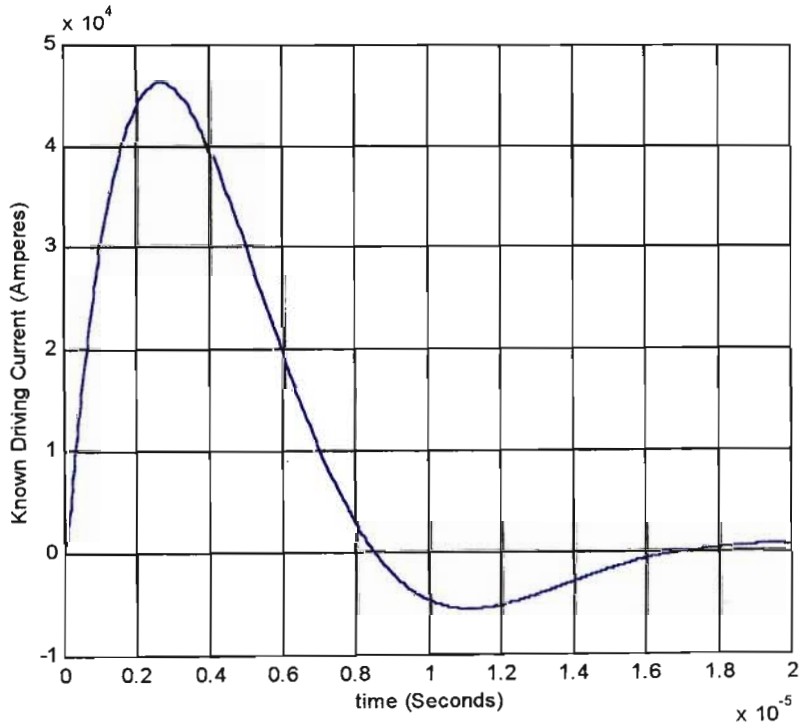

Figure 7.7 : Predefined driving current to which the Rogowski coil was predicted to respond.

7.4 A Manufactured Rogowski Coil

The design and manufacture of an integrating Rogowski coil capable of measuring a 100kA current pulse with rise time >500ns and pulse duration ~10μs was attempted. The Rogowski coil was intended for use around a Fuse Opening Switch (FOS), and was required to measure the current through the fuse wire as the wire moved from a conducting to non-conducting state. Owing to the geometry of the FOS experiment the former was restricted to an average major radius of r=45mm. Cross sectional dimensions of a=7.5mm and b=7.5mm were chosen. Using the model contained in Appendix F it was determined that the coil should be manufactured from 620 turns of 0.4mm thick enamelled copper wire. The self inductance L of the coil was predicted to be approximately 380μH, the mutual inductance M ~625nH, and the resistance of the coil wire R_w ~7.5Ω. A suitable terminating resistor was then chosen in order to a) ensure a L/R_{tot} time constant at least 5× greater than the 10μs pulse duration, and b) provide an output voltage of say 10V to 20V at 100kA peak measured current. Owing to the large resistance of the wire it was imperative not to increase the total resistance of the coil beyond the ~7.5Ω value which provided an upper limit on L/R_{tot} of 58μs. Fortunately the model indicated that the terminating resistance required to produce the desired output voltage signal was ~0.1Ω. Ten 2% 1Ω miniature carbon resistors were connected in parallel to produce a 0.1Ω terminating resistance, and positioned inside a cavity cut into the side of the former. The former was manufactured on a lathe from high density polyethylene (HDPE). The L/R_{tot} time constant was determined to be ~60μs.

Figure 7.8 shows the cross-section of the aluminium housing into which the coil and former was fitted. The housing was manufactured from two identical aluminium halves which bolted together using 8 off 3mm diameter stainless steel bolts. Note, the two inner edges of the housing *do not* make electrical contact. This is important in order to prevent the azimuthal magnetic field about the current carrying conductor coupling to the housing. If the housing were a closed circuit then the intended Rogowski coil winding current would reside in the housing, and not in the Rogowski coil, hence rendering the device useless!

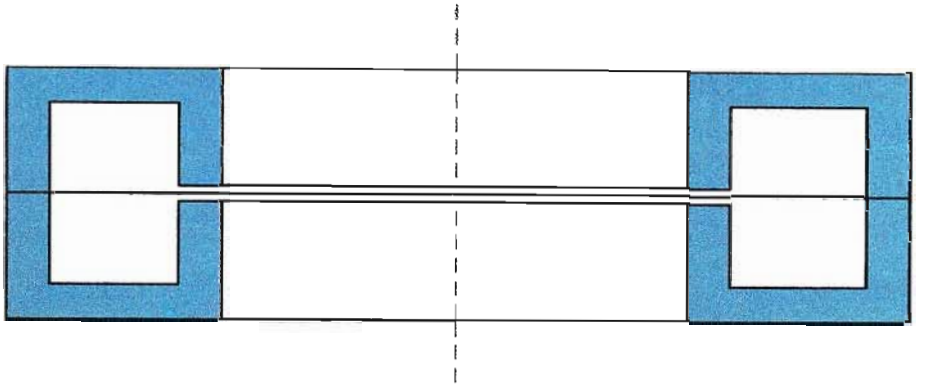

Figure 7.8: Cross-section of the aluminium housing designed to prevent the capacitive coupling of the coil windings to the high voltage apparatus.

Approximately 2m of 50Ω RG-58 coaxial cable was connected to the coil output (across the 0.1Ω resistance) and terminated at the input to a digital storage oscilloscope with a 50Ω coaxial termination. Since the ~0.1Ω output impedance of the Rogowski coil was significantly less than the 50Ω cable and termination, the cable and termination had little or no effect on the recorded signal. To prevent electrical noise penetration into the Rogowski coil coaxial cable an additional screen was placed over the length of RG-58. The screen was obtained from the outer conductor of a length of RG-213 coaxial cable, which fitted easily over the outside of the length of RG-58 cable. The outer screen was attached to the Rogowski coil housing by silver-soldering the copper screen to a ¼ inch NPT fitting, which was modified in the lathe, and then screwed into the hole drilled in the side of the Rogowski housing, through which the RG-58 was threaded.

Figure 7.9 shows a Rogowski coil after the 620 turns of 0.4mm diameter enamelled copper wire were applied to the HDPE former. Commercial electricians tape was wound over the windings as they were applied in order to hold them in place. Figure 10 shows the detail of one half of the Rogowski coil enclosure.

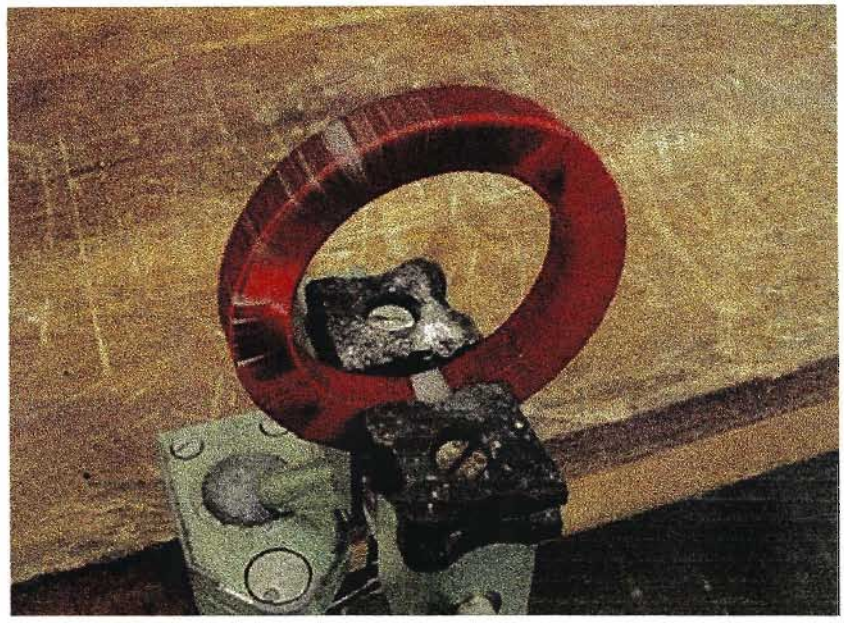

Figure 7.9 : The Rogowski coil former with 620 turns of 0.4mm diameter copper wire applied

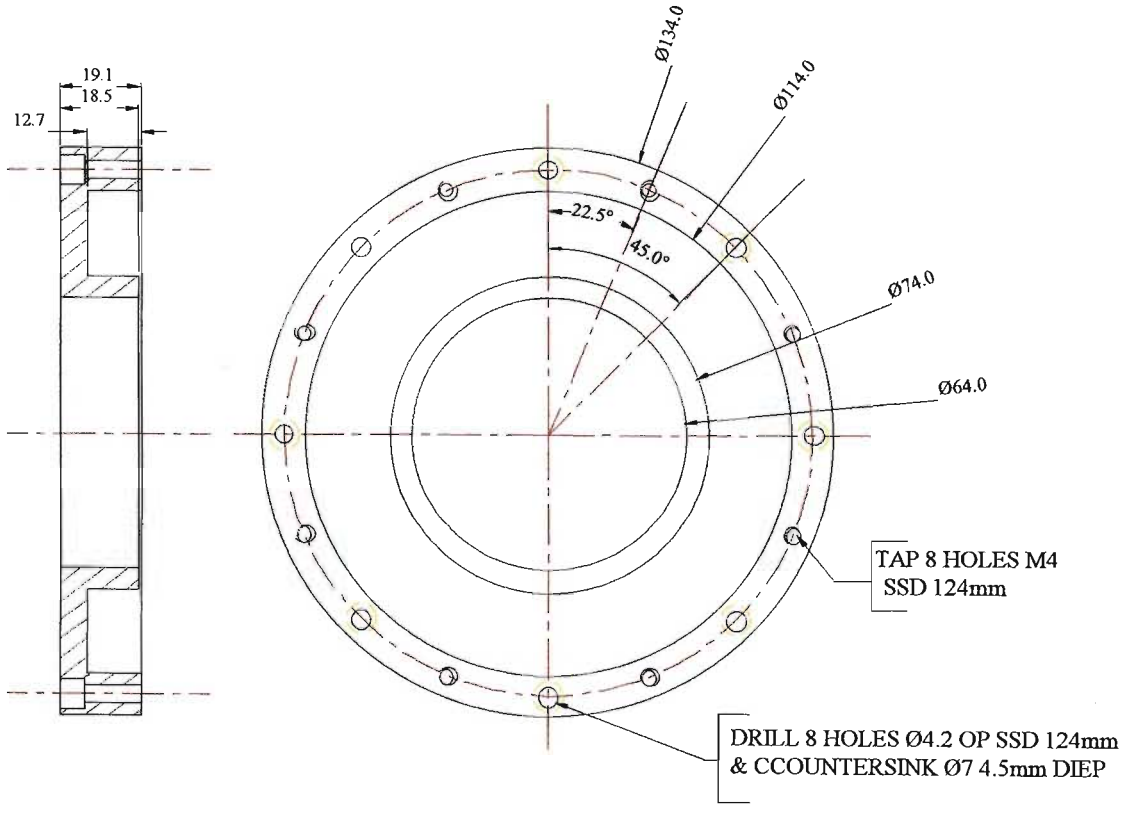

Figure 7.10 : A detailed drawing of one half of the Rogowski coil housing.

Both mains borne and radiated electromagnetic noise was anticipated during the exploding wire experiment due to the magnitude of the predicted currents and geometry of the apparatus. Electrical noise was observed throughout the work presented in this text to be induced in nearby cables as a result of three mechanisms, namely a) electric (capacitive) coupling due to cables passing through regions of strong electric field, b) magnetic coupling due cables coupling to strong magnetic fields and c) via both mechanisms back into the mains supply via power supplies, trigger boxes, vacuum stations etc. Electrical noise is difficult to quantify since it is a function of a) the magnitude of the currents and voltages in the experiment, b) the proximity of the experiment to noise susceptible wires and cables (for example, cables to vacuum gauges and vacuum pumps) and c) the geometry of these cables (for example, coaxial, twisted-pair, etc.) This includes all mains electrical cables.

In most cases electromagnetic *noise* was not observed to be radiated as a self sufficient electromagnetic wave, as is commonly believed to occur. In fact, when carefully designed, pulsed power experiments display an inherent *inability* to transmit or *far field couple* themselves to adjacent equipment. The *near field* coupling of either the magnetic field or electric field (or both) around an apparatus *was* however a specific problem that was often required to be addressed. If the correct design procedures were followed these problems were reduced to a minimum. Unfortunately, with the high voltage vacuum experiments requiring pumps, gauges, and other diagnostic tools, it was impossible to alleviate these problems altogether. Noise transferred onto the main electrical supply was observed to have adverse effects on sensitive measurement equipment.

Noise carried back into the main electrical supply is often referred to as *conducted* noise. Conducted noise was observed to be particularly damaging during the measurement process since measurement equipment well hardened against other forms of noise could not, in general, be operated disconnected from the main electrical supply (in-line filters were an insufficient solution in such a hostile environment). It is for this reason that all Rogowski coil measurements were performed using a battery operated Tektronix THS-720 digital storage oscilloscope housed within a metallic enclosure. The enclosure was manufactured from 5mm thick aluminium plate welded along all edges to form a housing impervious to, in particular, any lines of magnetic flux that may have otherwise attempted to couple to

the oscilloscope. Liquid crystal displays on compact oscilloscopes were observed to be highly receptive to magnetic noise, carrying the noise back into the oscilloscope internal circuitry! Note: Aluminium is non-magnetic, but highly conductive. Hence lines of fast time varying magnetic flux were not able to penetrate due to eddy currents established in the enclosure. However, static or slowly varying magnetic fields were able to penetrate the enclosure. However, since such slowly varying fields were of little consequence the aluminium enclosure was considered to be an acceptable form of screen. The lid of the enclosure, which for obvious reasons could not be welded shut, was held down with clamps to form a conductive seal. The inside face and upper edge of the enclosure were machined flat to ensure a close fit. The additional screen placed around the 2m length of RG-58 coax attached to the Rogowski coil was attached to the aluminium oscilloscope enclosure using a brass disc. Figure 7.11 shows the manufactured Rogowski coil positioned inside the vessel within which the exploding wire apparatus was positioned. Adjacent to the Rogowski coil is the aluminium oscilloscope enclosure, oscilloscope and lid.

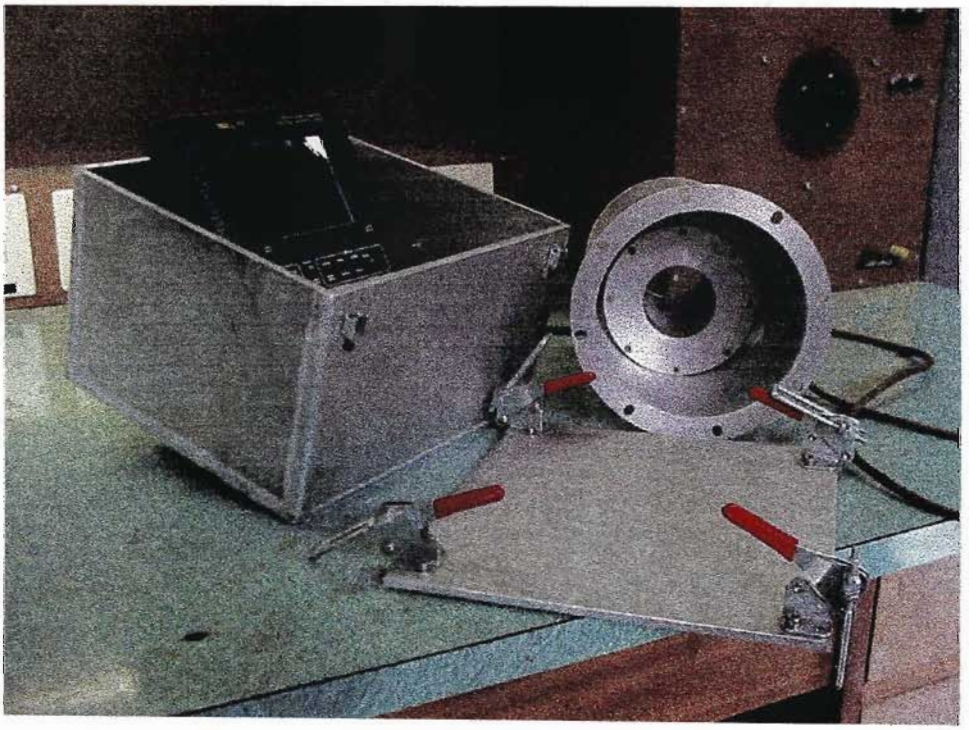

Figure 7.11 : Rogowski coil as a part of the exploding wire experiment with the oscilloscope enclosure.

7.5 Data Extraction Using Digital Techniques

A Rogowski coil is, in reality, neither capable of *integration* nor *differentiation*. However, by designing a Rogowski coil such that its characteristic L/R_{tot} time constant is significantly longer than the measured current pulse, a *convenient proportional relationship* between the current under observation and the coil output is invoked. (A similar argument applies to the *differentiating* Rogowski coil). This *trick* of the mathematics is undoubtedly useful since the coil output is easier to relate to. However, given that a Rogowski coil of arbitrary time constant will return data regardless, a meaningful current measurement may be extracted from this data *subsequent* to numerical processing performed in accordance with equation 7.34. The numerical processing of a measured waveform was made difficult in the past due to difficulties in storing measurement data for later mathematical analysis. However, using digital technology, it is possible to download data into a PC from a digital storage oscilloscope and invoke numerical integration and numerical differentiation techniques in order to extract recognisable wave-forms from that which was previously unrecognisable. This technique is possible only if the parameters of the Rogowski coil are accurately known. If the coil was designed by the user it is likely that these would have been well documented during the design and manufacture process, as was the case with this work.

The process of numerically integrating or differentiating data in no way enhances or falsifies the recorded data provided no interpolating or *best fit* techniques are employed. Indeed, if the same number of data samples are employed during numerical integration and differentiation, as were sampled by the digital storage oscilloscope, the data will be neither enhanced nor degraded. If fewer samples are employed than were recorded, the data quality will be degraded. If additional samples are created by, for example, passing an interpolating polynomial through the samples, the data will be enhanced. If the interpolating polynomial is intelligent enough it may very well produce data truer to reality than that originally sampled. The data will therefore be enhanced, but not necessarily falsified. However, since no polynomial can accurately predict what may have occurred at any given moment between two consecutive samples this technique is best avoided.

A digital storage oscilloscope may, for example, store a Rogowski coil measurement as 2500 individual samples. The exact number of samples, sampling speed, resolution, analogue bandwidth etc. will obviously differ from oscilloscope to oscilloscope. Using a serial cable or floppy disc (provided the oscilloscope has this facility) the recorded data may be transferred to a PC where it may be processed. The simplest manner in which the data may be handled is within a spreadsheet environment such as Microsoft Excel™. The data should be imported into the spreadsheet and arranged sequentially down the page. One column should contain the time data and the other the voltage data.

Figure 7.12 shows a small portion of the *real* (not sampled) output of a fictitious Rogowski coil as a function of time. Marked on the waveform is a number of consecutive voltage samples generated by a digital storage oscilloscope, separated on the x-axis by the time interval Δt.

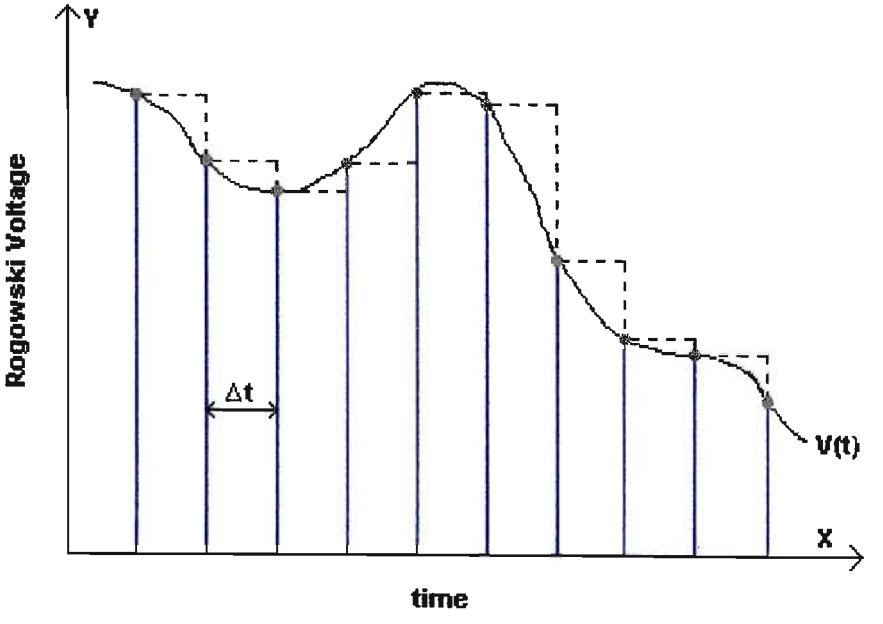

Figure 7.12 : A portion of the waveform sampled by a digital storage oscilloscope.

The integral of the Rogowski output with respect to time is effectively the area under the measured waveform. The best interpretation that can be made of the sampled data is to spread the value of each sample over the duration of the sample Δt. Any effort to join or interpolate the samples will require some assumption to be made with regard to the Rogowski coil output in between sampling events. The integral of

the Rogowski coil output may therefore at best be approximated by the sum of the area of the rectangles under each sample spread over the duration Δt. The integral of $V(t)$ with respect to time, the sum of the areas of the rectangles, may be determined according to:

$$\int V(t)dt \cong \sum_{q=1}^{q=Q} v(q) \times \Delta t \,, \tag{7.39}$$

where $v(q)$ is the sample value of the q^{th} sample out of a total of Q samples. Δt is calculated as:

$$\Delta t = t(q+1) - t(q) \,, \tag{7.40}$$

where $t(q)$ is the time at which the q^{th} sample was recorded.

Equation 7.39 determines the integral of the Rogowski coil output as a function of discrete samples. Equation 7.39 was applied to equation 7.34 in order that the measured current could be determined at the discrete time intervals defined by the digital storage oscilloscope. Hence:

$$i_p(q) = \frac{-1}{MR_t}\left(\left(R_{tot}\sum_{q=1}^{q=Q} v(q) \times \Delta t\right) + Lv(q)\right) \tag{7.41}$$

Equation 7.41 relies on a sound knowledge of the values L, M, R_t and R_{tot}.

Since the L/R_{tot} time constant of a Rogowski coil will never be infinite it is impossible to construct an *integrating* Rogowski coil with a totally insignificant differential term in its output. This has the effect of introducing a subtle distortion into the measurement, as in figure 7.6, which will worsen at longer and longer pulse durations.

7.6 High Frequency Limitations

This work has thus far indicated that the rise-time and decay-time of the Rogowski coil output, in response to a time changing magnetic field about a current carrying conductor, is a function of the coils inductance (both self and mutual) and resistance. Till now, however, the subject of distributed capacitance has been avoided. According to Stygar and Gerdin any stray or distributed capacitance within the coil must be taken into account in order to determine the high frequency response of a Rogowski coil. As a result of distributed capacitance a Rogowski coil becomes a transmission line device, characterised by its distributed R, L and C values, with a characteristic transit time given by:

$$t_r \cong \sqrt{LC} \qquad \textbf{(7.42)}$$

where L is the inductance of the coil, and C an equivalent capacitance term as a function of the inter-winding capacitance (capacitance between turns) and the coil to screen capacitance. This value is most easily determined for a given manufactured Rogowski coil using a network analyser in order to determine the resonant frequency (proportional to the inverse of the transit time) of the device. However, for pulse rise-times significantly above the characteristic transit time t_r of the transmission line structure, the effect of the distributed capacitance need not be included in the mathematics of the device and a transmission line type analysis need not be applied. For the specific applications dealt with in this text rise-times of around a microsecond were typical, and well beyond the expected rise-time of a typical Rogowski coil, which should, for a good design, be less than a few nanoseconds. Indeed, the work of Pellinen *et al* [**36**] describes rise-times of less than a nanosecond for a uniformly excited device. That is to say the magnetic field of the current carrying conductor couples equally to *all* turns on the Rogowski coil. Pellinen *et al* refer specifically to the problem a Rogowski coil not positioned on or parallel to the major axis of the Rogowski coil. Under such conditions the magnetic field of the conductor does not couple equally to all turns of the coil. Since the coil has a finite transit time the EMF developed in one turn of the coil will not reach the terminating resistor at the same time as that due to another turn. Pellinen *et al* have shown that owing to this effect a non-uniformly exited coil will show undesired oscillations at its output.

Many Rogowski coil designs make use of a length of flexible coaxial cable to form the coil section. The outer insulation and outer conductor (*braid*) are stripped back by a length equivalent to the circumference of the Rogowski coil and the required number of turns wound over the inner dielectric layer. The coil is connected between the edge of the *braid* and the tip of centre conductor, and then bent into a circular form. Hence, the return conductor of the Rogowski coil passes *through* the centre of the Rogowski coil. The coil and the centre conductor are therefore separated by the coax dielectric. A Rogowski coil is intended to operate such that the azimuthal magnetic field surrounding a current carrying conductor couples to the wire turns wound onto the coil former. However, with a conventional design Rogowski coil any *axial* magnetic field component will also couple to the major loop of the Rogowski coil and cause the coil output to be in error. The *coaxial* design Rogowski coil has the advantage of no major loop, since the coil folds back on itself via the inner coaxial conductor. The coaxial design Rogowski coil is therefore impervious to any axial magnetic field component. The distributed capacitance of the coaxial Rogowski coil is, however, greatly increased, as is the rise-time capability of the Rogowski coil. This style of Rogowski coil was therefore avoided. However, Pellinen *et al* state that the electrostatic screen placed around the Rogowski coil discriminates against any axial magnetic field since the screen forms a single short circuit turn about the major axis of the coil. Hence, with the conventional design Rogowski, a screened housing is a requirement, not only in order to avoid the possibility of electric field coupling!

7.7 Results

The Rogowski coil was calibrated using a Pearson™ current transformer positioned with the Rowoski coil around a conductor through which was passed a 3kA peak over-damped sinusoidal current pulse of duration ~2.8μs. Since it was possible to measure the former dimensions, the number of turns, the coil self inductance and coil resistance accurately, no further calibration other than that required to verify the correct operation of the Rogowski coil was required.

Figure 7.13 shows the sampled Rogowski coil output (2500 samples recorded with a Tektronix THS-720 oscilloscope) as a result of the current passed through the 210mm long × 0.7mm thick FOS described in section 6.6. Note, the waveform shown in figure 7.13 does not appear to return to zero, but instead settles to a steady state condition of approximately -1V. This is as a direct result of the non-negligible differential term within the Rogowski coil output. When observed over a longer time period this steady state condition is more easily recognised as an exponentially decaying waveform with decay time approximately five times the time constant of the coil.

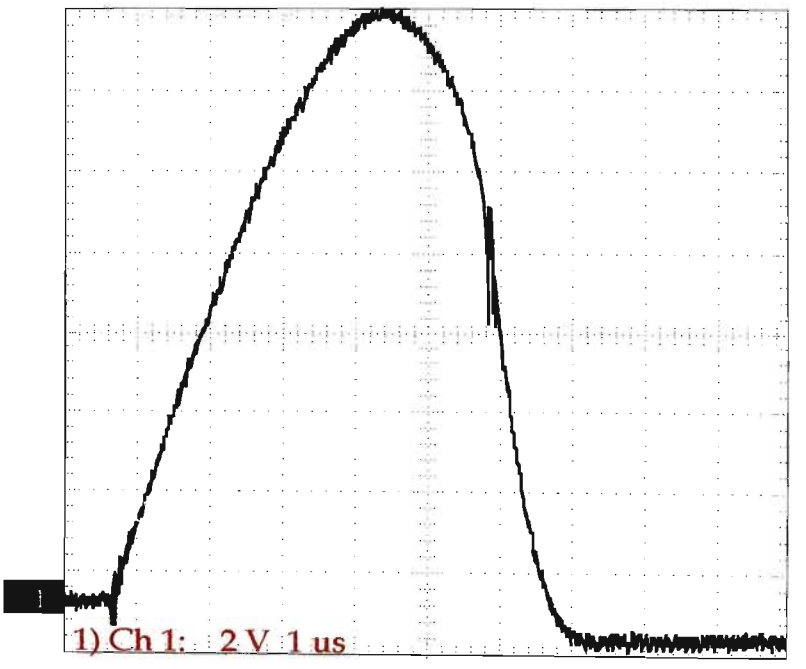

Figure 7.13 : Sampled Rogowski coil output. Y-axis = 2V/div, X-axis = 1μs/div.

While figure 7.13 is a fair representation of the current through the FOS, the mathematical procedure detailed in section 7.5 was implemented in order to derive a more accurate measurement of the FOS current. Figure 7.14 shows the same waveform subsequent to numerical processing. Data was downloaded to a Pentium-I personal computer via a RS-232 cable connected to the computers serial port. The data was then imported into Microsoft Excel where a spreadsheet was set up to process the data. Unlike figure 7.13 the waveform in figure 7.14 clearly *does* in fact settle to a steady state value of zero. This is as was anticipated

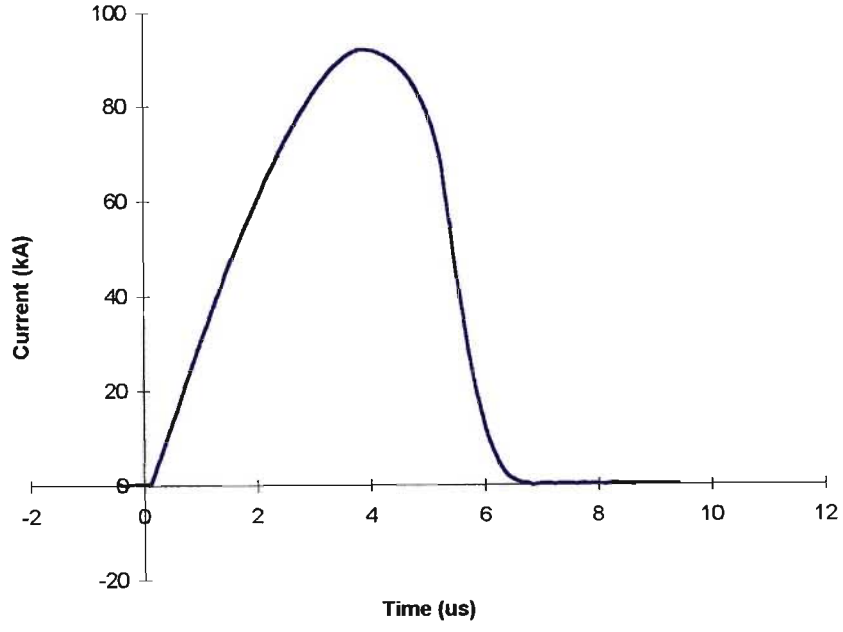

Figure 7.14 : The numerically evaluated Rogowski coil output.

7.8 Conclusions

This chapter has dealt with both the theoretical and practical considerations of a Rogowski coil designed and manufactured to measure a current pulse of duration approximately 10μs and peak magnitude approximately 100kA. The measured current pulse was approximately 6μs in duration, and of peak magnitude 90kA. Under these conditions the Rogowski coil was shown to produce a full scale deflection of approximately 15V. It was further shown how the recorded data could be manipulated using a basic signal processing technique in order that the flow of current within the current carrying conductor be accurately determined. A method of shielding the Rogowski coil and oscilloscope against erroneous electrical noise was also presented. Sufficient theory and modelling was presented to enable the future design of other Rogowski coils. A $4^{th}/5^{th}$ order Runge-Kutta-Fehlberg numerical model was presented.

The design and manufacture of the Rogowski coil discussed in this chapter may be summarised as follows:

- The magnitude and duration of the current pulse to be measured was determined as accurately as possible (by prediction or calculation).
- The space available around the current carrying conductor was determined in order that the Rogowski coil with its housing be able to fit the application.
- The coil was designed, based on the available space, such that its characteristic time constant was longer than the predicted current pulse duration, and that a reasonably sized output would be generated which could be fed into a digital storage oscilloscope.
- A basic mathematical model of the driving function was specified such that it approximated the current pulse to be measured.
- The Rogowski coil was added to the to the model in order to examine its response to the predicted current flow.
- The necessary design changes were made in order to improve the operation of the Rogowski coil.
- The Rogowski coil with its aluminium housing was manufactured, assembled, calibrated, and finally tested.

Appendix A:

Flash-lamp circuit analysis:

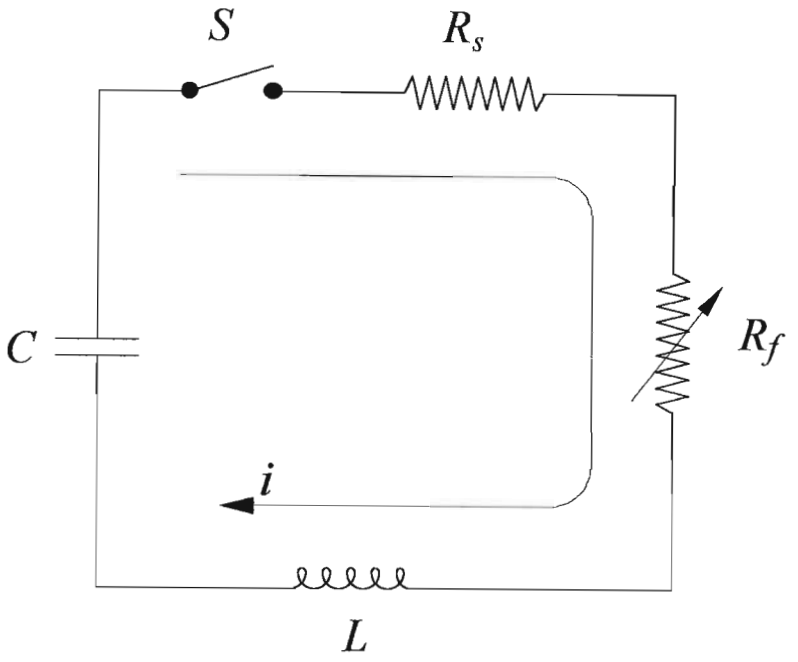

According to Kirchhoff's voltage law the sum of the voltages around the circuit is:

$$\frac{1}{C}\int i dt + R_s i + R_f i + L\frac{di}{dt} = V_o \ , \qquad \textbf{(A.1)}$$

where V_o is the voltage to which capacitor C is charged prior to the discharge event when switch S is closed at time $t = 0$.

In order to simplify equation A.1 the following relations were defined:

$$T = \sqrt{LC} \ , \qquad \textbf{(A.2a)}$$

$$Z_o = \sqrt{\frac{L}{C}} \ , \qquad \textbf{(A.2b)}$$

$$\tau = \frac{t}{T} \qquad \textbf{(A.2c)}$$

From equation A.2c:

$$dt = Td\tau \tag{A.3}$$

Equations A.2 and A.3 were substituted into equation A.1:

$$Z_o \int id\tau + R_s i + R_f i + Z_o \frac{di}{d\tau} = V_o \tag{A.4}$$

The current I was further conveniently defined according to:

$$I = i\frac{Z_O}{V_O} \tag{A.5}$$

Rearranging equation A.5 and substituting into equation A.4:

$$\int Id\tau + \frac{R_s}{Z_o} I + \frac{R_f}{Z_o} I + \frac{dI}{d\tau} = 1 \tag{A.6}$$

The constant β was defined according to:

$$\beta = \frac{R_s}{Z_o} \ . \tag{A.7}$$

Equations A.2 through A.3 and equation A.5 were substituted into equation 4.3 (chapter 4) in order to evaluate the resistance of the discharge column. Hence:

$$R_f = 1.28\frac{l}{d} \times \frac{d}{d_a} \times \frac{1}{\sqrt{|I|}} \times \frac{Z_o}{\sqrt{V_o Z_o}}$$

$$= \frac{Z_o \alpha}{\sigma} \times \frac{1}{\sqrt{|I|}} \ , \tag{A.8}$$

where from equation A8:

$$\alpha = 1.28\frac{l}{d\sqrt{V_o Z_o}} \quad , \tag{A.9}$$

and:

$$\sigma = \frac{d_a}{d} \quad . \tag{A.10}$$

Hence, equation A.6 was written as:

$$\int I d\tau + \beta I + \frac{\alpha}{\sigma}\frac{I}{\sqrt{|I|}} + \frac{dI}{d\tau} = 1 \tag{A.11}$$

Equation A.10, the ratio of filament diameter to bore diameter, was determined from the work of Dishington *et al* [**11**] to be:

$$\sigma = \frac{1.5(\varepsilon)^{0.6}}{d} \quad , \qquad \sigma \le \sigma_c \tag{A.12a}$$

$$\sigma = \frac{0.77(\varepsilon)^{0.077}}{d} \quad , \qquad \sigma > \sigma_c \tag{A.12b}$$

where σ_c is the critical filament to bore diameter ratio beyond which the rate of expansion of the filament is observed to slow, where:

$$\sigma_c = 0.7d^{0.15} \tag{A.13}$$

and ε is the energy deposited into the filament per cm length of the lamp according to:

$$\varepsilon = \frac{1}{l}\int i^2 R_f dt \tag{A.14}$$

Equations A.2 through A.3, A.5 and A.8 were substituted into equation A.14. Hence:

$$\varepsilon = \frac{T}{l}\left(\frac{V_o}{Z_o}\right)^2 \int \left(\frac{I^2}{\sqrt{|I|}}\frac{\alpha Z_o}{\sigma}\right) d\tau$$

$$= \frac{\alpha C V_o^{\,2}}{l}\int \frac{I^2}{\sigma\sqrt{|I|}}\, d\tau$$

$$= 2\varepsilon_o \alpha \int \frac{I^2}{\sigma\sqrt{|I|}}\, d\tau \qquad \textbf{(A.15)}$$

where:

$$\varepsilon_o = \frac{C V_o^{\,2}}{2l} \qquad \textbf{(A.16)}$$

is the total energy in Joules stored in the capacitor per cm length of the flash-lamp.

The variable step size Runge-Kutta-Fehlberg [**14**] method for the numerical solution of differential equations was used to solve for the time dependant flash-lamp current i and lamp power ε. In accordance with the Runge-Kutta-Fehlberg method equations A.11 and A.15 were differentiated and rearranged to solve for their highest order derivative. From equation A.11:

$$\ddot{I} = -\left[I + \beta\dot{I} + \alpha\left(\frac{\dot{I}}{2\sigma\sqrt{|I|}}\right) - k\alpha\left(\frac{\dot{\sigma}\sqrt{|I|}}{\sigma^2}\right)\right] \qquad \textbf{(A.17)}$$

where $k = 1$ for $I \geq 0$ or $k = -1$ for $I < 0$, and from equation A.15:

$$\dot{\varepsilon} = \frac{2\varepsilon_o \alpha}{\sigma}\frac{I^2}{\sqrt{|I|}} \,. \qquad \textbf{(4.18)}$$

The dot notation at all times implied a derivative with respect to τ.

To evaluate equation A.17, σ, the ratio of filament diameter to bore diameter, and its derivative were solved for. This was achieved by taking the derivative of equations A.12(a) and A.12(b) with respect to τ. Hence:

$$\dot{\sigma} = \frac{0.9\varepsilon^{-0.4}}{d}\dot{\varepsilon}, \qquad \sigma \le \sigma_c \qquad \textbf{(A.19a)}$$

$$\dot{\sigma} = \frac{0.0593\varepsilon^{-0.923}}{d}\dot{\varepsilon}, \qquad \sigma > \sigma_c \qquad \textbf{(A.19b)}$$

Equations A.12(a) and 4.12(b) and equation A.18 were substituted into A.19(a) and A.19(b). Hence:

$$\dot{\sigma} = 2.359\frac{\varepsilon_o \alpha}{(\sigma d)^{5/3}}\frac{I^2}{\sqrt{|I|}}, \qquad \sigma \le \sigma_c \qquad \textbf{(A.20a)}$$

$$\dot{\sigma} = 5.126\times 10^{-3}\frac{\varepsilon_o \alpha}{(\sigma d)^{13}}\frac{I^2}{\sqrt{|I|}}, \qquad \sigma > \sigma_c \qquad \textbf{(A.20b)}$$

Equations A.17 and A.19(a) and A.19(b) were then solved for I and σ simultaneously. The step size was controlled as a function of the magnitude of the error in I after each iteration, and was initially set to around τ/10000. The numerical model, implemented in the MATLAB mathematical programming language is contained in Appendix B.

Appendix B:

```
%--------------------%
%- FLASH-LAMP MODEL -%
%--------------------%

%This model predicts the current through a linear flash-lamp as a
%function of the lamp and discharge circuit parameters.

echo off;

%FLASHLAMP DIMENSIONS
l=150;                      %Lamp length
d=1.4;                      %Lamp bore diameter

%CIRCUIT PARAMETERS
Vo=35e3;                    %Charging voltage
Rp=0.0005;                  %Circuit resistance
Lp=2e-6;                    %Circuit Inductance
C=3e-6;                     %Storage capacitance

Eo=0.5*C*(Vo^2)/l;          %Energy per unit lamp length
Energy=0.5*C*(Vo^2)         %Capacitor energy

T=(Lp*C)^.5;                %Circuit time constant
Zo=(Lp/C)^.5;               %Circuit impedance
Rmin=1000;

%CONSTANTS
kap=1.28;
a=kap*l/(d*sqrt(Vo*Zo));
b=Rp/Zo;

%ROGOWSKI COIL PARAMETERS
N=620;

aa=7.5e-3;
bb=7.5e-3;
rr=45e-3;
ab=2*sqrt(aa*bb/pi);

Rcv=.1;
RHO=.175;
length=N*(sqrt(((2*pi*rr/N)^2)+((4*(aa+bb))^2)));
Rwire=length*RHO;

Rs=Rcv+Rwire
wd=.4e-3;
mu=4*pi*1e-7;
G=((-5/4)+log(4*pi*rr/(wd*N)));
H=(7e-4)+(0.1773*log(N))-(3.22e-2*((log(N))^2))+(1.97e-
3*((log(N))^3));

M=N*(mu*bb/pi)*log((rr+aa)/(rr-aa))
Lapprox=2*mu*(N^2)*aa*bb/(pi*rr);
Ls=mu*ab*N*((N*ab/(2*rr))+G-H)

TORR=Ls/Rs;
```

```
%INITIAL VALUES
n=1;
S=(15*1/Vo);
Sc=0.7*(d^0.15);

I=0.005;
dI=1-(a*(I^.5)/S)-(b*I)
Is=0;

Sigma(n)=S;
Cur(n)=I*Vo/Zo;
dCur(n)=dI*Vo/Lp;
Curs(n)=0;
Res(n)=kap*1*((I*Vo/Zo)^-0.5)/(S*d);

torr=0;
time(n)=0;
h=1/10000;

while (torr*T)<12e-6
%while I>=0

   n=n+1;

   if S<Sc
      q=2.6;
      p=5/3;
   else
      q=5.126e-3;
      p=13;
   end

   if I<0
      k=-1;
   else
      k=1;
   end

   %part 1
   tS=S;
   tdI=dI;
   tI=I;
   tIs=Is;

   tdS=q*Eo*a*abs(tI)*(sqrt(abs(tI)))/((tS*d)^p);

   k1S=h*tdS;
   k1I=h*tdI;
   k1dI=-h*((tI)+(b*tdI)+(a*tdI/(2*tS*sqrt(abs(tI))))-
((a*k*tdS*sqrt(abs(tI)))/(tS^2)));
   k1Is=(h/Ls)*((M*tdI)-(T*Rs*tIs));

   %part 2
   tS=S+(k1S/4);
   tdI=dI+(k1dI/4);
   tI=I+(k1I/4);
   tIs=Is+(k1Is/4);

   tdS=q*Eo*a*abs(tI)*(sqrt(abs(tI)))/((tS*d)^p);

   k2S=h*tdS;
   k2I=h*tdI;
   k2dI=-h*((tI)+(b*tdI)+(a*tdI/(2*tS*sqrt(abs(tI))))-
((a*k*tdS*sqrt(abs(tI)))/(tS^2)));
```

```
   k2Is=(h/Ls)*((M*tdI)-(T*Rs*tIs));

   %part 3
   tS=S+(3*k1S/32)+(9*k2S/32);
   tdI=dI+(3*k1dI/32)+(9*k2dI/32);
   tI=I+(3*k1I/32)+(9*k2I/32);
   tIs=Is+(3*k1Is/32)+(9*k2Is/32);

   tdS=q*Eo*a*abs(tI)*(sqrt(abs(tI)))/((tS*d)^p);

   k3S=h*tdS;
   k3I=h*tdI;
   k3dI=-h*((tI)+(b*tdI)+(a*tdI/(2*tS*sqrt(abs(tI))))-
((a*k*tdS*sqrt(abs(tI)))/(tS^2)));
   k3Is=(h/Ls)*((M*tdI)-(T*Rs*tIs));

   %part 4
   tS=S+(1932*k1S/2197)-(7200*k2S/2197)+(7296*k3S/2197);
   tdI=dI+(1932*k1dI/2197)-(7200*k2dI/2197)+(7296*k3dI/2197);
   tI=I+(1932*k1I/2197)-(7200*k2I/2197)+(7296*k3I/2197);
   tIs=Is+(1932*k1Is/2197)-(7200*k2Is/2197)+(7296*k3Is/2197);

   tdS=q*Eo*a*abs(tI)*(sqrt(abs(tI)))/((tS*d)^p);

   k4S=h*tdS;
   k4I=h*tdI;
   k4dI=-h*((tI)+(b*tdI)+(a*tdI/(2*tS*sqrt(abs(tI))))-
((a*k*tdS*sqrt(abs(tI)))/(tS^2)));
   k4Is=(h/Ls)*((M*tdI)-(T*Rs*tIs));

   %part 5
   tS=S+(439*k1S/216)-(8*k2S)+(3680*k3S/513)-(845*k4S/4104);
   tdI=dI+(439*k1dI/216)-(8*k2dI)+(3680*k3dI/513)-(845*k4dI/4104);
   tI=I+(439*k1I/216)-(8*k2I)+(3680*k3I/513)-(845*k4I/4104);
   tIs=Is+(439*k1Is/216)-(8*k2Is)+(3680*k3Is/513)-(845*k4Is/4104);

   tdS=q*Eo*a*abs(tI)*(sqrt(abs(tI)))/((tS*d)^p);

   k5S=h*tdS;
   k5I=h*tdI;
   k5dI=-h*((tI)+(b*tdI)+(a*tdI/(2*tS*sqrt(abs(tI))))-
((a*k*tdS*sqrt(abs(tI)))/(tS^2)));
   k5Is=(h/Ls)*((M*tdI)-(T*Rs*tIs));

   %part 6
   tS=S-(8*k1S/27)+(2*k2S)-(3544*k3S/2565)+(1859*k4S/4104)-
(11*k5S/40);
   tdI=dI-(8*k1dI/27)+(2*k2dI)-(3544*k3dI/2565)+(1859*k4dI/4104)-
(11*k5dI/40);
   tI=I-(8*k1I/27)+(2*k2I)-(3544*k3I/2565)+(1859*k4I/4104)-
(11*k5I/40);
   tIs=Is-(8*k1Is/27)+(2*k2Is)-(3544*k3Is/2565)+(1859*k4Is/4104)-
(11*k5Is/40);

   tdS=q*Eo*a*abs(tI)*(sqrt(abs(tI)))/((tS*d)^p);

   k6S=h*tdS;
   k6I=h*tdI;
   k6dI=-h*((tI)+(b*tdI)+(a*tdI/(2*tS*sqrt(abs(tI))))-
((a*k*tdS*sqrt(abs(tI)))/(tS^2)));
   k6Is=(h/Ls)*((M*tdI)-(T*Rs*tIs));
```

```
   %Yn+1
   torr=torr+h;

   S=real(S+(16*k1S/135)+(6656*k3S/12825)+(28561*k4S/56430)-
(9*k5S/50)+(2*k6S/55));
   dI=real(dI+(16*k1dI/135)+(6656*k3dI/12825)+(28561*k4dI/56430)-
(9*k5dI/50)+(2*k6dI/55));
   I=real(I+(16*k1I/135)+(6656*k3I/12825)+(28561*k4I/56430)-
(9*k5I/50)+(2*k6I/55));
   Is=real(Is+(16*k1Is/135)+(6656*k3Is/12825)+(28561*k4Is/56430)-
(9*k5Is/50)+(2*k6Is/55));

   Error=real((k1Is/360)-(128*k3Is/4275)-
(2197*k4Is/75240)+(k5Is/50)+(2*k6Is/55));

   %blob(n)=100*Error/I;
   if abs(Error)/abs(Is)>1e-9;
      h=h/1.2;
      else h=h*1.2;
      end

   Sigma(n)=(S);
   Cur(n)=((Vo/Zo)*I);
   dCur(n)=((Vo/Lp)*dI);
   Curs(n)=((Vo/Zo)*Is);
   Res(n)=Zo*k*a*(sqrt(abs(I)))/(I*S);
   VL(n)=(Vo*(dI));
   VR(n)=Vo*k*a*(sqrt(abs(I)))/S;
   Vlamp(n)=Vo*(dI+(k*a*(sqrt(abs(I)))/S));
   Tbr(n)=abs((0.8*((Vo/Zo)*I)*(Vo*k*a*(sqrt(abs(I)))/S)/5.67e-
12))^(1/4);

   time(n)=torr*T;

end

n
Rmin

Power=Cur.*VR;
Vrogowski=Curs*Rs;
Vscope=(Rcv/(Rcv+Rwire))*Vrogowski;
%Integrating Rogowski
Curp=Curs*Ls/M;
%Non-Integrating Rogowski
dCurp=Curs*Rs/M;

Elamp(1)=0;
q=1;
while q<n
   time_int=time(q+1)-time(q);
   Elamp(q+1)=Elamp(q)+((Power(q+1)+Power(q))*time_int/2);
   q=q+1;
end


Erel=Elamp/Energy;


   %plot(time,Erel);
   %plot(time,Elamp);

   plot(time,Cur);
   %plot(time,Sigma);
```

```
%plot(time,Cur,time,Vlamp);
%plot(time,dCur);
%plot(time,Res);
%plot(time,VR);
%plot(Cur,VR);
%plot(time,Power);
%plot(time,Tbr);

%plot(time,Vrogowski);
%plot(time,Vscope);
%plot(time,Curp,time,Cur);
%plot(time,dCurp,time,dCur);
%axis ([0 2e-6 0 1]);

grid on
box on

xlabel('time (Seconds)')
ylabel('Predicted lamp Current (Amperes)')
```

Appendix C:

Corona Power Supply Analysis

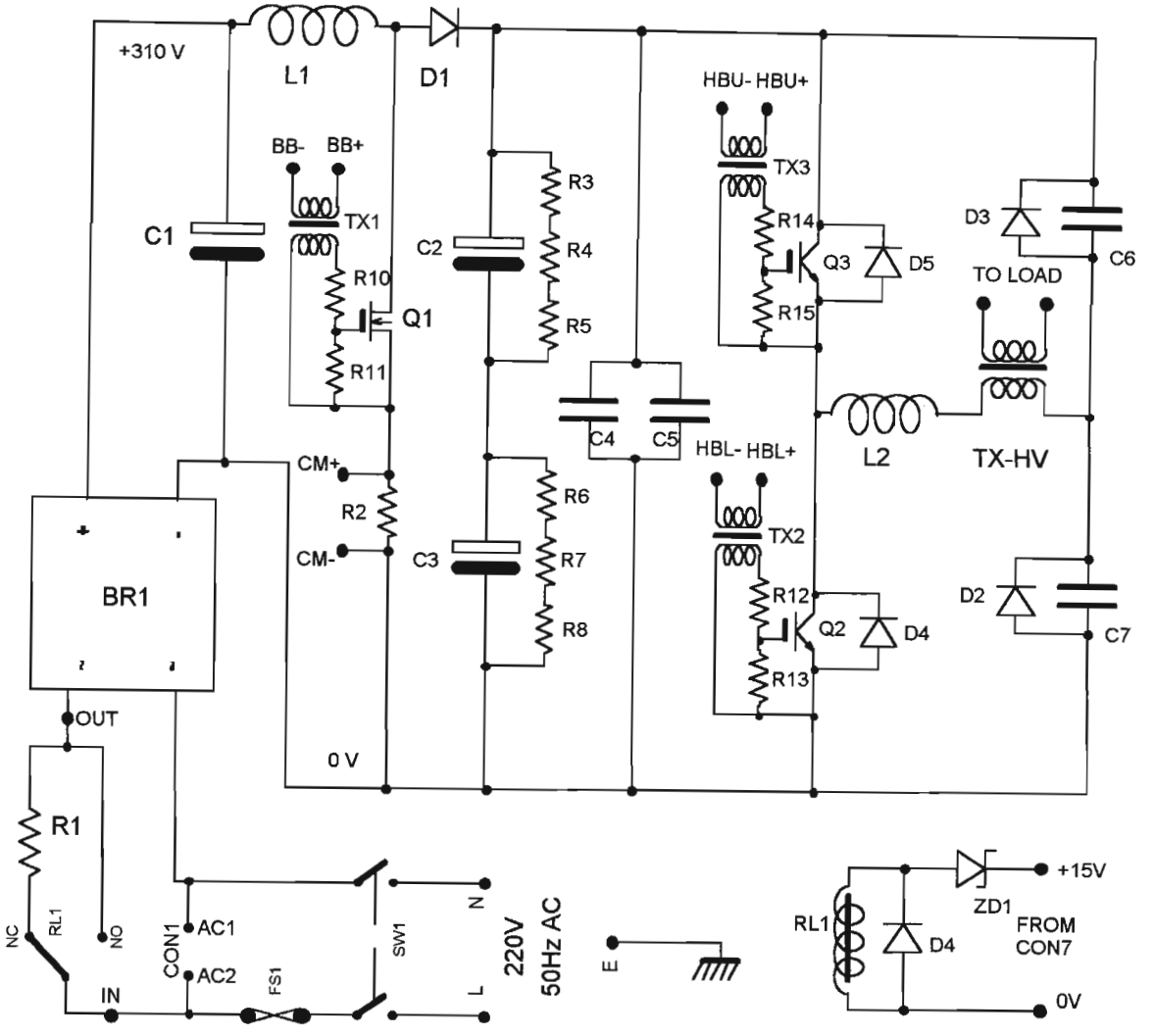

Figure C.1 : The power stage of the high frequency corona discharge current source

Figure C.1 shows a schematic diagram of the power delivery circuit. The corona apparatus, as defined in chapter 5, was attached to the secondary of ferrite transformer *TX-HV*. The design operated as follows:

Mains at nominal 220v RMS is connected to the AC terminals of bridge-rectifier BR_1 via double-pole switch SW_1, fuse FS_1, and the normally open contacts of relay RL_1. Relay RL_1 and resistor R_1 provide the soft-start mechanism required to prevent the sudden current surge as capacitor C_1 charges at switch-on. The positive output of BR_1 is connected to the positive terminal of electrolytic capacitor C_1. Typically 310v

DC (rectified mains) was measured across capacitor C_1, with a degree of ripple as a function of the power drawn by the load. From the +310v positive terminal of capacitor C_1, current is fed to the half bridge circuit via inductor L_1 and diode D_1, where, inductor L_1, diode D_1 and switch Q_1 form a *buck-derived converter*. The buck-derived converter supplies current to the half-bridge at an adjustable voltage between rectified mains potential (+310v) and 450v, as a function of the drive signal switch $Q1$.

The buck-derived converter functions such that when switch Q_1 (a MOSFET) is left in the *off* state, the potential which develops across capacitor C_4, C_5 and the C_2,C_3 pair is near enough identical to that across C_1, since, given that the current drawn is near enough time invariant, no potential can develop across inductor L_1. Note, ~0.6v is dropped across diode D_1. *However*, when switch Q_1 is toggled to the *on* state a current I_{BD} is forced to flow through inductor L_1 according to:

$$\frac{dI_{BD}}{dt} = \frac{V_L}{L} \qquad \textbf{(C.1)}$$

where V_L is simply ~310v (rectified mains voltage). Hence the magnitude of the current through inductive energy store L_1 is controlled as a function of the duration over which switch Q_1 is set into the *on* state. Given that the oscillator on the control circuit is of constant frequency, the duration of the on state during a given cycle is controlled in the usual pulse-width modulated fashion typical of many switching power supplies. The switch current is monitored by measuring the voltage across resistor R_2 placed in series with switch Q_1. When a predefined current is crossed (set according to the control circuit) switch Q_1 is returned to the *off* state until the next cycle of the oscillator begins. Since the current through inductor L_1 can not terminate when switch Q_1 is opened, current I_{BD} is forced to flow through diode D_1 into the half-bridge. Given the load parameters, this current was either drawn away at the same potential, or the voltage across the half-bridge rises until such time as the potential is sufficiently high to <u>cause</u> the delivered current *to be drawn away by the load*. Hence the buck-derived converter is employed to vary the voltage across the half-bridge from rectified mains potential upwards. The maximum voltage on the manufactured unit was limited to 450v DC, but could be increased theoretically if switch Q_1 and inductor L_1 were chosen to carry higher peak currents.

The half-bridge functions such that when switch Q_3 is set into the *on* state, switch Q_2 is set into the *off* state, and visa-versa. With switch Q_3 *on* and C_7 completely discharged (C_6 fully charged) C_7 is caused to charge (and C_6 discharge) as current flows from the positive supply rail through switch Q_3, inductor L_2, and the primary of transformer *TX-HV*. Between discharges the corona load appears at the primary of the transformer as capacitor C_O multiplied by the square of the secondary to primary turns ratio. Consequently inductor L_2 forms a series resonant circuit with the capacitance seen at the primary of the transformer *and* the combined capacitance of C_6 and C_7. To ensure the correct operation of the circuit the magnitude of the combined C_6-C_7 pair is made significantly (<5×) smaller than that seen at the primary of the transformer. Hence, between discharges, the dominant LC transfer occurs between inductor L_2 and the combined C_6-C_7 pair. In a typical LC transfer circuit the peak voltage across the circuit capacitance is twice the supply voltage. However, in the above circuit this is prevented by diode D_3, since diode D_3 clamps the voltage across capacitor C_7 to the supply rail if the voltage across capacitor C_7 should happen to attempt to exceed the supply voltage. Consequently the current flowing through inductor L_2 (at that moment at which diode D_3 clamps capacitor C_7 to the supply rail) has no other alternative other than to dissipate through the transformer into the corona load, causing a visible discharge to form momentarily.

When the energy stored in inductor L_2 has fully dissipated (that is to say that the inductor current had subsided), switch Q_3 is turned off, and switch Q_2 turned on. The circuit operation is then repeat in an identical but opposite manner such that C_7 is discharged while C_6 is charged. Diode D_2 ensures that C_7 (and C_6) are clamped to the zero volt line after C_7 had discharged, and once again inductor L_2 is forced discharge itself through the transformer into the corona load. Each half-cycle of the half-bridge operation is therefore sub-divided into two further sub-cycles; the former to *charge* energy storage inductor L_2, and the latter to *discharge* energy storage inductor L_2, into the corona via transformer *TX-HV*. Switches Q_3 and Q_4 are identical IGBT's.

Figure C.2 shows the corona power supply control circuit. The purpose of the control circuit is to control the switching operation of the power circuit. The control circuit is responsible for ensuring that switches Q_1, Q_2 and Q_3 are switched *on* and *off* at the correct moments in time as a function of control signals fed back to the

control circuit from the power circuit. Only two control signals were employed in this design, namely a temperature signal from the heat-sink to which switch Q_1 was attached, and a voltage representation of the current flowing through transistor Q_1. Due to the self regulating nature of the chosen resonant half-bridge circuit no voltage or current feed-back was employed or ever appeared necessary; even under short circuit and no-load conditions!

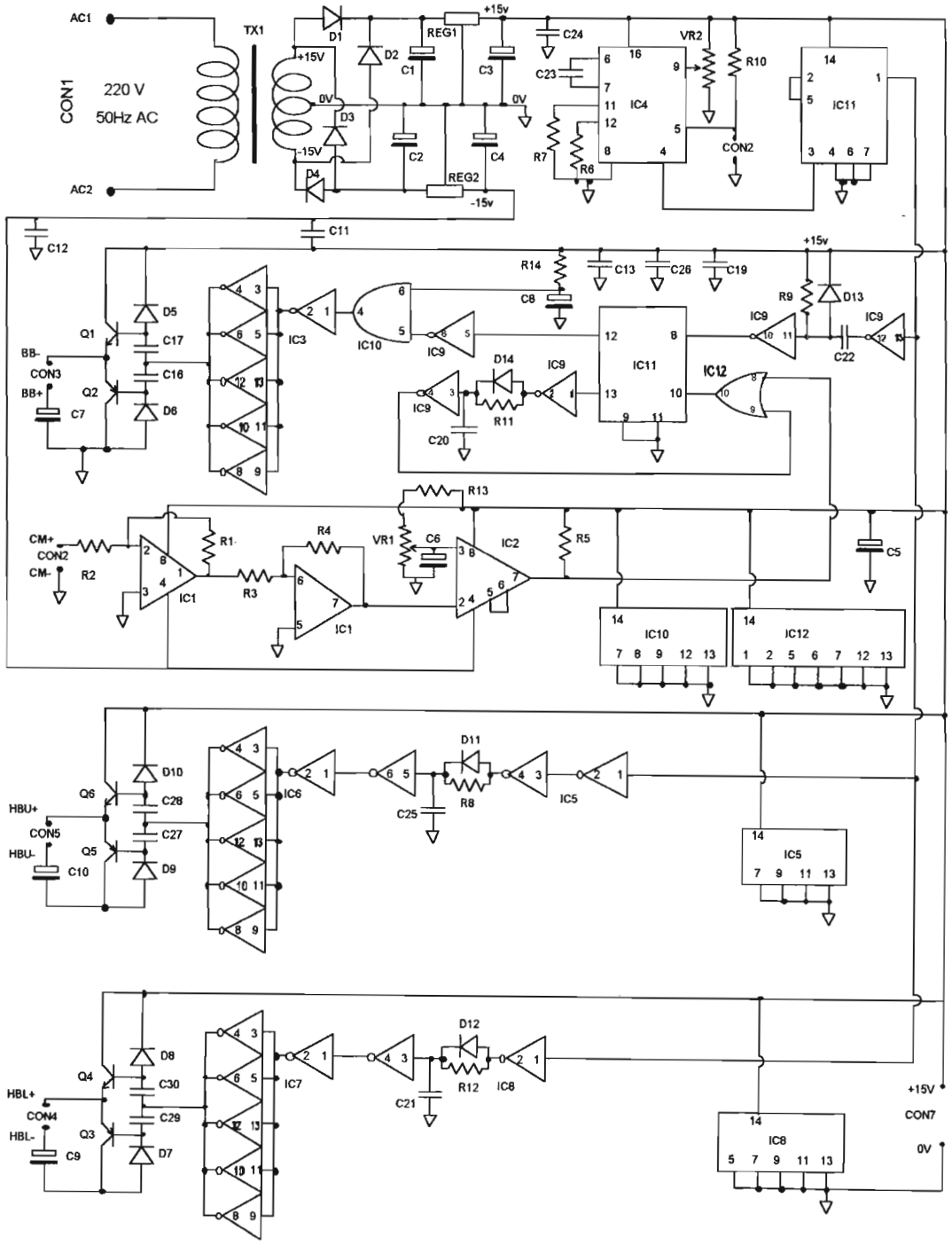

Figure C.2 : The control circuit for the high frequency corona discharge current source

The control circuit operates as follows: Transformer TX_1 steps 220v, 50Hz AC mains from switch SW_1 and fuse FS_1, down to 15V, 50Hz AC. The secondary of transformer TX_1 is centre-tapped. Diodes D_1 to D_4 rectify the output of TX_1. Capacitors C_1 and C_2 ensured a smoothed DC output and REG_1 and REG_2 regulates the smoothed DC to plus and minus 15V DC. The heart of the control circuit is its oscillator IC_4 manufactured from a temperature stabilised Phase-Lock-Loop (PLL). Only the oscillator capability of the PLL is utilised. The frequency of the square-wave output of IC_4 is adjusted by turning preset resistor VR_2 between the frequency limits defined by R_6, R_7 and C_{23}. A normally closed heat-switch SW_2 is fitted to the heat-sink to which Q_1 on the power circuit is attached, and used to disable the oscillator if Q_1 overheats.

To ensure a 50% duty cycle the output of IC_4 is passed through half a D-type flip-flop, IC_{11}. This halves the oscillator frequency but guarantees a 50% duty-cycle. The signal measured at pin 1 of IC_{11} is the control circuit clock signal, and is set to between 15kHz and 25kHz depending on the resonant frequency of the corona load. This clock signal is fed to two halves of the control circuit: That which controls the operation of the buck-derived converter, and that which controls the operation of the half-bridge. Two inverters from IC_9 and R_9, D_{13} and C_{22} are used to pulse the SET input of the remaining flip-flop within IC_{11} when the clock signal toggles from a *low* to *high* state. Hence switch Q_1 is set placed in the *on* state (provided C_8 is charged). R_{14} and C_8 ensure that Q_1 can only be turned on after the control circuit has powered up and the oscillator stabilised, thus preventing the unnecessary destruction of switch Q_1 due to confusion in the control circuit during power-up. Pin 12 of IC_{11} is the NOT-Q output of the flip-flop. It is important to use the NOT-Q output because under the accidental condition of both the SET and RESET inputs are set *high* simultaneously, Q and NOT-Q will <u>both</u> go high, spelling disaster for the buck-derived converter. Hence the NOT-Q output is inverted using another of the inverters within IC_9 in order to regain the Q state. This is then AND'ed to the state of C_8 in order to drive IC_3, a hex-Schmidt-inverter. IC_3 and the remaining components between IC_3 and CON_3 are for the purpose of driving the isolating transformer TX_1 on the power circuit board. Hence, under normal operating conditions, when the clock signal changes from the low state to the high state, switch Q_1 on the power circuit toggles from the off state to the on state.

The operation of the buck-derived converter control circuit is a function of the current through switch Q_1 by virtue of the voltage which develops across resistor R_2 (100mV/A). Op-Amp IC_1 amplifies the voltage across resistor R_2 and compares it to the voltage across preset resistor VR_1. When the output of Op-Amp IC_1 exceeds the preset value the output of the comparitor goes *high*. The flip-flop is therefore reset and switch Q_1 is turned off. To ensure that the flip-flop output Q cannot be set high indefinitely, two inverters from IC_9 and R_{11}, D_{14} and C_{20} are employed to pulse the RESET input of the flip-flop. Hence, under normal operating conditions, switch Q_1 on the power circuit is toggled from the on state to the off state when the current level defined by preset resistor VR_1 has been exceeded, or, when the time period defined by R_{11} and C_{20} has elapsed.

Finally, the clock signal is used to drive switches Q_2 and Q_3 via a similar inverter and transistor drive circuit used to drive switch Q_1. However, in order to introduce the required amount of dead-time between the switching *off* of one switch and the switching *on* of the other, two inverters, a diode, resistor and capacitor are employed in each respective half of the drive circuitry. These components are of course identical in order to ensure that each switch element experiences identical dead-time.

Appendix D :

```
%------------------%
%-- CORONA MODEL --%
%------------------%

%Model to determine performance of Corona PSU

clear all;

%BASIC CIRCUIT COMPONENTS:
Vsupply=380;        %supply voltage in units of Volts
Al_s=270e-9;        %Al value of series inductor core
n_s=40;             %Number of turns on series inductor
Lo=(n_s^2)*Al_s     %Resonant inductance in units of Henries
Rp=0.1;             %primary resistance in units of ohms
Rs=6.2;             %secondary resistance in units of ohms
Cp=2*68e-9;         %Resonant primary capacitor


%TRANSFORMER:
Nc=1;               %Number of transformer core pairs
Le=354e-3;          %magnetic path length in units of m
Ae=Nc*840e-6;       %magnetic area in units of m^2

Ngap=0;             %number of air gaps
Lgap=0;             %air gap path length in units of m
Kfe=1.5;            %Flux expansion co-efficient at each air gap

MUi=1750;           %initial relative permeability
MUe=(Le*MUi)/(Le+((Ngap*Lgap*MUi)/Kfe))
                    %Effective permeability with air gap
AL=4*pi*1e-7*MUe/(Le/Ae)
                    %inductance per turn^2 in Henries
N=12;               %ns/np
np=20;              %number of primary turns
ns=N*np;            %number of secondary turns
Lp=(np^2)*AL;       %primary magnetising inductance in Henries
Ls=(ns^2)*AL;       %secondary de-magnetising inductance in Henries
kc=1.00;            %Coupling coefficient
M=kc*sqrt(Lp*Ls);   %mutual inductance in Henries


%NON-LINEAR CAPACITIVE-CORONA LOAD:
Nb=2;               %Number of dielectric boards
eps=5*8.854e-12;    %dielectric constant in Farads per metre
d=0.00063;          %thickness of dielectric in metres
Ac=0.1*0.15;        %area of dielectric in metres^2
Cb=Nb*Ac*eps/d;     %final capacitance of load in Farads
Co=(300/500)*Cb     %initial capacitance of load
Cg=(500/500)*Cb     %Remaining capacitance of load
Rg=200/Nb;          %Corona resistance in ohms
Vion=2000;          %Corona potential


%INITIAL VALUES
CurP(1)=0;
CurS(1)=0;
CurL(1)=0;
Power(1)=0;
Energy(1)=0;
E_prim(1)=0;
E_seco(1)=0;
E_load(1)=0;
```

```
Ip=0;
Is=0;
Il=0;
Ipeak=0;
Vcp=0;
Vco=Vion+((5*Vsupply)-900);
%Vco=0;
Vcg=-((5*Vsupply)-900);
%Vcg=0;
Vg=-Vion;
%Vg=0;

k_cp=1;
k_vg=-1;

error_margin=1e-13;
n=2;

T=0;
Interval=5e-6;
h=Interval/5000;
check=0;

count=0;
while count<4;
   COR_macro;
   count=count+1
end

VolCg=VolCo-((CurL.*Rg)+(VolG));


%plot(time,Vp);
%plot(time,Vs);

%plot(time,CurP);
%plot(time,CurS);
%plot(time,CurL);

plot(time,10*CurP,time,Vp);

%plot(time,-10*CurS,time,10*CurL,time,VolCo/1000);

plot(time,CurP,time,2*VolCo/1000);

%plot(time,VolCp,time,10*CurP);
%plot(time,VolCg)
%plot(time,FluxDen);
%plot(time,VolCo,time,VolG);
%plot(time,VolG,time,((CurS+CurL)/(1e6*Co)))
%plot(time,(VolCo-VolCg))

grid on;
box on;

time(n-1);
```

```
%---------------------%
% ---- COR_macro  ----%
%---------------------%

subroutine, as used in the above model ---- %

k_cp=1;
k_vg=-1;

Vo=Vsupply;

while Ip>=0;

   %part 1
   tIp=Ip;
   tIs=Is;
   tIl=Il;
   tVcp=Vcp;
   tVco=Vco;
   tVcg=Vcg;

   tdVcp=k_cp*tIp/Cp;
   tdVco=(tIs+tIl)/Co;
   tdVcg=tIl/Cg;
   tdVg=k_vg*tdVco;

   tdIl=(-1/Rg)*(tdVco+tdVcg+tdVg);
   tdIp=(1/(Lp+Lo-((M^2)/Ls)))*(Vo+((M/Ls)*(tVco+(Rs*tIs)))-(Rp*tIp)-
tVcp);
   tdIs=(-1/Ls)*((Rs*tIs)+(M*tdIp)+tVco);

   k1Ip=h*tdIp;
   k1Is=h*tdIs;
   k1Il=h*tdIl;
   k1Vcp=h*tdVcp;
   k1Vco=h*tdVco;
   k1Vcg=h*tdVcg;
   k1Vg=h*tdVg;

   %part 2
   tIp=Ip+(k1Ip/4);
   tIs=Is+(k1Is/4);
   tIl=Il+(k1Il/4);
   tVcp=Vcp+(k1Vcp/4);
   tVco=Vco+(k1Vco/4);
   tVcg=Vcg+(k1Vcg/4);

   tdVcp=k_cp*tIp/Cp;
   tdVco=(tIs+tIl)/Co;
   tdVcg=tIl/Cg;
   tdVg=k_vg*tdVco;

   tdIl=(-1/Rg)*(tdVco+tdVcg+tdVg);
   tdIp=(1/(Lp+Lo-((M^2)/Ls)))*(Vo+((M/Ls)*(tVco+(Rs*tIs)))-(Rp*tIp)-
tVcp);
   tdIs=(-1/Ls)*((Rs*tIs)+(M*tdIp)+tVco);

   k2Ip=h*tdIp;
   k2Is=h*tdIs;
   k2Il=h*tdIl;
   k2Vcp=h*tdVcp;
   k2Vco=h*tdVco;
   k2Vcg=h*tdVcg;
   k2Vg=h*tdVg;
```

```
   %part 3
   tIp=Ip+(3*k1Ip/32)+(9*k2Ip/32);
   tIs=Is+(3*k1Is/32)+(9*k2Is/32);
   tIl=Il+(3*k1Il/32)+(9*k2Il/32);
   tVcp=Vcp+(3*k1Vcp/32)+(9*k2Vcp/32);
   tVco=Vco+(3*k1Vco/32)+(9*k2Vco/32);
   tVcg=Vcg+(3*k1Vcg/32)+(9*k2Vcg/32);

   tdVcp=k_cp*tIp/Cp;
   tdVco=(tIs+tIl)/Co;
   tdVcg=tIl/Cg;
   tdVg=k_vg*tdVco;

   tdIl=(-1/Rg)*(tdVco+tdVcg+tdVg);
   tdIp=(1/(Lp+Lo-((M^2)/Ls)))*(Vo+((M/Ls)*(tVco+(Rs*tIs)))-(Rp*tIp)-
tVcp);
   tdIs=(-1/Ls)*((Rs*tIs)+(M*tdIp)+tVco);

   k3Ip=h*tdIp;
   k3Is=h*tdIs;
   k3Il=h*tdIl;
   k3Vcp=h*tdVcp;
   k3Vco=h*tdVco;
   k3Vcg=h*tdVcg;
   k3Vg=h*tdVg;

   %part 4
   tIp=Ip+(1932*k1Ip/2197)-(7200*k2Ip/2197)+(7296*k3Ip/2197);
   tIs=Is+(1932*k1Is/2197)-(7200*k2Is/2197)+(7296*k3Is/2197);
   tIl=Il+(1932*k1Il/2197)-(7200*k2Il/2197)+(7296*k3Il/2197);
   tVcp=Vcp+(1932*k1Vcp/2197)-(7200*k2Vcp/2197)+(7296*k3Vcp/2197);
   tVco=Vco+(1932*k1Vco/2197)-(7200*k2Vco/2197)+(7296*k3Vco/2197);
   tVcg=Vcg+(1932*k1Vcg/2197)-(7200*k2Vcg/2197)+(7296*k3Vcg/2197);

   tdVcp=k_cp*tIp/Cp;
   tdVco=(tIs+tIl)/Co;
   tdVcg=tIl/Cg;
   tdVg=k_vg*tdVco;

   tdIl=(-1/Rg)*(tdVco+tdVcg+tdVg);
   tdIp=(1/(Lp+Lo-((M^2)/Ls)))*(Vo+((M/Ls)*(tVco+(Rs*tIs)))-(Rp*tIp)-
tVcp);
   tdIs=(-1/Ls)*((Rs*tIs)+(M*tdIp)+tVco);

   k4Ip=h*tdIp;
   k4Is=h*tdIs;
   k4Il=h*tdIl;
   k4Vcp=h*tdVcp;
   k4Vco=h*tdVco;
   k4Vcg=h*tdVcg;
   k4Vg=h*tdVg;

   %part 5
   tIp=Ip+(439*k1Ip/216)-(8*k2Ip)+(3680*k3Ip/513)-(845*k4Ip/4104);
   tIs=Is+(439*k1Is/216)-(8*k2Is)+(3680*k3Is/513)-(845*k4Is/4104);
   tIl=Il+(439*k1Il/216)-(8*k2Il)+(3680*k3Il/513)-(845*k4Il/4104);
   tVcp=Vcp+(439*k1Vcp/216)-(8*k2Vcp)+(3680*k3Vcp/513)-
(845*k4Vcp/4104);
   tVco=Vco+(439*k1Vco/216)-(8*k2Vco)+(3680*k3Vco/513)-
(845*k4Vco/4104);
   tVcg=Vcg+(439*k1Vcg/216)-(8*k2Vcg)+(3680*k3Vcg/513)-
(845*k4Vcg/4104);

   tdVcp=k_cp*tIp/Cp;
```

```
   tdVco=(tIs+tIl)/Co;
   tdVcg=tIl/Cg;
   tdVg=k_vg*tdVco;

   tdIl=(-1/Rg)*(tdVco+tdVcg+tdVg);
   tdIp=(1/(Lp+Lo-((M^2)/Ls)))*(Vo+((M/Ls)*(tVco+(Rs*tIs)))-(Rp*tIp)-
tVcp);
   tdIs=(-1/Ls)*((Rs*tIs)+(M*tdIp)+tVco);
   k5Ip=h*tdIp;
   k5Is=h*tdIs;
   k5Il=h*tdIl;
   k5Vcp=h*tdVcp;
   k5Vco=h*tdVco;
   k5Vcg=h*tdVcg;
   k5Vg=h*tdVg;

   %part 6
   tIp=Ip-(8*k1Ip/27)+(2*k2Ip)-(3544*k3Ip/2565)+(1859*k4Ip/4104)-
(11*k5Ip/40);
   tIs=Is-(8*k1Is/27)+(2*k2Is)-(3544*k3Is/2565)+(1859*k4Is/4104)-
(11*k5Is/40);
   tIl=Il-(8*k1Il/27)+(2*k2Il)-(3544*k3Il/2565)+(1859*k4Il/4104)-
(11*k5Il/40);
   tVcp=Vcp-(8*k1Vcp/27)+(2*k2Vcp)-
(3544*k3Vcp/2565)+(1859*k4Vcp/4104)-(11*k5Vcp/40);
   tVco=Vco-(8*k1Vco/27)+(2*k2Vco)-
(3544*k3Vco/2565)+(1859*k4Vco/4104)-(11*k5Vco/40);
   tVcg=Vcg-(8*k1Vcg/27)+(2*k2Vcg)-
(3544*k3Vcg/2565)+(1859*k4Vcg/4104)-(11*k5Vcg/40);

   tdVcp=k_cp*tIp/Cp;
   tdVco=(tIs+tIl)/Co;
   tdVcg=tIl/Cg;
   tdVg=k_vg*tdVco;

   tdIl=(-1/Rg)*(tdVco+tdVcg+tdVg);
   tdIp=(1/(Lp+Lo-((M^2)/Ls)))*(Vo+((M/Ls)*(tVco+(Rs*tIs)))-(Rp*tIp)-
tVcp);
   tdIs=(-1/Ls)*((Rs*tIs)+(M*tdIp)+tVco);

   k6Ip=h*tdIp;
   k6Is=h*tdIs;
   k6Il=h*tdIl;
   k6Vcp=h*tdVcp;
   k6Vco=h*tdVco;
   k6Vcg=h*tdVcg;
   k6Vg=h*tdVg;

   %Yn+1
   Ip=(Ip+(16*k1Ip/135)+(6656*k3Ip/12825)+(28561*k4Ip/56430)-
(9*k5Ip/50)+(2*k6Ip/55));
   Is=(Is+(16*k1Is/135)+(6656*k3Is/12825)+(28561*k4Is/56430)-
(9*k5Is/50)+(2*k6Is/55));
   Il=(Il+(16*k1Il/135)+(6656*k3Il/12825)+(28561*k4Il/56430)-
(9*k5Il/50)+(2*k6Il/55));
   Vcp=(Vcp+(16*k1Vcp/135)+(6656*k3Vcp/12825)+(28561*k4Vcp/56430)-
(9*k5Vcp/50)+(2*k6Vcp/55));
   Vco=(Vco+(16*k1Vco/135)+(6656*k3Vco/12825)+(28561*k4Vco/56430)-
(9*k5Vco/50)+(2*k6Vco/55));
   Vcg=(Vcg+(16*k1Vcg/135)+(6656*k3Vcg/12825)+(28561*k4Vcg/56430)-
(9*k5Vcg/50)+(2*k6Vcg/55));
   Vg=(Vg+(16*k1Vg/135)+(6656*k3Vg/12825)+(28561*k4Vg/56430)-
(9*k5Vg/50)+(2*k6Vg/55));
```

```
   Error1=((k1Ip/360)-(128*k3Ip/4275)-
(2197*k4Ip/75240)+(k5Ip/50)+(2*k6Ip/55));
   Error2=((k1Vcp/360)-(128*k3Vcp/4275)-
(2197*k4Vcp/75240)+(k5Vcp/50)+(2*k6Vcp/55));

   CurP(n)=Ip;
   CurS(n)=Is;
   CurL(n)=Il;
   VolCp(n)=Vcp;
   VolCo(n)=-Vco;
   VolL(n)=Vcg;
   VolG(n)=Vg;
   FluxDen(n)=(1/(Ae*np))*((Lp*Ip)+(M*Is));

   dIp=((CurP(n)-CurP(n-1))/h);
   dIs=((CurS(n)-CurS(n-1))/h);

   Vp(n)=(Lp*dIp)+(M*dIs);
   Vs(n)=(Ls*dIs)+(M*dIp);

   Power(n)=Ip*(((Lp*dIp)+(M*dIs))+(Ip*Rp));
   Energy(n)=(Energy(n-1))+((h/2)*(Power(n)+Power(n-1)));
   PowAv(n)=Energy(n)/T;

   time(n)=T;
   T=T+h;

   if Vcp>=Vo
      k_cp=0;
   end

   if (abs(-Vco-Vcg))>=Vion
      k_vg=0;
   end

   if -Vco<0
      if (-(Is+Il)/Co)>=0
         k_vg=-1;
      end
   end

   if -Vco>0
      if (-(Is+Il)/Co)<=0
         k_vg=-1;
      end
   end
   if (CurP(n)*CurP(n-1))<0
      check=check+1;
   end
   n=n+1;

   if abs(Error1)/abs(Ip)>error_margin;
      h=h/1.2;
      else h=h*1.2;
      end
   if abs(Error2)/abs(Vcp)>error_margin;
      h=h/1.2;
      else h=h*1.2;
      end

   end
```

```
%PART TWO:
k_cp=1;
k_vg=-1;
Vo=0;

while Ip<=0;
   %part 1
   tIp=Ip;
   tIs=Is;
   tIl=Il;
   tVcp=Vcp;
   tVco=Vco;
   tVcg=Vcg;

   tdVcp=k_cp*tIp/Cp;
   tdVco=(tIs+tIl)/Co;
   tdVcg=tIl/Cg;
   tdVg=k_vg*tdVco;

   tdIl=(-1/Rg)*(tdVco+tdVcg+tdVg);
   tdIp=(1/(Lp+Lo-((M^2)/Ls)))*(Vo+((M/Ls)*(tVco+(Rs*tIs)))-(Rp*tIp)-
tVcp);
   tdIs=(-1/Ls)*((Rs*tIs)+(M*tdIp)+tVco);

   k1Ip=h*tdIp;
   k1Is=h*tdIs;
   k1Il=h*tdIl;
   k1Vcp=h*tdVcp;
   k1Vco=h*tdVco;
   k1Vcg=h*tdVcg;
   k1Vg=h*tdVg;

   %part 2
   tIp=Ip+(k1Ip/4);
   tIs=Is+(k1Is/4);
   tIl=Il+(k1Il/4);
   tVcp=Vcp+(k1Vcp/4);
   tVco=Vco+(k1Vco/4);
   tVcg=Vcg+(k1Vcg/4);

   tdVcp=k_cp*tIp/Cp;
   tdVco=(tIs+tIl)/Co;
   tdVcg=tIl/Cg;
   tdVg=k_vg*tdVco;

   tdIl=(-1/Rg)*(tdVco+tdVcg+tdVg);
   tdIp=(1/(Lp+Lo-((M^2)/Ls)))*(Vo+((M/Ls)*(tVco+(Rs*tIs)))-(Rp*tIp)-
tVcp);
   tdIs=(-1/Ls)*((Rs*tIs)+(M*tdIp)+tVco);

   k2Ip=h*tdIp;
   k2Is=h*tdIs;
   k2Il=h*tdIl;
   k2Vcp=h*tdVcp;
   k2Vco=h*tdVco;
   k2Vcg=h*tdVcg;
   k2Vg=h*tdVg;

   %part 3
   tIp=Ip+(3*k1Ip/32)+(9*k2Ip/32);
   tIs=Is+(3*k1Is/32)+(9*k2Is/32);
   tIl=Il+(3*k1Il/32)+(9*k2Il/32);
   tVcp=Vcp+(3*k1Vcp/32)+(9*k2Vcp/32);
   tVco=Vco+(3*k1Vco/32)+(9*k2Vco/32);
```

```
   tVcg=Vcg+(3*k1Vcg/32)+(9*k2Vcg/32);

   tdVcp=k_cp*tIp/Cp;
   tdVco=(tIs+tIl)/Co;
   tdVcg=tIl/Cg;
   tdVg=k_vg*tdVco;

   tdIl=(-1/Rg)*(tdVco+tdVcg+tdVg);
   tdIp=(1/(Lp+Lo-((M^2)/Ls)))*(Vo+((M/Ls)*(tVco+(Rs*tIs)))-(Rp*tIp)-
tVcp);
   tdIs=(-1/Ls)*((Rs*tIs)+(M*tdIp)+tVco);

   k3Ip=h*tdIp;
   k3Is=h*tdIs;
   k3Il=h*tdIl;
   k3Vcp=h*tdVcp;
   k3Vco=h*tdVco;
   k3Vcg=h*tdVcg;
   k3Vg=h*tdVg;

   %part 4
   tIp=Ip+(1932*k1Ip/2197)-(7200*k2Ip/2197)+(7296*k3Ip/2197);
   tIs=Is+(1932*k1Is/2197)-(7200*k2Is/2197)+(7296*k3Is/2197);
   tIl=Il+(1932*k1Il/2197)-(7200*k2Il/2197)+(7296*k3Il/2197);
   tVcp=Vcp+(1932*k1Vcp/2197)-(7200*k2Vcp/2197)+(7296*k3Vcp/2197);
   tVco=Vco+(1932*k1Vco/2197)-(7200*k2Vco/2197)+(7296*k3Vco/2197);
   tVcg=Vcg+(1932*k1Vcg/2197)-(7200*k2Vcg/2197)+(7296*k3Vcg/2197);

   tdVcp=k_cp*tIp/Cp;
   tdVco=(tIs+tIl)/Co;
   tdVcg=tIl/Cg;
   tdVg=k_vg*tdVco;

   tdIl=(-1/Rg)*(tdVco+tdVcg+tdVg);
   tdIp=(1/(Lp+Lo-((M^2)/Ls)))*(Vo+((M/Ls)*(tVco+(Rs*tIs)))-(Rp*tIp)-
tVcp);
   tdIs=(-1/Ls)*((Rs*tIs)+(M*tdIp)+tVco);

   k4Ip=h*tdIp;
   k4Is=h*tdIs;
   k4Il=h*tdIl;
   k4Vcp=h*tdVcp;
   k4Vco=h*tdVco;
   k4Vcg=h*tdVcg;
   k4Vg=h*tdVg;

   %part 5
   tIp=Ip+(439*k1Ip/216)-(8*k2Ip)+(3680*k3Ip/513)-(845*k4Ip/4104);
   tIs=Is+(439*k1Is/216)-(8*k2Is)+(3680*k3Is/513)-(845*k4Is/4104);
   tIl=Il+(439*k1Il/216)-(8*k2Il)+(3680*k3Il/513)-(845*k4Il/4104);
   tVcp=Vcp+(439*k1Vcp/216)-(8*k2Vcp)+(3680*k3Vcp/513)-
(845*k4Vcp/4104);
   tVco=Vco+(439*k1Vco/216)-(8*k2Vco)+(3680*k3Vco/513)-
(845*k4Vco/4104);
   tVcg=Vcg+(439*k1Vcg/216)-(8*k2Vcg)+(3680*k3Vcg/513)-
(845*k4Vcg/4104);

   tdVcp=k_cp*tIp/Cp;
   tdVco=(tIs+tIl)/Co;
   tdVcg=tIl/Cg;
   tdVg=k_vg*tdVco;

   tdIl=(-1/Rg)*(tdVco+tdVcg+tdVg);
```

```
   tdIp=(1/(Lp+Lo-((M^2)/Ls)))*(Vo+((M/Ls)*(tVco+(Rs*tIs)))-(Rp*tIp)-
tVcp);
   tdIs=(-1/Ls)*((Rs*tIs)+(M*tdIp)+tVco);
   k5Ip=h*tdIp;
   k5Is=h*tdIs;
   k5Il=h*tdIl;
   k5Vcp=h*tdVcp;
   k5Vco=h*tdVco;
   k5Vcg=h*tdVcg;
   k5Vg=h*tdVg;

   %part 6
   tIp=Ip-(8*k1Ip/27)+(2*k2Ip)-(3544*k3Ip/2565)+(1859*k4Ip/4104)-
(11*k5Ip/40);
   tIs=Is-(8*k1Is/27)+(2*k2Is)-(3544*k3Is/2565)+(1859*k4Is/4104)-
(11*k5Is/40);
   tIl=Il-(8*k1Il/27)+(2*k2Il)-(3544*k3Il/2565)+(1859*k4Il/4104)-
(11*k5Il/40);
   tVcp=Vcp-(8*k1Vcp/27)+(2*k2Vcp)-
(3544*k3Vcp/2565)+(1859*k4Vcp/4104)-(11*k5Vcp/40);
   tVco=Vco-(8*k1Vco/27)+(2*k2Vco)-
(3544*k3Vco/2565)+(1859*k4Vco/4104)-(11*k5Vco/40);
   tVcg=Vcg-(8*k1Vcg/27)+(2*k2Vcg)-
(3544*k3Vcg/2565)+(1859*k4Vcg/4104)-(11*k5Vcg/40);

   tdVcp=k_cp*tIp/Cp;
   tdVco=(tIs+tIl)/Co;
   tdVcg=tIl/Cg;
   tdVg=k_vg*tdVco;

   tdIl=(-1/Rg)*(tdVco+tdVcg+tdVg);
   tdIp=(1/(Lp+Lo-((M^2)/Ls)))*(Vo+((M/Ls)*(tVco+(Rs*tIs)))-(Rp*tIp)-
tVcp);
   tdIs=(-1/Ls)*((Rs*tIs)+(M*tdIp)+tVco);

   k6Ip=h*tdIp;
   k6Is=h*tdIs;
   k6Il=h*tdIl;
   k6Vcp=h*tdVcp;
   k6Vco=h*tdVco;
   k6Vcg=h*tdVcg;
   k6Vg=h*tdVg;

   %Yn+1
   Ip=(Ip+(16*k1Ip/135)+(6656*k3Ip/12825)+(28561*k4Ip/56430)-
(9*k5Ip/50)+(2*k6Ip/55));
   Is=(Is+(16*k1Is/135)+(6656*k3Is/12825)+(28561*k4Is/56430)-
(9*k5Is/50)+(2*k6Is/55));
   Il=(Il+(16*k1Il/135)+(6656*k3Il/12825)+(28561*k4Il/56430)-
(9*k5Il/50)+(2*k6Il/55));
   Vcp=(Vcp+(16*k1Vcp/135)+(6656*k3Vcp/12825)+(28561*k4Vcp/56430)-
(9*k5Vcp/50)+(2*k6Vcp/55));
   Vco=(Vco+(16*k1Vco/135)+(6656*k3Vco/12825)+(28561*k4Vco/56430)-
(9*k5Vco/50)+(2*k6Vco/55));
   Vcg=(Vcg+(16*k1Vcg/135)+(6656*k3Vcg/12825)+(28561*k4Vcg/56430)-
(9*k5Vcg/50)+(2*k6Vcg/55));
   Vg=(Vg+(16*k1Vg/135)+(6656*k3Vg/12825)+(28561*k4Vg/56430)-
(9*k5Vg/50)+(2*k6Vg/55));

   Error1=((k1Ip/360)-(128*k3Ip/4275)-
(2197*k4Ip/75240)+(k5Ip/50)+(2*k6Ip/55));
   Error2=((k1Vcp/360)-(128*k3Vcp/4275)-
(2197*k4Vcp/75240)+(k5Vcp/50)+(2*k6Vcp/55));
```

```
    CurP(n)=Ip;
    CurS(n)=Is;
    CurL(n)=Il;
    VolCp(n)=Vcp;
    VolCo(n)=-Vco;
    VolL(n)=Vcg;
    VolG(n)=Vg;
    FluxDen(n)=(1/(Ae*np))*((Lp*Ip)+(M*Is));

    dIp=((CurP(n)-CurP(n-1))/h);
    dIs=((CurS(n)-CurS(n-1))/h);

    Vp(n)=(Lp*dIp)+(M*dIs);
    Vs(n)=(Ls*dIs)+(M*dIp);

    Power(n)=Ip*(((Lp*dIp)+(M*dIs))+(Ip*Rp));
    Energy(n)=(Energy(n-1))+((h/2)*(Power(n)+Power(n-1)));
    PowAv(n)=Energy(n)/T;

    time(n)=T;
    T=T+h;

    if Vcp<=Vo
       k_cp=0;
    end

    if (abs(-Vco-Vcg))>=Vion
       k_vg=0;
    end

    if -Vco>0
       if (-(Is+Il)/Co)<=0
          k_vg=-1;
       end
    end

    if -Vco<0
       if (-(Is+Il)/Co)>=0
          k_vg=-1;
       end
    end

    if (CurP(n)*CurP(n-1))<0
       check=check+1;
    end

    n=n+1;

    if abs(Error1)/abs(Ip)>error_margin;
       h=h/1.2;
       else h=h*1.2;
    end

    if abs(Error2)/abs(Vcp)>error_margin;
       h=h/1.2;
       else h=h*1.2;
    end
end
```

Appendix E:

```
%---------------%
%-- POS Model --%
%---------------%

%This model calls on the routine "POS_macro" to calculate the sheath
%potential "Us", And the sheath length "lp".

%Note: This model is relativistic and includes the Lorentz
%transforms.

echo off;
clear all;

%CIRCUIT PARAMETERS:
Vo=35e3;                %Voltage to which capacitor Co is charged in
Volts
Ro=0.01;                %Pre-PEOS circuit resistance in ohms
Lo=120e-9;              %Pre-PEOS inductance in Henries
Co=2.8e-6;              %Capacitance of storage capacitor in Farads
Ll=100e-9;              %Load inductance
Rl=0.01;                %Load resistance

%PLASMA PARAMETERS:
Z=2;                    %Predominant charge state of plasma
ni=7e18;                %Number of ions per m^3
vd=5.5e4;               %radial velocity of plasma in m/S
mi=20e-27;              %ion mass in kg

%POS DIMENSIONS:
lc=70e-3;               %cathode length metres
rc=10e-3;               %Cathode radius in metres

%CONSTANTS
qe=1.6e-19;             %Electron charge in Coulombs
me=9.11e-31;            %Electron mass in kg
mu=4e-7*pi;             %Permeability of free space
epl=8.854e-12;          %Permittivity of free space
C=3e8;                  %Speed of light


Ic=2*pi*rc*lc*ni*vd*Z*qe*sqrt(mi/(Z*me));
                        %Critical current above which the sheath
forms.

nn=1;
tt=0;
ttime(nn)=tt;

hh=1e-12;
error_ping=1e-11;

Ig=0;                   %Initial generator current
Uc=Vo;                  %Initial capacitor voltage
Il=0;                   %Initial load current
tUs=0;                  %Initial sheath voltage
```

```
%------------%
%-- PART 1 --%
%------------%

%while t<1e-5   %duration over which calculation is performed
while Ig<Ic;

   tock=0;

   %part 1
   tIg=Ig;
   tUc=Uc;

   k1Ig=(hh/Lo)*(tUc-(Ro*tIg));
   k1Uc=-hh*tIg/Co;

   %part 2
   tIg=Ig+(k1Ig/4);
   tUc=Uc+(k1Uc/4);

   k2Ig=(hh/Lo)*(tUc-(Ro*tIg));
   k2Uc=-hh*tIg/Co;

   %part 3
   tIg=Ig+(3*k1Ig/32)+(9*k2Ig/32);
   tUc=Uc+(3*k1Uc/32)+(9*k2Uc/32);

   k3Ig=(hh/Lo)*(tUc-(Ro*tIg));
   k3Uc=-hh*tIg/Co;

   %part 4
   tIg=Ig+(1932*k1Ig/2197)-(7200*k2Ig/2197)+(7296*k3Ig/2197);
   tUc=Uc+(1932*k1Uc/2197)-(7200*k2Uc/2197)+(7296*k3Uc/2197);

   k4Ig=(hh/Lo)*(tUc-(Ro*tIg));
   k4Uc=-hh*tIg/Co;

   %part 5
   tIg=Ig+(439*k1Ig/216)-(8*k2Ig)+(3680*k3Ig/513)-(845*k4Ig/4104);
   tUc=Uc+(439*k1Uc/216)-(8*k2Uc)+(3680*k3Uc/513)-(845*k4Uc/4104);

   k5Ig=(hh/Lo)*(tUc-(Ro*tIg));
   k5Uc=-hh*tIg/Co;

   %part 6
   tIg=Ig-(8*k1Ig/27)+(2*k2Ig)-(3544*k3Ig/2565)+(1859*k4Ig/4104)-
(11*k5Ig/40);
   tUc=Uc-(8*k1Uc/27)+(2*k2Uc)-(3544*k3Uc/2565)+(1859*k4Uc/4104)-
(11*k5Uc/40);

   k6Ig=(hh/Lo)*(tUc-(Ro*tIg));
   k6Uc=-hh*tIg/Co;

   %Yn+1
   Ig_old=Ig;
   Uc_old=Uc;

   Ig=Ig+(16*k1Ig/135)+(6656*k3Ig/12825)+(28561*k4Ig/56430)-
(9*k5Ig/50)+(2*k6Ig/55);
   Uc=Uc+(16*k1Uc/135)+(6656*k3Uc/12825)+(28561*k4Uc/56430)-
(9*k5Uc/50)+(2*k6Uc/55);

   Ping1=(k1Ig/360)-(128*k3Ig/4275)-
(2197*k4Ig/75240)+(k5Ig/50)+(2*k6Ig/55);
```

```
   Ping2=(k1Uc/360)-(128*k3Uc/4275)-
(2197*k4Uc/75240)+(k5Uc/50)+(2*k6Uc/55);

   if abs(Ping1)/abs(Ig)>error_ping;
      tock=1;
   end

   if abs(Ping2)/abs(Uc)>error_ping;
      tock=1;
   end

   if tock==1;
      Ig=Ig_old;
      Uc=Uc_old;
      hh=hh/1.02;
   end

   if tock==0;
      hh=hh*1.02;

      CurG(nn)=Ig;
      VolC(nn)=Uc;

      ttime(nn)=tt;
      tt=tt+hh;
      nn=nn+1;
   end


end
nn

%------------%
%-- PART 2 --%
%------------%

Ig=Ic;
Il=0;
hh=1e-9;
error_ping=1e-5;

while tt<280e-9
%while nn<440;

   tock=0;

   %part 1
   tIg=Ig;
   tIl=Il;
   tUc=Uc;

   k1Ig=(hh/Lo)*(tUc-(Ro*tIg)-tUs);
   k1Uc=-hh*tIg/Co;
   k1Il=(hh/Ll)*(tUs-(Rl*tIl));

   %part 2
   tIg=Ig+(k1Ig/4);
   tIl=Il+(k1Il/4);
   tUc=Uc+(k1Uc/4);

   k2Ig=(hh/Lo)*(tUc-(Ro*tIg)-tUs);
   k2Uc=-hh*tIg/Co;
   k2Il=(hh/Ll)*(tUs-(Rl*tIl));
```

```
   %part 3
   tIg=Ig+(3*k1Ig/32)+(9*k2Ig/32);
   tIl=Il+(3*k1Il/32)+(9*k2Il/32);
   tUc=Uc+(3*k1Uc/32)+(9*k2Uc/32);

   k3Ig=(hh/Lo)*(tUc-(Ro*tIg)-tUs);
   k3Uc=-hh*tIg/Co;
   k3Il=(hh/Ll)*(tUs-(Rl*tIl));

   %part 4
   tIg=Ig+(1932*k1Ig/2197)-(7200*k2Ig/2197)+(7296*k3Ig/2197);
   tIl=Il+(1932*k1Il/2197)-(7200*k2Il/2197)+(7296*k3Il/2197);
   tUc=Uc+(1932*k1Uc/2197)-(7200*k2Uc/2197)+(7296*k3Uc/2197);

   k4Ig=(hh/Lo)*(tUc-(Ro*tIg)-tUs);
   k4Uc=-hh*tIg/Co;
   k4Il=(hh/Ll)*(tUs-(Rl*tIl));

   %part 5
   tIg=Ig+(439*k1Ig/216)-(8*k2Ig)+(3680*k3Ig/513)-(845*k4Ig/4104);
   tIl=Il+(439*k1Il/216)-(8*k2Il)+(3680*k3Il/513)-(845*k4Il/4104);
   tUc=Uc+(439*k1Uc/216)-(8*k2Uc)+(3680*k3Uc/513)-(845*k4Uc/4104);

   k5Ig=(hh/Lo)*(tUc-(Ro*tIg)-tUs);
   k5Uc=-hh*tIg/Co;
   k5Il=(hh/Ll)*(tUs-(Rl*tIl));

   %part 6
   tIg=Ig-(8*k1Ig/27)+(2*k2Ig)-(3544*k3Ig/2565)+(1859*k4Ig/4104)-
(11*k5Ig/40);
   tIl=Il-(8*k1Il/27)+(2*k2Il)-(3544*k3Il/2565)+(1859*k4Il/4104)-
(11*k5Il/40);
   tUc=Uc-(8*k1Uc/27)+(2*k2Uc)-(3544*k3Uc/2565)+(1859*k4Uc/4104)-
(11*k5Uc/40);

   k6Ig=(hh/Lo)*(tUc-(Ro*tIg)-tUs);
   k6Uc=-hh*tIg/Co;
   k6Il=(hh/Ll)*(tUs-(Rl*tIl));

   %Yn+1
   Ig_old=Ig;
   Il_old=Il;
   Uc_old=Uc;

   Ig=Ig+(16*k1Ig/135)+(6656*k3Ig/12825)+(28561*k4Ig/56430)-
(9*k5Ig/50)+(2*k6Ig/55);
   Il=Il+(16*k1Il/135)+(6656*k3Il/12825)+(28561*k4Il/56430)-
(9*k5Il/50)+(2*k6Il/55);
   Uc=Uc+(16*k1Uc/135)+(6656*k3Uc/12825)+(28561*k4Uc/56430)-
(9*k5Uc/50)+(2*k6Uc/55);

   Ping1=(k1Ig/360)-(128*k3Ig/4275)-
(2197*k4Ig/75240)+(k5Ig/50)+(2*k6Ig/55);
   Ping2=(k1Uc/360)-(128*k3Uc/4275)-
(2197*k4Uc/75240)+(k5Uc/50)+(2*k6Uc/55);
   Ping3=(k1Il/360)-(128*k3Il/4275)-
(2197*k4Il/75240)+(k5Il/50)+(2*k6Il/55);

   if abs(Ping1)/abs(Ig)>error_ping;
      tock=1;
   end

   if abs(Ping2)/abs(Uc)>error_ping;
      tock=1;
```

```
    end

    if abs(Ping3)/abs(Il)>error_ping;
       tock=1;
    end

    if tock==1;
       Ig=Ig_old;
       Uc=Uc_old;
       Il=Il_old;
       hh=hh/1.02;
       nn
    end

    if tock==0;
       hh=hh*1.02;

       CurG(nn)=Ig;
       VolC(nn)=Uc;
       CurL(nn)=Il;

       POS_macro;
       VolS(nn)=tUs;
       Us=tUs;

       ttime(nn)=tt;
       tt=tt+hh;
       nn=nn+1;
    end


end
nn

plot(ttime,CurG,ttime,CurL,ttime,CurG-CurL)

%plot(ttime,CurL)
%plot(ttime,VolS)
%plot(ttime,VolC);

grid on
box on

xlabel('time')
ylabel('Y')

%axis ([0 lc rc rc+D]);
```

```
%----------POS_Macro--------------------------------------%

%---------------------------------------------------------%
%-- Model to determine sheath potential as a function --%
%-- of the sheath current and cathode magnetic field  --%
%---------------------------------------------------------%

flip=0;

tIe=tIg-tIl;
del=tIe/(2*pi*epl*lc);
kap=(tIe/(2*pi*ni*vd*Z*qe))*sqrt(me*Z/mi);
rs=kap/lc;

if rs<=rc;
   flip=1;
   tUs=0;
end

n=1;
t=0;
time(n)=t;

h=1e-12;
error_margin=1e-4;

Py=rc;
Pz=0;
Vy=1;
Vz=1;
Ey=1;

while flip==0;
   tick=0;

   %part 1
   tVy=Vy;
   tVz=Vz;
   tPy=Py;
   tPz=Pz;
   tEy=Ey;

   tR4=sqrt(((tPy)^2)+((lc-tPz)^2));
   tR1=sqrt(((tPy)^2)+(tPz^2));
   tB1=(mu/(4*pi))*((Ig+Il)/(tPy));
   tB2=(mu/(4*pi))*((Ig-Il)/(tPy))*((lc-tPz)/tR4);
   tB3=(mu/(4*pi))*((Ig-Il)/(lc))*(((tPy)/tR4)-((tPy)/tR1));
   tBx=tB1+tB2+tB3;

   bet=((C^2)-(tVy^2)-(tVz^2));
   tm=me*C/sqrt(bet);
   gam=tm/bet;

   k1Vy=h*(qe/gam)*((((tEy-(tVz*tBx))/(tVy*tVz))-
((tVy*tBx)/(((tVz^2))+bet)))/(((((tVy^2))+bet)/(tVy*tVz))-
((tVy*tVz)/(((tVz^2))+bet))));
   k1Vz=h*(qe/gam)*((((tVy*tBx)/(tVy*tVz))-((tEy-
(tVz*tBx))/(((tVy^2))+bet)))/(((((tVz^2))+bet)/(tVy*tVz))-
((tVy*tVz)/(((tVy^2))+bet))));
   k1Py=h*tVy;
   k1Pz=h*tVz;
   k1Ey=(h/tPy)*(del-(tVy*tEy));

   %part 2
```

```
    tVy=Vy+(k1Vy/4);
    tVz=Vz+(k1Vz/4);
    tPy=Py+(k1Py/4);
    tPz=Pz+(k1Pz/4);
    tEy=Ey+(k1Ey/4);

    tR4=sqrt(((tPy)^2)+((lc-tPz)^2));
    tR1=sqrt(((tPy)^2)+(tPz^2));
    tB1=(mu/(4*pi))*((Ig+Il)/(tPy));
    tB2=(mu/(4*pi))*((Ig-Il)/(tPy))*((lc-tPz)/tR4);
    tB3=(mu/(4*pi))*((Ig-Il)/(lc))*(((tPy)/tR4)-((tPy)/tR1));
    tBx=tB1+tB2+tB3;

    bet=((C^2)-(tVy^2)-(tVz^2));
    tm=me*C/sqrt(bet);
    gam=tm/bet;

    k2Vy=h*(qe/gam)*((((tEy-(tVz*tBx))/(tVy*tVz))-
((tVy*tBx)/(((tVz^2))+bet)))/(((((tVy^2))+bet)/(tVy*tVz))-
((tVy*tVz)/(((tVz^2))+bet))));
    k2Vz=h*(qe/gam)*((((tVy*tBx)/(tVy*tVz))-((tEy-
(tVz*tBx))/(((tVy^2))+bet)))/(((((tVz^2))+bet)/(tVy*tVz))-
((tVy*tVz)/(((tVy^2))+bet))));
    k2Py=h*tVy;
    k2Pz=h*tVz;
    k2Ey=(h/tPy)*(del-(tVy*tEy));

    %part 3
    tVy=Vy+(3*k1Vy/32)+(9*k2Vy/32);
    tVz=Vz+(3*k1Vz/32)+(9*k2Vz/32);
    tPy=Py+(3*k1Py/32)+(9*k2Py/32);
    tPz=Pz+(3*k1Pz/32)+(9*k2Pz/32);
    tEy=Ey+(3*k1Ey/32)+(9*k2Ey/32);

    tR4=sqrt(((tPy)^2)+((lc-tPz)^2));
    tR1=sqrt(((tPy)^2)+(tPz^2));
    tB1=(mu/(4*pi))*((Ig+Il)/(tPy));
    tB2=(mu/(4*pi))*((Ig-Il)/(tPy))*((lc-tPz)/tR4);
    tB3=(mu/(4*pi))*((Ig-Il)/(lc))*(((tPy)/tR4)-((tPy)/tR1));
    tBx=tB1+tB2+tB3;

    bet=((C^2)-(tVy^2)-(tVz^2));
    tm=me*C/sqrt(bet);
    gam=tm/bet;

    k3Vy=h*(qe/gam)*((((tEy-(tVz*tBx))/(tVy*tVz))-
((tVy*tBx)/(((tVz^2))+bet)))/(((((tVy^2))+bet)/(tVy*tVz))-
((tVy*tVz)/(((tVz^2))+bet))));
    k3Vz=h*(qe/gam)*((((tVy*tBx)/(tVy*tVz))-((tEy-
(tVz*tBx))/(((tVy^2))+bet)))/(((((tVz^2))+bet)/(tVy*tVz))-
((tVy*tVz)/(((tVy^2))+bet))));
    k3Py=h*tVy;
    k3Pz=h*tVz;
    k3Ey=(h/tPy)*(del-(tVy*tEy));

    %part 4
    tVy=Vy+(1932*k1Vy/2197)-(7200*k2Vy/2197)+(7296*k3Vy/2197);
    tVz=Vz+(1932*k1Vz/2197)-(7200*k2Vz/2197)+(7296*k3Vz/2197);
    tPy=Py+(1932*k1Py/2197)-(7200*k2Py/2197)+(7296*k3Py/2197);
    tPz=Pz+(1932*k1Pz/2197)-(7200*k2Pz/2197)+(7296*k3Pz/2197);
    tEy=Ey+(1932*k1Ey/2197)-(7200*k2Ey/2197)+(7296*k3Ey/2197);

    tR4=sqrt(((tPy)^2)+((lc-tPz)^2));
    tR1=sqrt(((tPy)^2)+(tPz^2));
```

```
   tB1=(mu/(4*pi))*((Ig+Il)/(tPy));
   tB2=(mu/(4*pi))*((Ig-Il)/(tPy))*((lc-tPz)/tR4);
   tB3=(mu/(4*pi))*((Ig-Il)/(lc))*(((tPy)/tR4)-((tPy)/tR1));
   tBx=tB1+tB2+tB3;

   bet=((C^2)-(tVy^2)-(tVz^2));
   tm=me*C/sqrt(bet);
   gam=tm/bet;

   k4Vy=h*(qe/gam)*((((tEy-(tVz*tBx))/(tVy*tVz))-
((tVy*tBx)/(((tVz^2))+bet)))/(((((tVy^2))+bet)/(tVy*tVz))-
((tVy*tVz)/(((tVz^2))+bet))));
   k4Vz=h*(qe/gam)*((((tVy*tBx)/(tVy*tVz))-((tEy-
(tVz*tBx))/(((tVy^2))+bet)))/(((((tVz^2))+bet)/(tVy*tVz))-
((tVy*tVz)/(((tVy^2))+bet))));
   k4Py=h*tVy;
   k4Pz=h*tVz;
   k4Ey=(h/tPy)*(del-(tVy*tEy));

   %part 5
   tVy=Vy+(439*k1Vy/216)-(8*k2Vy)+(3680*k3Vy/513)-(845*k4Vy/4104);
   tVz=Vz+(439*k1Vz/216)-(8*k2Vz)+(3680*k3Vz/513)-(845*k4Vz/4104);
   tPy=Py+(439*k1Py/216)-(8*k2Py)+(3680*k3Py/513)-(845*k4Py/4104);
   tPz=Pz+(439*k1Pz/216)-(8*k2Pz)+(3680*k3Pz/513)-(845*k4Pz/4104);
   tEy=Ey+(439*k1Ey/216)-(8*k2Ey)+(3680*k3Ey/513)-(845*k4Ey/4104);

   tR4=sqrt(((tPy)^2)+((lc-tPz)^2));
   tR1=sqrt(((tPy)^2)+(tPz^2));
   tB1=(mu/(4*pi))*((Ig+Il)/(tPy));
   tB2=(mu/(4*pi))*((Ig-Il)/(tPy))*((lc-tPz)/tR4);
   tB3=(mu/(4*pi))*((Ig-Il)/(lc))*(((tPy)/tR4)-((tPy)/tR1));
   tBx=tB1+tB2+tB3;

   bet=((C^2)-(tVy^2)-(tVz^2));
   tm=me*C/sqrt(bet);
   gam=tm/bet;

   k5Vy=h*(qe/gam)*((((tEy-(tVz*tBx))/(tVy*tVz))-
((tVy*tBx)/(((tVz^2))+bet)))/(((((tVy^2))+bet)/(tVy*tVz))-
((tVy*tVz)/(((tVz^2))+bet))));
   k5Vz=h*(qe/gam)*((((tVy*tBx)/(tVy*tVz))-((tEy-
(tVz*tBx))/(((tVy^2))+bet)))/(((((tVz^2))+bet)/(tVy*tVz))-
((tVy*tVz)/(((tVy^2))+bet))));
   k5Py=h*tVy;
   k5Pz=h*tVz;
   k5Ey=(h/tPy)*(del-(tVy*tEy));

   %part 6
   tVy=Vy-(8*k1Vy/27)+(2*k2Vy)-(3544*k3Vy/2565)+(1859*k4Vy/4104)-
(11*k5Vy/40);
   tVz=Vz-(8*k1Vz/27)+(2*k2Vz)-(3544*k3Vz/2565)+(1859*k4Vz/4104)-
(11*k5Vz/40);
   tPy=Py-(8*k1Py/27)+(2*k2Py)-(3544*k3Py/2565)+(1859*k4Py/4104)-
(11*k5Py/40);
   tPz=Pz-(8*k1Pz/27)+(2*k2Pz)-(3544*k3Pz/2565)+(1859*k4Pz/4104)-
(11*k5Pz/40);
   tEy=Ey-(8*k1Ey/27)+(2*k2Ey)-(3544*k3Ey/2565)+(1859*k4Ey/4104)-
(11*k5Ey/40);

   tR4=sqrt(((tPy)^2)+((lc-tPz)^2));
   tR1=sqrt(((tPy)^2)+(tPz^2));
   tB1=(mu/(4*pi))*((Ig+Il)/(tPy));
   tB2=(mu/(4*pi))*((Ig-Il)/(tPy))*((lc-tPz)/tR4);
   tB3=(mu/(4*pi))*((Ig-Il)/(lc))*(((tPy)/tR4)-((tPy)/tR1));
```

```
   tBx=tB1+tB2+tB3;

   bet=((C^2)-(tVy^2)-(tVz^2));
   tm=me*C/sqrt(bet);
   gam=tm/bet;

   k6Vy=h*(qe/gam)*((((tEy-(tVz*tBx))/(tVy*tVz))-
((tVy*tBx)/(((tVz^2))+bet)))/(((((tVy^2))+bet)/(tVy*tVz))-
((tVy*tVz)/(((tVz^2))+bet))));
   k6Vz=h*(qe/gam)*((((tVy*tBx)/(tVy*tVz))-((tEy-
(tVz*tBx))/(((tVy^2))+bet)))/(((((tVz^2))+bet)/(tVy*tVz))-
((tVy*tVz)/(((tVy^2))+bet))));
   k6Py=h*tVy;
   k6Pz=h*tVz;
   k6Ey=(h/tPy)*(del-(tVy*tEy));

   %Yn+1
   Vy_old=Vy;
   Vz_old=Vz;
   Py_old=Py;
   Pz_old=Pz;
   Ey_old=Ey;

   Vy=Vy+(16*k1Vy/135)+(6656*k3Vy/12825)+(28561*k4Vy/56430)-
(9*k5Vy/50)+(2*k6Vy/55);
   Vz=Vz+(16*k1Vz/135)+(6656*k3Vz/12825)+(28561*k4Vz/56430)-
(9*k5Vz/50)+(2*k6Vz/55);
   Py=Py+(16*k1Py/135)+(6656*k3Py/12825)+(28561*k4Py/56430)-
(9*k5Py/50)+(2*k6Py/55);
   Pz=Pz+(16*k1Pz/135)+(6656*k3Pz/12825)+(28561*k4Pz/56430)-
(9*k5Pz/50)+(2*k6Pz/55);
   Ey=Ey+(16*k1Ey/135)+(6656*k3Ey/12825)+(28561*k4Ey/56430)-
(9*k5Ey/50)+(2*k6Ey/55);

   Error1=(k1Py/360)-(128*k3Py/4275)-
(2197*k4Py/75240)+(k5Py/50)+(2*k6Py/55);
   Error2=(k1Pz/360)-(128*k3Pz/4275)-
(2197*k4Pz/75240)+(k5Pz/50)+(2*k6Pz/55);
   Error3=(k1Vy/360)-(128*k3Vy/4275)-
(2197*k4Vy/75240)+(k5Vy/50)+(2*k6Vy/55);
   Error4=(k1Vz/360)-(128*k3Vz/4275)-
(2197*k4Vz/75240)+(k5Vz/50)+(2*k6Vz/55);
   Error5=(k1Ey/360)-(128*k3Ey/4275)-
(2197*k4Ey/75240)+(k5Ey/50)+(2*k6Ey/55);

   if abs(Error1)/abs(Py)>error_margin;
      tick=1;
   end

   if abs(Error2)/abs(Pz)>error_margin;
      tick=1;
   end

   if abs(Error3)/abs(Vy)>error_margin;
      tick=1;
   end

   if abs(Error4)/abs(Vz)>error_margin;
      tick=1;
   end

   if abs(Error5)/abs(Ey)>error_margin;
      tick=1;
   end
```

```
   if tick==1;
      Vy=Vy_old;
      Vz=Vz_old;
      Py=Py_old;
      Pz=Pz_old;
      Ey=Ey_old;

      h=h/1.02;
   end

   if tick==0;
      h=h*1.02;

      tUs=me*(C^2)*((1/(sqrt(1-(((Vy^2)+(Vz^2))/C^2))))-1)/qe;

      if %Py>rs;
      if Py>(kap/(lc-Pz));
         flip=1;
      end

      if Py<=0;
         flip=1;
      end

      time(n)=t;
      t=t+h;
      n=n+1;
   end


end
```

Appendix F:

```
%---------------------------%
%--- ROGOWSKI COIL MODEL ---%
%---------------------------%

%NOTE: By changing the parameters of the RLC circuit the duration
%of the current pulse (to be measured by the Rogowski coil) may be
%manipulated. Hence the effect on the coil may be observed. This
%model may be used to design a coil for measurement of a current
%pulse as defined by the RLC values as specified by the user. The
%coil may be manipulated by changing the physical dimensions of the
%coil, as well as the wire diameter, number of turns, terminating
%resistor etc.

echo off;
clear all;

%RLC CIRCUIT PARAMETERS:
V=4e4;                  %Voltage to which capacitor Cp is charged
Rp=0.5;                 %Resistance of RLC circuit
Lp=1e-6;                %Inductance of RLC circuit
Cp=5e-6;                %Capacitance of RLC circuit

aa=-Rp/(2*Lp);
bb=sqrt(((Rp/(2*Lp))^2)-(1/(Lp*Cp)));
%aa and bb are properties of the algebraic solution to
%the damped RLC circuit.

%ROGOWSKI COIL PARAMETERS
N=620;                  %number of turns on coil
a=7.5e-3;
b=7.5e-3;               %former dimensions: width=2*a, height=2*b
r=45e-3;                %former major radius
rr=2*sqrt(a*b/pi);      %equivilant former radius were it round and
                        %not square.
Rt=.1;                  %Terminating resistor
RHO=.175;               %Wire resistance per unit length
length=N*(sqrt(((2*pi*r/N)^2)+((4*(a+b))^2)));
                        %wire length
Rwire=length*RHO;       %Wire resistance.
Rs=Rt+Rwire             %Total secondary (Rogowski) resistance.
wd=.4e-3;               %Wire diameter

mu=4*pi*1e-7;           %Magnetic permitivity of free space
G=((-5/4)+log(4*pi*r/(wd*N)));
                        %Inductance parameters
H=(7e-4)+(0.1773*log(N))-(3.22e-2*((log(N))^2))+(1.97e-
3*((log(N))^3));
M=N*(mu*b/pi)*log((r+a)/(r-a))
                        %Mutual inductance of Rogowski coil
Ls=mu*rr*N*((N*rr/(2*r))+G-H)
                        %Self inductance of Rogowski coil
TORR=Ls/Rs              %Coil time constant

n=2;                    %nth iteration
t=0;
time(n)=t;
h=1e-15;                %initial step size, is made larger or smaller
                        %according to error term.
```

```
Ip=0;                       %initial primary current
dIp=(V/(bb*Lp))*exp(aa*t)*((aa*sinh(bb*t))+(bb*cosh(bb*t)));
                            %Initial rate of change of primary current.
Is=0;                       %Initial secondary current

CurP(1)=0;
CurS(1)=0;
tick=0;

while t<2e-5   %duration over which calculation is performed
   %part 1
   tIs=Is;
   k1Is=(h/Ls)*(-(M*dIp)+(Rs*tIs));

   %part 2
   tIs=Is+(k1Is/4);
   k2Is=(h/Ls)*(-(M*dIp)+(Rs*tIs));

   %part 3
   tIs=Is+(3*k1Is/32)+(9*k2Is/32);
   k3Is=(h/Ls)*(-(M*dIp)+(Rs*tIs));

   %part 4
   tIs=Is+(1932*k1Is/2197)-(7200*k2Is/2197)+(7296*k3Is/2197);
   k4Is=(h/Ls)*(-(M*dIp)+(Rs*tIs));

   %part 5
   tIs=Is+(439*k1Is/216)-(8*k2Is)+(3680*k3Is/513)-(845*k4Is/4104);
   k5Is=(h/Ls)*(-(M*dIp)+(Rs*tIs));

   %part 6
   tIs=Is-(8*k1Is/27)+(2*k2Is)-(3544*k3Is/2565)+(1859*k4Is/4104)-
(11*k5Is/40);
   k6Is=(h/Ls)*(-(M*dIp)+(Rs*tIs));

   %Yn+1
   Is=Is+(16*k1Is/135)+(6656*k3Is/12825)+(28561*k4Is/56430)-
(9*k5Is/50)+(2*k6Is/55);

   Error=real((k1Is/360)-(128*k3Is/4275)-
(2197*k4Is/75240)+(k5Is/50)+(2*k6Is/55));

   if abs(Error)/abs(Is)>1e-17;
      h=h/1.2;
      else h=h*1.2;
      end

   CurS(n)=Is;
   %CurS is the secondary (Rogowski coil) current
   CurP(n)=(V/(bb*Lp))*exp(aa*t)*sinh(bb*t);
   %CurP is the primary (measured) current

   if CurP(n)*CurP(n-1)<0
      tick=tick+1
   end
   time(n)=t;
   t=t+h;
   n=n+1;
   dIp=(V/(bb*Lp))*exp(aa*t)*((aa*sinh(bb*t))+(bb*cosh(bb*t)));

end
n
```

```
VRp=Rp*CurP;

Vout=-Rt*CurS;
%Vout is the voltage output measured at the
%terminals of the Rogowski coil across the terminating resistor Rt

Vint=(Rt*M/Ls)*CurP;
%Vint is the fictitious voltage that would be measured were the
rogowski
%coil output a linear function of the measured current.

plot(time,CurP);
%plot(time,CurS);
%plot(time,Vout);
%plot(time,VRp);
%plot(time,PowerP);

%plot(time,Vout,time,Vint);
%Examination of this graph reveals the subtle differences between the
%Ideal integrating Rogowski coil and a REAL Rogowski coil.

grid on
box on

xlabel('time (Seconds)')
%ylabel('Rogowski Output (Volts)')
ylabel('Known Driving Current (Amperes)')
```

References

[1] W. Sarjeant and R. Dollinger, *High-Power electronics*, Tab Books, pp 171, 1989

[2] E. E. Kunhardt, *Basic theory of gas breakdown* in *A critical analysis and assessment of high power switches*, Naval Surface Weapons Centre, pp 399, 1978

[3] K.R. Spangenberg, *Vacuum Tubes*, Mcgraw & Hill, pp 23, 1948,

[4] F. Llewellyn-Jones, *Ionisation Avalanches and Breakdown*, Methuen & Co., pp 50, 1967

[5] A.L. Ward, J. Appl. Phys., vol. **33**, pp 2789, 1964

[6] J.H. Ingold, *Glow Discharges at DC and Low Frequencies*, Academic Press, pp 19, 1978

[7] J. I. Levatter and Shao-Chi Lin, *Necessary conditions for the homogenous formation of pulsed avalanche discharges at high gas pressures*, J. Appl. Phys., vol. **51**(1), pp 213, 1980

[8] H. Seguin and J. Tulip, *Photo-initiated and photo-sustained laser*, Appl. Phys. Lett., vol. **21**(9), pp 414, 1972

[9] P. W. Pace and M. Lacombe, *A sealed high repetition rate TEA CO_2 laser*, IEEE Journal of Quantum electronics, vol. **QE-14** (4), pp 263, 1978.

[10] L. Denes and J. Lowke, *V-I characteristics of pulsed CO_2 laser discharges*, Appl. Phys. Letters, vol. **23**(3), pp 130-132, 1973.

[11] R.H. Dishington, W.R. Hook and R.P. Hilberg, *Flash-lamp discharge and laser efficiency*, Applied Optics, vol. **13**(10), pp 2300, 1974.

[12] Frank B. Frugel, *High Speed Pulse Technology*, Volume IV, Academic Press Inc., pp 146, 1980.

[13] J.H. Goncz, J. Appl. Phys., vol. **36**, pp 742, 1965.

[14] C. F. Gerald, P. O. Wheatley, *Applied Numerical Analysis*, Addison-Wesley, pp 356, 1970

[15] M.A. Plonus, *Applied Electromagnetics*, McGraw & Hill, pp 87, 1978

[16] A. Larrson, *Numerical modelling of inhibited electrical discharges in air*, J. Phys. D: Appl. Phys. vol. **31**, pp 1831, 1998

[17] R. Feng, *Automated System for the Power Measurement in the Silent Discharge*, IEEE Trans. On Industry Apps., vol. **34**(3), 1998

[18] G.C. Chryssis, *High Frequency Switching Power Supplies*, 2nd edition., McGraw & Hill, pp 53, 1984

[19] G.A. Mesyats, D.I. Proskurovsky, *Pulsed Electrical Discharge in Vacuum*, Springer-Verlag, pp 5-32, 1989

[20] M. Kristiansen and M.O. Hagler, *Spark Gaps* in *A critical analysis and assessment of high power switches*, Naval Surface Weapons Centre, pp 266-277, 1978

[21] C.W. Mendel, D.M. Zagar, G.S. Mills, S Humphries, and SA Goldstein, *Carbon plasma gun*, Rev. Sci. Instrum., vol. **51**(12), pp 1641, 1980

[22] T.J. Renk, *Flashboards as a plasma source for plasma opening switch applications*, J. Appl. Phys., vol. **65**(7), pp 2652, 1989

[23] P.F. Ottinger, S.A. Goldstein, and R.A. Meger, *Theoretical modelling of the plasma erosion opening switch for inductive storage applications*, J. Appl. Phys., vol. **56**(3), pp 776, 1984

[24] R.J. Commisso, G. Cooperstein, R.A, Meger, J.M. Neri, and P.F. Ottinger, *The Plasma Erosion Opening Switch*, from *Opening Switches*, Plenum Press, pp 149, 1987

[25] D.D. Hinshelwood, J.R. Boller, R.J. Commisso, G. Cooperstein, R.A. Meger, J.M. Neri, P.F. Ottinger, and B.V. Weber, *Plasma Erosion Opening switch operation at long conduction times*, IEEE transactions on Plasma Science, vol. **PS-15**(5), pp 564, 1987

[26] R.W. Shumacher and R.J. Harvey, *Low Pressure Plasma Opening Switches,* from *Opening Switches*, Plenum Press, pp 93, 1987

[27] K.R. Spangenberg, *Vacuum Tubes*, Mcgraw & Hill, pp 175, 1948

[28] Ron Arad, http://plasma-gate.weizmann.ac.il/

[29] W. Rogowski, W. Steinhaus, *Die Messung der magnetischen spanning*, Archiv. Electrotegnik, vol. **1**(4), pp 141-150, 1912

[30] H. Krompholz, J. Doggett, K. Schoenbach, J. gahl, C. Harjes, G. Schaefer and M. Kristiansen, *Nanosecond current probe for high voltage experiments*, Rev. Sci. Instruments, vol **55**(1), pp 127-128, 1984

[31] K. Nalty, R. Zowarka, L. Holland, *Instrumentation for EM launcher systems*, IEEE transactions on Magnetics, vol. **Mag-20**(2), pp 328-331, 1984

[32] W. Stygar, G. Gerdin, "High Frequency Rogowski Coil Response Characteristics", IEEE Transactions on Plasma Science, vol. **PS-10**(1), pp 40-44, 1982

[33] M. A. Plonus, *Applied Electromagnetics*, McGraw & Hill, pp 203-208, 1978

[34] J. E. Parton, S. J. T. Owen and M. S. raven, *Applied Electromagnetics*, MacMillan, 1975.

[35] F. W. Grover, *Inductance Calculations*, Dover Press, 1962

[36] D. Pellinen, M. Di Capua, S. Sampayan, H. Gerbracht, M. Wang, *Rogowski Coil For Measuring Fast, High-level Pulsed Currents*, Rev. Sci. Instruments, vol **51**(11), pp 1535-1540, 1980